FOR FURTHER TRAN

AFML-TR-77-11

STUDIES OF HYDRODYNAMIC RAM INDUCED BY HIGH VELOCITY SPHERICAL FRAGMENT SIMULATORS

UNIVERSITY OF DAYTON RESEARCH INSTITUTE
300 COLLEGE PARK AVENUE
DAYTON, OHIO 45469

JUNE 1977

TECHNICAL REPORT AFML-TR-77-11
FINAL REPORT FOR PERIOD AUGUST 1975 - NOVEMBER 1976

Approved for public release; distribution unlimited.

AIR FORCE MATERIALS LABORATORY
AIR FORCE WRIGHT AERONAUTICAL LABORATORIES
AIR FORCE SYSTEMS COMMAND
WRIGHT-PATTERSON AIR FORCE BASE, OHIO 45433

NOTICE

When Government drawings, specifications, or other data are used for any purpose other than in connection with a definitely related Government procurement operation, the United States Government thereby incurs no responsibility nor any obligation whatsoever; and the fact that the Government may have formulated, furnished, or in any way supplied the said drawings, specifications, or other data, is not to be regarded by implication or otherwise as in any manner licensing the holder or any other person or coroporation, or conveying any rights or permission to manufacture, use, or sell any patented invention that may be related in any way thereto.

This report has been reviewed by the Information Office (OI) and is releasable to the National Technical Information Service (NTIS). At NTIS, it will be available to the general public, including foreign nations.

This technical report has been reviewed and is approved for publication.

James S. Wilbeck

James S. Wilbeck, Capt. USAF
Project Monitor

FOR THE COMMANDER

G. E. Eichelman

G. E. Eichelman, Chief
Metals Behavior Branch
Metals and Ceramics Division
Air Force Materials Laboratory

Copies of this report should not be returned unless return is required by security considerations, contractual obligations, or notice on a specific document.

UNCLASSIFIED

SECURITY CLASSIFICATION OF THIS PAGE (When Data Entered)

18 19 REPORT DOCUMENTATION PAGE

READ INSTRUCTIONS BEFORE COMPLETING FORM

1. REPORT NUMBER: AFML-TR-77-11

2. GOVT ACCESSION NO.

3. RECIPIENT'S CATALOG NUMBER: 9

4. TITLE (and Subtitle): 6 STUDIES OF HYDRODYNAMIC RAM INDUCED BY HIGH VELOCITY SPHERICAL FRAGMENT SIMULATORS.

5. TYPE OF REPORT & PERIOD COVERED: Final Report, August 1975-November 1976,

6. PERFORMING ORG. REPORT NUMBER: 14 UDRI-TR-77-09

7. AUTHOR(s): 10 S. J./Bless, J. P./Barber, P. F./Fry, R. K./Newman

8. CONTRACT OR GRANT NUMBER(s): 15 F33615-75-C-5156

9. PERFORMING ORGANIZATION NAME AND ADDRESS:
University of Dayton Research Institute
300 College Park Avenue
Dayton, Ohio 45469

10. PROGRAM ELEMENT, PROJECT, TASK AREA & WORK UNIT NUMBERS: 16 7351, 735106, 735106A7 17 06

11. CONTROLLING OFFICE NAME AND ADDRESS: 12 193p.

12. REPORT DATE: 11 June 1977

13. NUMBER OF PAGES: 161

14. MONITORING AGENCY NAME & ADDRESS (if different from Controlling Office):
Air Force Materials Laboratory
Air Force Wright Aeronautical Laboratories
Air Force Systems Command
Wright-Patterson Air Force Base, Ohio

15. SECURITY CLASS. (of this report): UNCLASSIFIED

15a. DECLASSIFICATION DOWNGRADING SCHEDULE

16. DISTRIBUTION STATEMENT (of this Report)

Approved for public release; distribution unlimited.

17. DISTRIBUTION STATEMENT (of the abstract entered in Block 20, if different from Report)

18. SUPPLEMENTARY NOTES

19. KEY WORDS (Continue on reverse side if necessary and identify by block number)

20. ABSTRACT (Continue on reverse side if necessary and identify by block number)

Hydrodynamic ram events in simulated fuel cells have been studied both experimentally and theoretically. A moiré fringe technique was developed for dynamic measurement of out-of-plane displacement. Spherical projectiles 11.1 and 14.3 mm diameter were used in the velocity range 1.5 to 2.4 km/s. Data for entrance and side panel displacement, projectile trajectory, cavity growth, shock propagation, and fluid pressure were obtained for many impact configurations. A fluid drag code, a fluid shock code, the BR-1A (HR) code, over

DD FORM 1 JAN 73 1473 EDITION OF 1 NOV 65 IS OBSOLETE

UNCLASSIFIED

SECURITY CLASSIFICATION OF THIS PAGE (When Data Entered)

105 400

LB

20. ABSTRACT (Cont'd)

the AFTON finite difference code, and the NONSAP finite element code were exercised and the results compared with experimental data.

It was found that the failure mode of entrance panels was propagation of cracks caused by hoop stresses induced at very early times around the entrance site. Entrance panel damage was reduced by use of ductile alloys and eliminated by ballistic foam of thickness equal to the projectile diameter.

The fluid drag code provided an adequate description of fluid loading. However, the panel displacements predicted by the BR-1A (HR) code were unacceptably low. The principal reasons for this were inadequacies in the piston theory embodied in the code. AFTON-BR-1A calculations provided a marked improvement.

The AFTON-NONSAP calculations of entrance panel displacement were felt to be acceptable. This approach appears to be the nearest to providing a reliable method of predicting hydrodynamic ram-induced structural failure.

PREFACE

The program described in this report was carried out by the University of Dayton Research Institute under contract to the Air Force Materials Laboratory, Contract F33615-75-C-5156. The numerical studies were conducted under subcontract by California Research and Technology, Inc.

The work was conducted in support of Project 7351, "Metallic Materials," and Task 735106, "Behavior of Metals Used in Flight Vehicle and Engine Structural Applications," for the Metals Behavior Branch of the Metals and Ceramics Division during the period February 1975 to January 1977. The contract monitor was Capt. James S. Wilbeck of the Materials Laboratory. The project engineer was Mr. W.E. Hackenberger of the Air Force Flight Dynamics Laboratory. The work was funded by the Joint Technical Coordinating Group through the cooperation of Mr. A.J. Holten of the Flight Dynamics Laboratory.

This report was submitted by the authors in June 1977 for publication as a Materials Laboratory Technical Report.

TABLE OF CONTENTS

SECTION		PAGE
I	INTRODUCTION AND SUMMARY	1
	1.1 Background	1
	1.2 Objectives	4
	1.3 Approach of Program	4
	1.4 Summary of Results	6
II	EXPERIMENTAL FACILITY	8
	2.1 Main Experimental Facility	8
III	ANALYSIS OF MOIRE FRINGE DATA	14
	3.1 Description of Moire Optical Apparatus	14
	3.2 Theoretical Analysis of Moire Fringes	18
	3.3 Empirical Methods of Moire Fringe Data Reduction	30
IV	EXPERIMENTS AND RESULTS	35
	4.1 Introduction	35
	4.2 Description of Panel Damage	37
	4.3 Measurement of Wall Displacement	47
	4.4 Projectile Drag Determination	56
	4.5 Shock Velocity Measurements	62
	4.6 Pressure Measurements	66
V	CALCULATIONS	69
	5.1 The Fluid Drag Code (FDC)	69
	5.2 The Fluid Shock Code	79
	5.3 BR-1A (HR) Structural Response Code	85
	5.4 Finite Difference Calculations	97
VI	SUMMARY AND CONCLUSIONS	105
	APPENDIX A: FINITE ELEMENT/FINITE DIFFERENCE ANALYSIS OF FUEL TANK PENETRATION BY STEEL FRAGMENTS	107
	APPENDIX B: LISTING OF COMPUTER PROGRAMS	147
	REFERENCES	159

PRECEDING PAGE BLANK

LIST OF ILLUSTRATIONS

FIGURE		PAGE
1.	Peak shock pressure in tanks penetrated by blunt steel projectiles.	3
2.	Diagram of range hardware and instrumentation for main experimental facility.	8
3.	Drawing of 760ℓ target tank.	10
4.	Photograph of 760ℓ target tank, with entrance and side panels removed.	11
5.	Instrumentation for shock tank range.	13
6.	Moiré optical apparatus.	15
7.	Intensity vs. time for flash light source.	16
8.	Optical diagram of moiré apparatus.	17
9.	Target grid.	17
10.	Moiré triangle.	19
11.	Moiré geometric interference diagram.	20
12.	Moiré analytical diagram.	22
13.	Moiré ellipses.	26
14.	Panel shapes calculated for Shot FT5B at various times after impact.	27
15.	Cross section of fiducial step structure.	28
16.	Fringes produced on fiducial step structure for Shots FT5B and FT26A.	31
17.	Fringe map prepared from data of Figure 16.	32
18.	Panel shapes derived for fringe data from Shot FT5B and fringe map of Figure 17.	33
19.	Flash x-radiograph of 11.1 mm diameter projectile as it contacts the second mylar foil switch in Shot FT26A.	38
20.	Panel from Shot FT2 after impact.	38
21.	Panel from Shot FT3 after impact.	39
22.	Panel from Shot FT4 after impact.	39
23.	Panel from Shot FT5 after impact.	40
24.	Panel from Shot FT6 after impact.	41
25.	Panel from Shot FTA3, 1.6 mm thick 2024-T3 aluminum.	41

LIST OF ILLUSTRATIONS (CONT'D)

FIGURE		PAGE
26.	Panel from Shot FTA4, 1.6 mm thick 2024-T3 aluminum.	42
27.	Panel from Shot FTA5, 1.6 mm thick 2024-T3 aluminum.	42
28.	Panel from Shot FTA6, 1.6 mm thick 2024-T3 aluminum.	43
29.	Panel from Shot FTA10, 1.6 mm thick 2024-T3 aluminum.	43
30.	Panel from Shot FTA12, 1.6 mm thick 2024-T3 aluminum.	44
31.	Profiles through impact hole of selected 2024-T3 alloy entrance panels.	45
32.	Framing camera pictures of moiré fringes from shot FT5B.	49
33.	Out-of-plane displacement (measured from pre-impact surface).	50
34.	Same as Figure 33 except for vertical line through impact point.	50
35.	Same as Figure 33, but for Shot FT26A, an 11.1 mm diameter sphere striking a 2024-T3 panel backed by 38 mm of ballistic foam at 1.52 km/s.	52
36.	Same as Figure 35, but for vertical line through impact site.	52
37.	Same as Figure 33, except for Shot FT8, a 14.3 mm diameter sphere striking a 2024-T3 panel backed by 38 mm of ballistic foam at 1.59 km/s.	53
38.	Same as Figure 33, except for Shot FT6, a 14.3 mm diameter sphere striking a 2024-T3 panel at 1.52 km/s.	53
39.	Same as Figure 33, except for Shot FT2, an 11.1 mm diameter sphere striking a 7075-T6 panel at 1.73 km/s.	54
40.	Same as Figure 33, but for side panel of Shot FT33, a 14.3 mm diameter sphere striking at 1.83 km/s.	55
41.	Same as Figure 40, except for a line 150 mm below trajectory.	56
42.	Projectile entering tank in Shot FT4.	57
43.	Successive framing camera photographs of projectile penetrating fluid in Shot FTA9.	58

LIST OF ILLUSTRATIONS (CONT'D)

FIGURE		PAGE
44.	Drag coefficient vs. Reynolds number for spheres, (taken from Prandtl[23]).	59
45.	Drag coefficient vs. mach number for spheres (taken from Shapiro[24]).	59
46.	Reynolds number vs. velocity for spheres.	60
47.	Initial velocity vs. impact velocity for spherical projectiles.	63
48.	Comparison of measured projectile trajectory and trajectory calculated from best fit drag coefficient for Shot FT5.	63
49.	Peak shock pressure calculated from shock velocity data from Shot FTA9.	64
50.	Shock position vs. time for Shot FT9.	65
51.	Shot FT31, transducer T3 (431 mm from entrance panel, 100 mm above trajectory).	67
52.	Shot FT34 Upper beam: Transducer T4 (737 mm from entrance panel, 180 mm from trajectory) 1.35 MN/m^2/div. Lower beam: Transducer T5 (983 mm from entrance panel, 180 mm from trajectory), 1.6 MN/m^2/div., 1.5 ms delayed sweep.	67
53.	Comparison of pressure computed by FDC and pressure measured by a transducer in Shot 33 at a point located at 100 mm above trajectory 0.74 m from the entrance panel.	73
54.	Same as Figure 53, except for a point 0.43 m behind the entrance panel.	74
55.	Same as Figure 52, but for a point 220 mm above trajectory and 133 mm behind entrance panel.	75
56.	Comparison of pressure profiles predicted by FDC and AFTON for a point 100 mm behind the entrance panel and 100 mm off trajectory.	76
57.	Same as Figure 56, but for a point 50 mm behind entrance panel.	76
58.	Comparison of experimental and predicted cavitation at z = 133 mm for Shot FT5.	77
59.	Pressure-time history predicted at selected points on trajectory for impact conditions of Shot FT5.	78
60.	Pressure-time history for selected points above and below trajectory for impact conditions of Shot FT5.	79

LIST OF ILLUSTRATIONS (CONT'D)

FIGURE		PAGE
61.	Typical pressure profile calculated by three methods.	83
62.	Scheme used in calculating the impulse delivered by the shock pressures to the entrance panel.	84
63.	Plot of force vs. time for pressure calculated at entrance panel for Shot FT5B.	85
64.	Finite element model of left side of a fuel tank entrance panel.	87
65.	Comparison of panel profiles predicted by BR-1A (HR) code and measured during Shot FT5B.	89
66.	Out-of-plane displacement at nodes of calculation shown in Figure 63, at 0.89 ms after impact.	89
67.	Panel velocity at node 16 (see Figure 62) for calculation shown in Figure 63.	91
68.	Piston theory pressure at node 16 for the calculation shown in Figure 63.	91
69.	Comparison of BR-1A calculation with experimental data for case of 11.1 mm diameter sphere striking 1.5 mm thick 2024-T3 panel at 1.5 km/s.	92
70.	Displacement profile predicted for case of 11.1 mm diameter sphere striking 1.5 mm thick 7075-T6 panel at 1.73 km/s.	94
71.	Element used in BR-1A calculation of side panel displacement.	96
72.	Comparison of side panel profile computed by BR-1A (HR) calculation and profile measured in experiment FT33.	96
73.	Panel velocity at node 27 (see Figure 69) of calculation shown in Figure 72.	98
74.	Finite element model of .50 caliber projectile perforating the entrance wall of a fuel tank.	99
75.	Drag parameter vs. projectile displacement for smoothly tumbling and rapidly tumbling projectiles and for an 11.1 mm diameter steel fragment simulator.	99
76.	Comparison of AFTON-NONSAP calculation with experimental data for case of 11.1 mm diameter sphere striking 1.5 mm thick 2024-T3 panel at 1.5 km/s.	101

LIST OF SYMBOLS

a	•projectile cross-sectional area
A	•arbitrary ray in moiré model •area of annulus on entrance panel
b	•parameter used in moiré wedge solution
B	•arbitrary ray in moiré model
c	•sound velocity
C_D	•drag coefficient
d	•distance along equivalent grid from ray A to ray B
D	•sphere diameter
E	•projectile kinetic energy
f	•distance along optical axis from base vertex to equivalent grid
F	•force
g	•distance along equivalent grid from projection axis to ray A
h	•height of fringe
H	•parameter used in fluid shock code
i	•arbitrary integer in moiré solution
k	•parameter used in moiré wedge solution •parameter used in shock position equation
L	•one-half length of moiré baseline
m	•projectile mass
M	•mach number
n	•parameter used in shock position equation
N	•fringe number
p	•pitch of equivalent grid (Ronchi ruling)
P	•pressure
q	•parameter used in moiré wedge solution

$\bar{r}$	•shock front position
R	•projectile radius •radius of annulus on entrance panel
Re	•Reynolds number
t	•time
u	•particle velocity
u_o	•projectile impact velocity
u_i	•projectile initial velocity in fluid
u_f	•fluid velocity normal to wall
U	•shock propagation velocity
w	•wall velocity
x	•moiré model: distance parallel to baseline •moiré displacement solution: distance across entrance panel •shock position data: horizontal distance into tank from entrance panel •fluid drag code: horizontal distance across entrance panel
x'	•horizontal distance across entrance panel in moiré photographs
X	•arbitrary point on equivalent grid
y	•moiré model: distance perpendicular to baseline •fluid drag code: vertical distance across entrance panel •displacement of tank wall
Y	•arbitrary point on equivalent grid
z	•horizontal distance into tank from entrance panel

LIST OF SYMBOLS (cont'd)

α	•angle between baseline and optical axis
β	•angle between baseline and ray A •parameter used in fluid shock code
γ	•angle between baseline and ray B
ζ	•slope of fringe with respect to vertical
Θ	•angle between optical axis and ray B
μ	•viscosity
ρ	•density
ρ_f	•fluid density
ρ_o	•density of unshocked material
ρ_p	•projectile density
ρ_1	•density of shocked material
ϕ	•angle between fiducial plane and undeformed target
ψ	•parameter used in shock position equation

LIST OF UNITS

MASS	g (gram)	= 0.0022046 lb_m (pounds-mass)
	kg (kilogram)	= 10^3 g
LENGTH	m (meter)	= 3.2808 ft (feet)
		= 39.37 in (inches)
	cm (centimeter)	= 0.01 m
		= 2.54 in
TIME	s (second)	
FORCE	N (Newton)	= 0.2248 lb_f (pounds-force)
	MN (Meganewton)	= 10^6 N
DENSITY	kg/m^3	= 0.0624 lb_m/ft^3
		= 3.613×10^{-5} lb_m/in^3
PRESSURE	MN/m^2	= 10 Bars
		= 145.04 lb_f/in^2

SECTION I
INTRODUCTION AND SUMMARY

1.1 BACKGROUND

The process by which projectiles penetrating fuel cells transfer kinetic and chemical (explosive) energy to the fuel cell structure is termed hydrodynamic ram. Hydrodynamic ram has proven to be a major combat-related threat to modern aircraft. The development of design principles for fuel cells less vulnerable to ram damage is a priority task. Hence, a number of research programs have been conducted to investigate the coupling of projectile energy, energy to penetrated fluids[1-6], the coupling of fluid momentum to containing structures[1,5,7], and the response of fuel cell structures to fluid loading[1-3, 7-9].

The present program is addressed to hydrodynamic ram induced by high-velocity fragment simulators. When such a projectile/fragment penetrates a filled fuel cell structure, energy is transferred to the structure through pressure in the fluid. The pressure in the fluid is generated by two different mechanisms, the impact induced shock waves, and the subsonic flow around the penetrating projectile. Each mechanism will be reviewed in detail.

1.1.1 Shock Induced Pressure

The portion of the projectile trajectory during which shock waves are generated is sometimes referred to as the shock or entrance phase of hydrodynamic ram. When the projectile strikes the entrance panel, a shock wave is driven into the panel material. At the panel/fluid boundary, this shock is transmitted into the fluid. If the projectile is supersonic in the fluid after panel perforation, shock waves may continue to propagate away from the projectile. The pressure propagates

into the fluid as an expanding quasihemispherical shock wave. The amplitude of the wave decays rapidly due to geometric spreading and the generation of release waves at the entrance site. As the shock wave propagates along the entrance panel, the panel is exposed to extremely high pressures for a short time. The resulting panel motion can produce localized stress states near the entrance hole which are sufficient to initiate tensile cracks and gross tearing of the entrance panel.

The maximum possible amplitude of the impact induced shock in the fluid is that which would result from a one dimensional impact. The magnitude of the one dimensional pressure can be calculated from the Hugoniot relationship[10]

$$P = \rho_o u U^{*} \tag{1}$$

and

$$\rho_o U = \rho_1 (U-u) \tag{2}$$

together with the measured P-u Hugoniots for the fluid (water)[12], projectile[11], and cell wall[12], and the traditional assumptions that pressure and particle velocity are continuous across interfaces[10]. The magnitude of the impact pressure computed from (1) and (2) is very high, as illustrated in Figure 1. For comparison, the tensile strength of aluminum is only about 500 MN/m^2. The peak shock pressure in the fluid will be less than the value shown in Figure 1 for relatively pointed projectiles (e.g., of impact radius less than the wall thickness). Due to geometric speeding, the peak pressure in the fluid will decay inversely with radial distance (as 1/r). In addition, release waves generated at the boundaries of the impact region (entrance panel) overtake the shock front and further reduce its intensity.

---

*P, ρ_o, ρ_1, u, and U denote, respectively, the pressure across the shock front, the density of unshocked material, the density of shocked material, the particle velocity change across the shock, and the propagation velocity of the shock with respect to the undisturbed material.

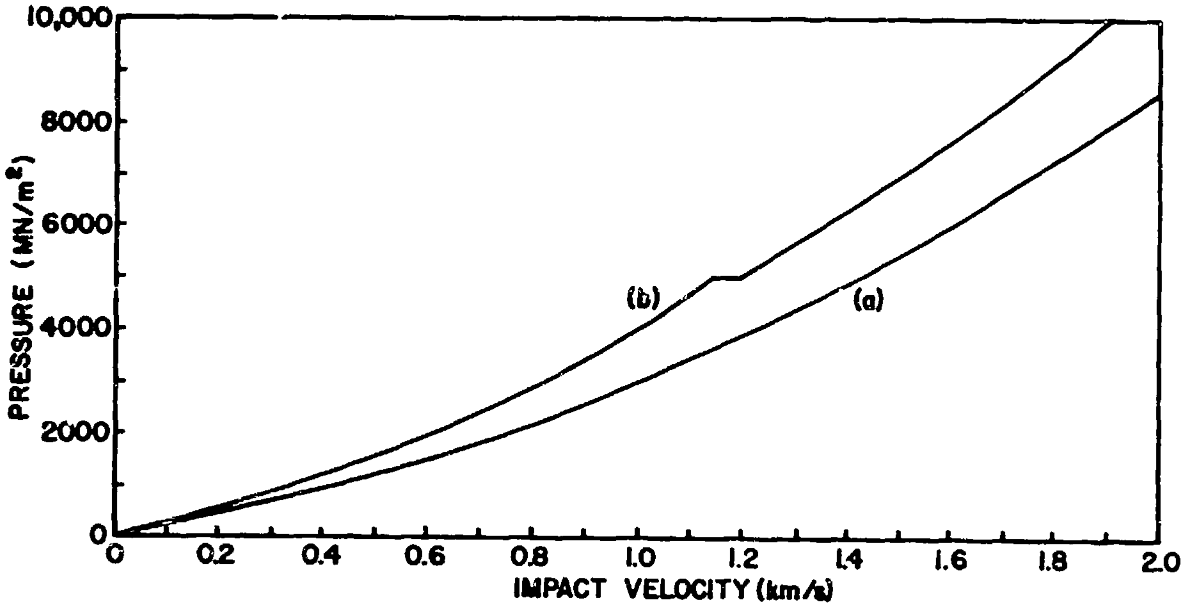

Figure 1. Peak Shock Pressure in Tanks Prenetrated by Blunt Steel Projectiles. (a) Walls of Negligible Thickness. (b) Thick Aluminum Walls.

1.1.2 Drag Related Pressure

In the drag or cavity phase of a hydrodynamic ram event, the projectile is slowed by drag forces as it passes through the fluid. The momentum imparted to the fluid by the projectile produces a cavity behind the projectile and a pressure pulse throughout the fluid which loads the cell panels over a large area. If the projectile is tumbling or breaks up, significant fluctuations in pressure can result. Fluid motion and pressure usually persist even after the projectile has come to rest or exited the tank. Occasionally, local failure in side panels result from the drag phase loading. More frequently, failure occurs at the fasteners which are unable to resist the net force on the panel.

A number of analytical treatments of this phase of hydrodynamic ram have been developed[7,9]. The starting point for such analyses is the energy loss rate of the projectile

given by

$$\frac{\delta E}{\delta x} = \frac{\rho_o C_D \, a \, u^2}{2} \qquad (3)$$

where E is the kinetic energy of the projectile, x is the distance along trajectory, C_D is the drag coefficient, a is the projectile cross sectional area and u is the projectile velocity. The energy loss rate is assumed to be due to the work which the drag phase pressure does on the penetrating projectile.

1.1.3 Exit Phase

The exit phase occurs when the projectile perforates a panel and leaves the cell. In the exit phase, the exit panel is first stressed by fluid which is accelerated and compressed ahead of the projectile and then struck by the projectile itself. The coupling of hydrodynamic ram with ballistic loading can result in extensive radial cracking of the exit panel in the impact region(3). When such an exit panel failure occurs, it is generally attributed to a steep increase in fluid pressure as the projectile approaches the wall, followed immediately by projectile impact. In some cases the high pressure preceding the projectile is sufficient to initiate radial cracking before perforation occurs.

1.2 OBJECTIVES

The research program described in this report had two principal objectives. The first was to evaluate two available analytic codes for prediction of hydrodynamic ram effects. A second objective was to obtain an understanding of ram phenomenology for high velocity spherical fragments.

1.3 APPROACH OF PROGRAM

The hydrodynamic ram prediction codes which appeared to be most promising were the BR-1A(HR) finite element code and the AFTON finite difference code. (These codes are described in detail in Section V of this report). The experiments were designed to provide the input data which the codes require and

to provide data with which the output of the codes could be compared.

The principal target employed was a replica of an A-10 fuselage tank with a capacity of 760ℓ (200 gal). For convenience and safety, the tank was filled with water. The panel material was 1.6 mm thick aluminum. Two alloys were selected, 7075-T6 and 2024 T-3. They find widespread use in aircraft and have well known material properties. Some panels were backed with AVCO Thermarest® ballistic foam; this material was selected because previous work has suggested its effectiveness in reducing ram damage[8], and because its "crush-up" properties have been well determined.

Early in the program it was found that important entrance phase phenomena occur at very early times and are highly localized. To aid the study of these effects, a series of experiments was conducted in a small shock tank of 28ℓ volume.

It was felt that the complications caused by asymmetrical entrance holes and tumbling projectiles would defeat an attempt to assess the basic validity of the computer treatments. Therefore, spherical projectiles were used throughout this program. The velocities employed spanned the range expected for high velocity fragments in combat, 1.5 to 2.4 km/s. The trajectory was at 90° to the entrance panel.

The data required to exercise the hydrodynamic ram codes are the projectile position as a function of time in the fluid, and the velocity of the shock front in the fluid. In addition, pressure measurements within the fluid were obtained. The codes were verified by comparisons between calculated and measured panel displacements.

Measurement of panel out-of-plane displacement was carried out using a moiré fringe technique. This technique has a temporal resolution of 80 μs and a displacement resolution of 0.3 mm. Measurements of projectile trajectory was determined from a 7000 f/s framing camera record of the progress of the projectile through the fluid. Shock velocity measurement was made with a 10^6 f/s framing camera. A number of piezoelectric

pressure transducers were placed in the tank to obtain pressure data.

1.4 SUMMARY OF RESULTS

Twenty-nine shots were completed for which data was obtained for out-of-plane entrance or side panel displacement, projectile drag coefficient, cavity expansion rate, shock velocity, and pressure. The NWC fluid drag code[14] and a fluid shock code were applied to the experimental configurations and pressure input was generated for the structure code. The BR-1A(HR) code was adapted for the fluid loads on the structure. The boundary conditions corresponding to the laboratory target tank were set up. The California Research and Technology (CRT) AFTON code was also applied to the experimental configurations. The AFTON/NONSAP calculation showed good qualitative and quantitative agreement with the experimental results. The BR-1A(HR) results showed poor agreement with experimental measurements. The difficulty was traced to the fluid pressure/wall motion coupling scheme.

The experimental data support the following statements:

1. High velocity fragments caused severe damage to entrance panels.

2. In these experiments foam of thickness equal to the projectile diameter effectively eliminated entrance panel damage.

3. Aluminum alloy 2024-T3 was superior to 7075-T6 for defeating hydrodynamic ram.

4. For the configuration and threat used in these tests, side panel failures were not initiated.

5. The moiré fringe technique provided an excellent way to analyze panel motion; distance-time resolutions of 0.3 mm and 80 μs were readily achievable.

6. The NWC pressure code is a valuable technique for quantitative calculation of early-time behavior and qualitative calculation of late-time events when reflections dominate the pressure.

7. Peak entrance out-of-plane displacements of the order of 30 mm were observed for the threats tested.

SECTION II
EXPERIMENTAL FACILITY

Two ballistic ranges at the University of Dayton Research Institute were instrumented for study of hydrodynamic ram effects in fuel cells. One of these ranges was dedicated to the main series of experiments which consisted of measurements of ram induced fuel cell panel motion, fluid pressure, and projectile trajectories. The second range was devoted to study of early time shock effects in fuel cells.

2.1 MAIN EXPERIMENTAL FACILITY

The hardware and instrumentation for the principal range used in this program is shown in Figure 2.

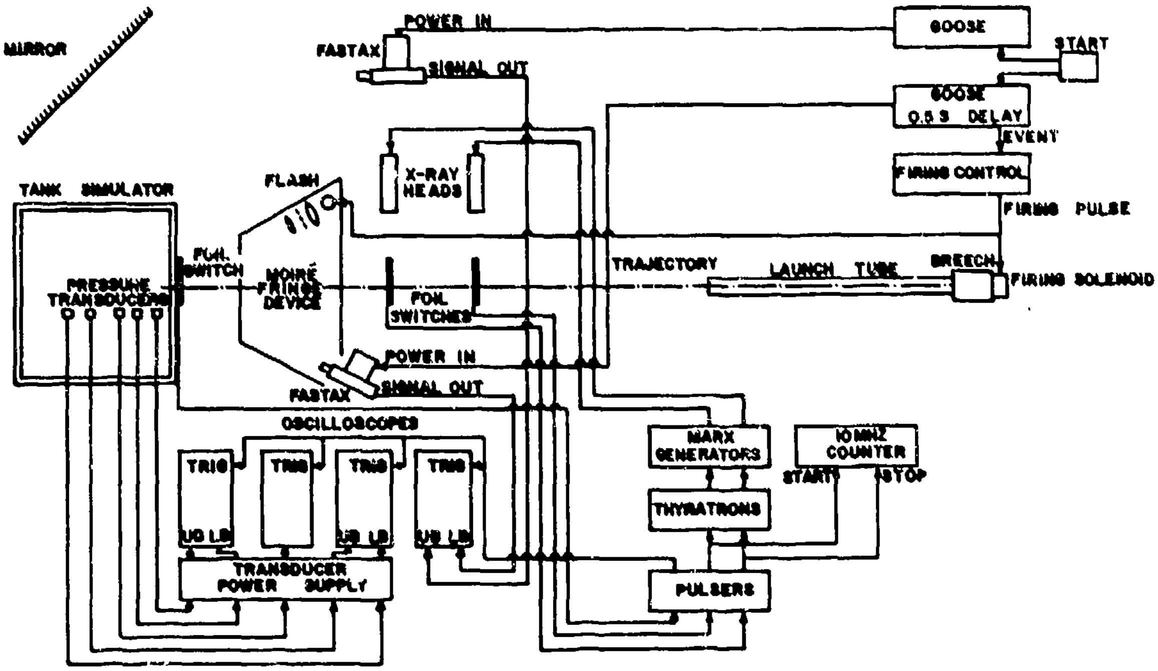

Figure 2. Diagram of Range Hardware and Instrumentation for Main Experimental Facility.

It consisted of a projectile launcher, velocity measurement stations, moiré fringe displacement-measuring equipment, and an instrumented replica A-10 fuselage section.

2.1.1 Projectiles

The projectiles used in this program were spherical fragment simulators made from annealed ball bearings (52100 chrome manganese steel). The two sizes used were 5.5 and 11 g, with diameters of 11.1 and 14.3 mm. The microhardness of the projectiles was 280 Hv (Vickers hardness scale, 10^ g load).

The spheres were launched in serrated polycarbonate sabots which were stripped by aerodynamic forces and stopped by metal baffles within the blast tank. Launch velocities were varied from 1.4 to 2.3 km/s.

2.1.2 Launch Apparatus

The projectile launch apparatus consisted of a breech, barrel, and blast tank. The specially-designed breech had a chamber capacity up to 110 g. The barrel had a bore diameter of 20 mm and a length of 2.3 m; the muzzle end was inserted into the blast tank. The blast tank was evacuated to a pressure of about 10 kN/m^2 (0.1 Atm). Baffle plates within the blast tank served to contain the sabot as well as to reduce the air blast within the range.

The velocity measurement section of the range consisted of aluminum foil-mylar switches and two flash x-rays. The switches were constructed of two sheets of aluminum foil separated by a thin sheet of mylar. The first switch was placed 29 cm downrange of the blast tank and the second switch was placed 55 cm downrange of the first. In addition, for most shots, a third switch was mounted on the target tank front wall 1.8 m beyond the first switch. The radiographs were used to determine projectile position and integrity at the switches. The first two switches, as shown in Figure 2, were connected to passive pulsers which triggered both the flash x-rays and a 10 MHz counter-timer. On several shots, a 1 MHz counter-timer was connected between the second and third switches.

To compute projectile velocities, times were taken from the counter readings and distances were computed in two steps. First, the distance traversed by the projectile was determined approximately using the distance between the foil switches. Secondly, the distance was determined more accurately from readings of the projectile position in the radiographs. Projectile velocity could be determined to be within ± 0.5% using the radiographs and to within ± 1.0% using only the distances between the foil switches.

2.1.3 Target Tank

The target tank consisted of two sections of a replica A-10 fuselage. The sections were permanently bolted together and the center ports removed. The overall dimensions of the tank are indicated in Figure 3. A photograph of this tank is shown in Figure 4.

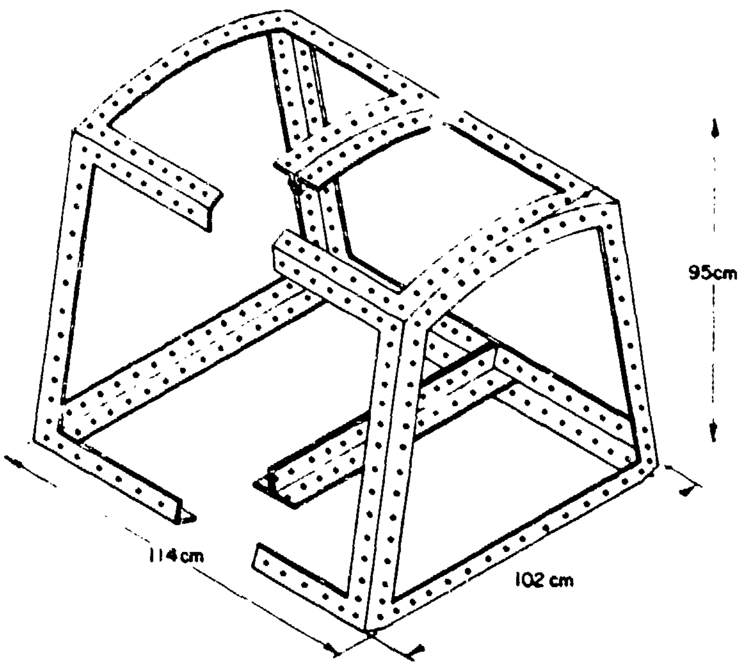

Figure 3. Drawing of 760ℓ Target Tank.

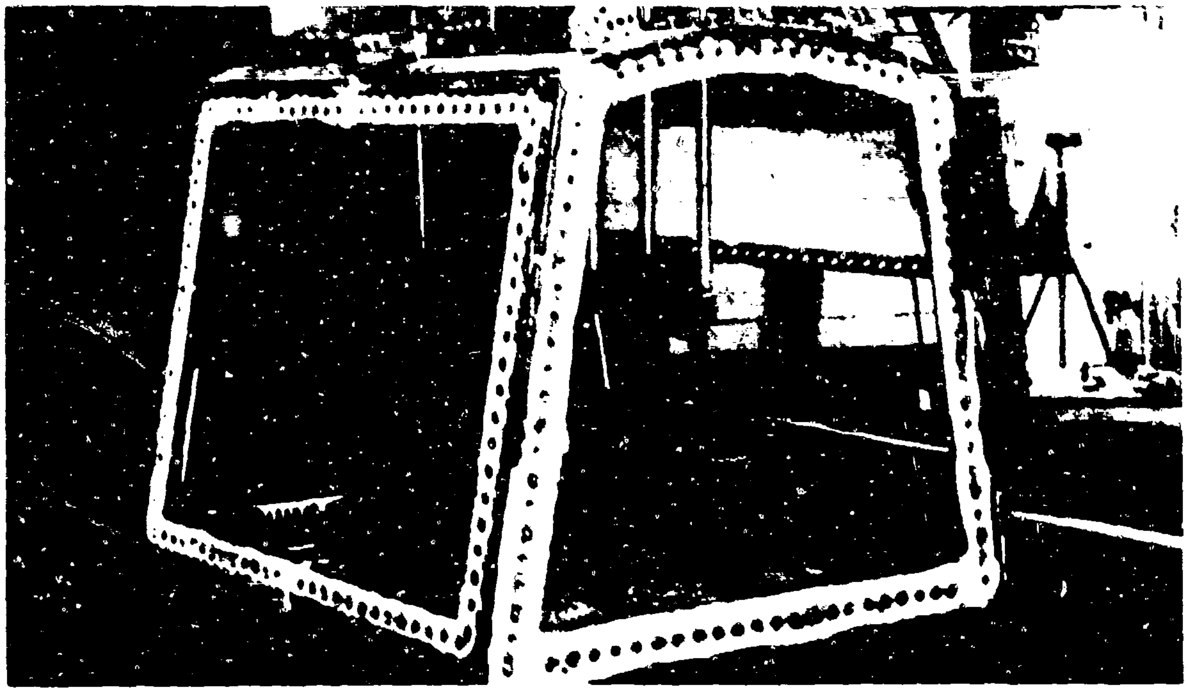

Figure 4. Photograph of 760ℓ Target Tank, with Entrance and Side Panels Removed. Supports for holding five pressure transducers are mounted independent of tank.

The tank was filled with approximately 760ℓ of tap water. The two bulkhead panels and one side panel were used as test panels. The test panels were made of 1 [illegible] mm thick aluminum alloy and were fastened with 9.5 mm (3/8 in) bolts at 38 mm intervals. A layer of rubber between the panels and the frame prevented leakage. The other side panel was constructed of 19 mm thick aluminum with a 0.3 m by 1.0 m viewing port. The viewing port was covered with a 12 mm thick polycarbonate window. The bottom of the tank was made of 1.6 mm thick 7075-T6 aluminum backed with 10 mm of plywood. The frame was 9.5 mm thick stainless steel. The top of the tank was open. The tank was orientated so that the bulkhead panels were the entrance and exit panels for the projectiles.

2.1.4 <u>Target Tank Instrumentation</u>

2.1.4.1 Moiré fringe apparatus

A moiré fringe optical system was mounted on a

movable, adjustable tripod, and was directed at either the entrance or the side test panel. This system is described in detail in Section III.

The moiré fringe data was recorded with a high-speed framing camera (Fastax). The speed of the camera was determined either by monitoring the drive sprocket rotation with a reluctance loop and oscilloscope, or by using a built-in timing light source. Two speeds were used, 6000 and 12,000 f/s. Illumination was accomplished with "Press 50" flash lamps. The film employed was Eastman Double X developed in Acufine developer for 10 min.

2.1.4.2 Projectile drag measurements

The progress of the projectile through the tank, and the development of the cavity, were recorded with a high-speed framing camera. This camera photographed the interior of the tank through the polycarbonate side window. Its speed was monitored with an oscilloscope, and was either 6000 or 12,000 f/s. Illumination for this camera consisted of six reflector photoflood lamps.

2.1.4.3 Pressure measurements

Five (occasionally four) piezoelectric pressure transducers were placed in the tank. They were mounted in aluminum caps threaded onto 20 mm diameter galvanized steel water pipe and inserted into the tank from the top. The tip of the transducer protruded slightly from the cap to eliminate the possibility of an air bubble forming.

Most of the transducers were PCB 102A04. This transducer is calibrated to 70 MN/m^2 and has a rise time of 1 μs. For measurements near the entrance point, a Kistler Model 207C3 transducer was sometimes employed. It has a peak pressure rating of 700 MN/m^2. The transducer outputs were recorded on cathode ray oscilloscopes. The oscilloscope trigger signal was generated from the third foil switch located at the entrance panel.

2.2 SHOCK TANK RANGE

The shock tank range was assembled to obtain data for shock wave propagation in the immediate vicinity of the entrance hole of a penetrated fuel cell. A diagram of this range is presented in Figure 5. The projectiles, the launch apparatus, and the foil switches were essentially identical to those used on the principal range. The target tank was a cube of 28ℓ capacity. The sides were 6.3 mm thick plexiglass and the entrance panel was 1.6 mm thick aluminum.

Instrumentation consisted of a Beckman and Whitley Model 300 framing camera and spark light source. The camera exposed 48 frames at speeds up to 4.5×10^6 f/s. The camera runs continually during the experiment and data is obtained by timing the discharge of the spark light source. The spark was triggered from the third foil switch mounted near the entrance panel, as shown in Figure 5. The camera framing rate was generally 6×10^5 f/s.

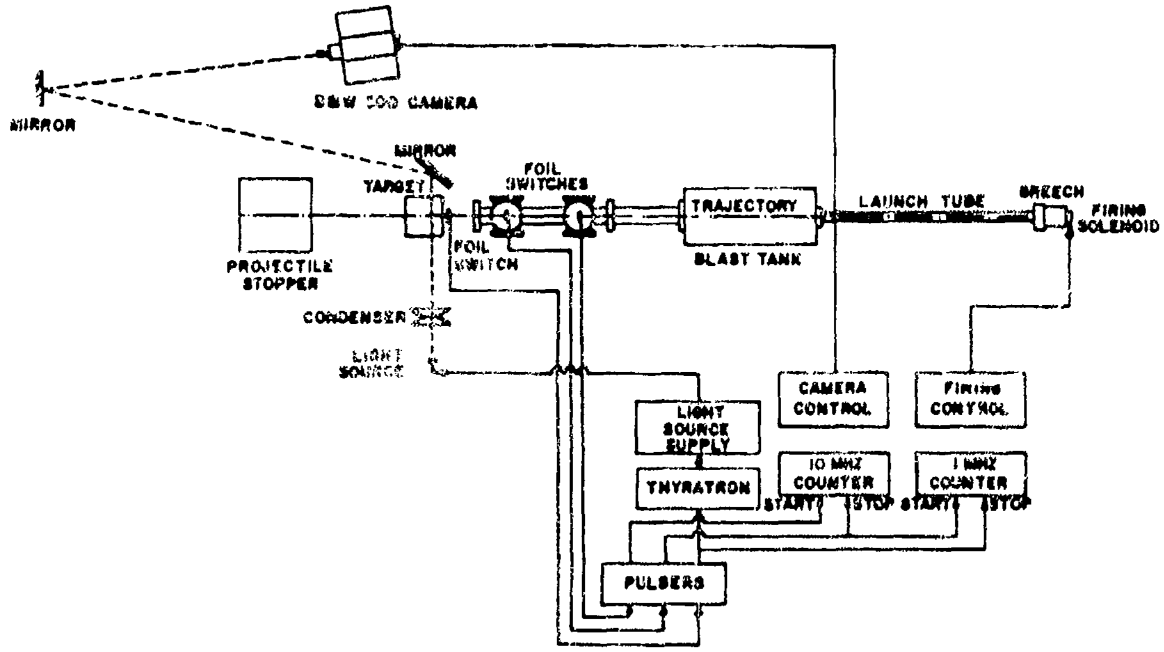

Figure 5. Instrumentation for Shock Tank Range.

SECTION III
ANALYSIS OF MOIRÉ FRINGE DATA

The reduction of moiré fringe data to yield information on out-of-plane displacement constituted a major effort of this program. Two approaches were developed: empirical and theoretical. In the empirical approach, the locations of fringes in space were determined by means of suitable fiducial data. The position of each fringe on the target panel was then used to obtain the out-of-plane displacement of the panel at that point. In the theoretical approach, the form of the fringe pattern was derived from the geometry and dimensions of the optical system. The theoretical approach is more powerful and can be automated with computer programs. A computer program based on the theoretical treatment was developed and debugged with the aid of the empirical solutions.

The combination f theoretical and empirical data reduction techniques provided a deep understanding of moiré fringes and the properties of the fringe patterns used in these experiments. In the following sections the moiré apparatus is described in detail, the theoretical model of fringe production is explained, and the empirical data reduction technique is described.

3.1 DESCRIPTION OF MOIRÉ OPTICAL APPARATUS

The moiré optical apparatus consisted primarily of two Ronchi rulings, commercially available lenses, a high intensity light source, and a high speed framing camera. The apparatus is shown schematically in Figure 6. The optical elements were mounted onto one-meter long optical benches which were bolted to a 1.2 m square, 19 mm thick aluminum table. The table could be both elevated and tilted.

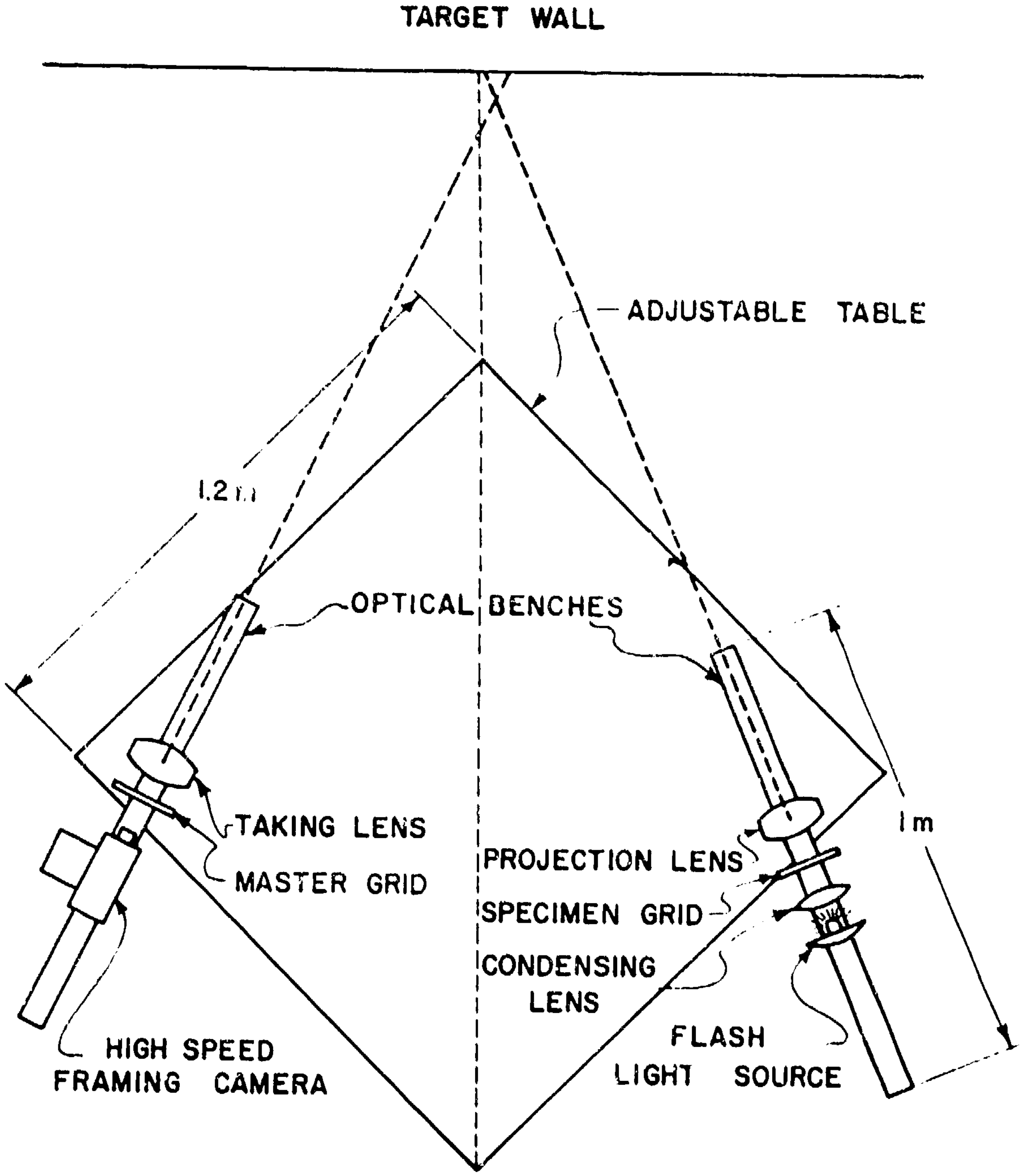

Figure 6. Moiré Optical Apparatus.

The light source chosen was a "Press 50" flash lamp with an intensity of more than 0.8 Mlm for at least 30 ms, as shown in Figure 7. This was sufficient light for recording approximately 180 frames of information at a framing rate of 6,000 f/s. The Ronchi rulings were glass slides with evenly-spaced, finely-ruled lines, separated by a distance equal to the line width. The rulings had 78.7 lines per centimeter (200 lines per inch). A Fastax high-speed framing camera was used to record the moiré fringes.

An optical block diagram of the moiré fringe apparatus is shown in Figure 8. Light from the flash lamp was collected by the condensing lens and focused to a point inside the projection lens. The projectile lens, a 80 mm-f/2.8 lens, was used to project an image of the specimen grid (a Ronchi ruling) onto the target wall. The image of the specimen grid on the tank wall was called the target grid. Due to the angle of projection, the pitch spacing between grid lines of the target was not constant as illustrated in Figure 9.

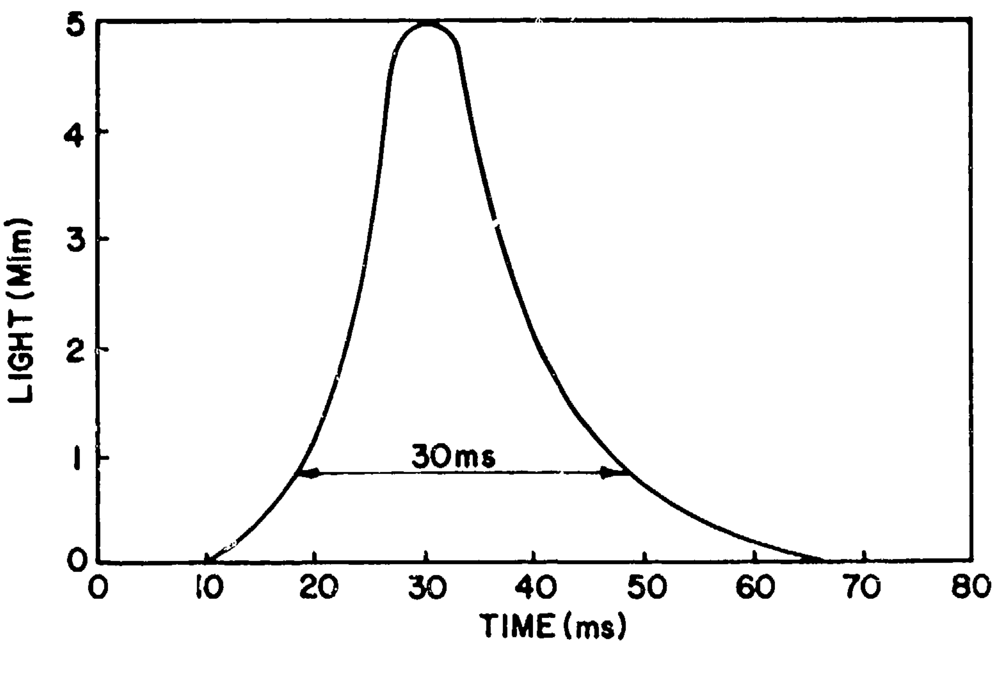

Figure 7. Intensity vs. Time for Flash Light Source.

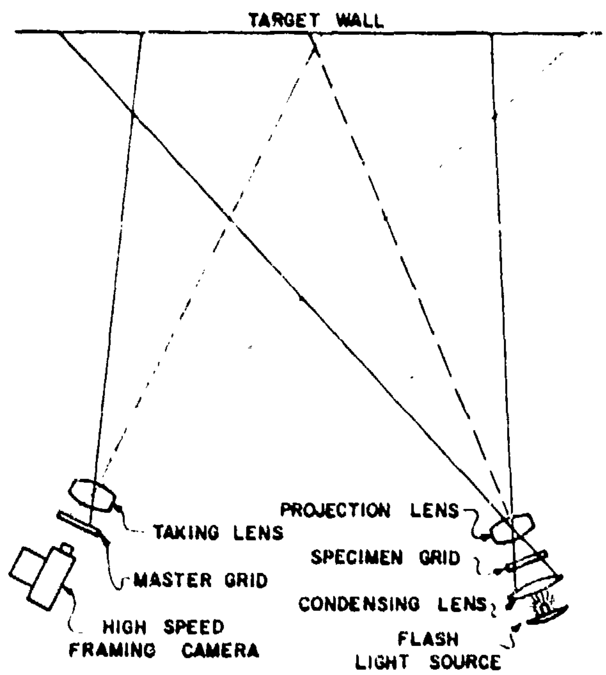

Figure 8. Optical Diagram of Moiré Apparatus.

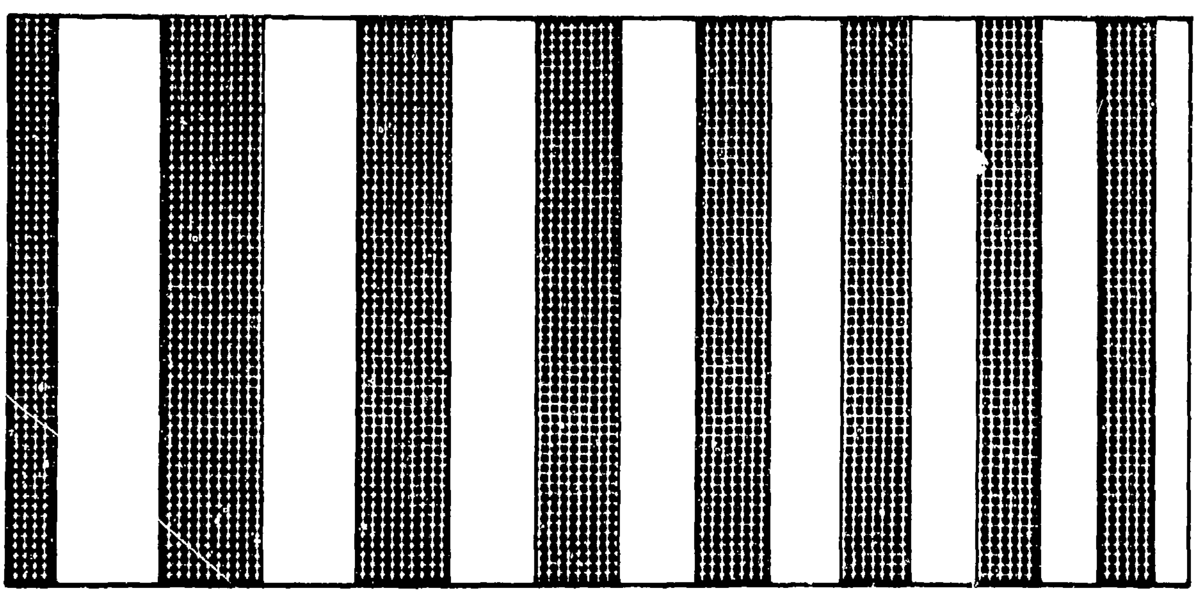

Figure 9. Target Grid.

The target grid was focused through a 75 mm - f/1.5 lens onto a master grid (a second Ronchi ruling). The geometric interference of the master grid with the image of the target grid produced fringes characteristic of the target wall topography. The high speed framing camera recorded this changing moiré pattern as the target was impacted by steel spheres.

A simple equivalent model, valid in the region of the target, was used to describe the moiré optical apparatus. In the model, rays radiated from the projection lens and converged in the taking lens at points on the optic axes very near the front principal planes of the respective lenses. These points were called the moiré source point and the moiré convergence point. The straight line connecting these points defined a reference line for the moiré apparatus called the baseline.

A triangle was defined by the principal axes of the projection and photographic optical elements and the baseline between the moiré source and convergence points. This triangle, illustrated in Figure 10, was called the moiré triangle. To facilitate measurement of the triangle, the principal optical axes were designed to lie parallel to the center lines of the optical benches.

3.2 THEORETICAL ANALYSIS OF MOIRÉ FRINGES

Out-of-plane motion of the target panel caused corresponding changes in the moiré fringe pattern. Measurements of this pattern and the dimensions and orientation of the moiré triangle were used to calculate displacements of the target.

A geometric model of the moiré system, valid in the region of the wall, was constructed to facilitate data reduction. The model, illustrated in Figure 11, also helped clarify the method of fringe information. The model of the optical system was simplified by considering all light to radiate from a source point inside the projection lens. Similarly, reflected light from the target converged to a point inside the taking lens. Equivalent specimen and master grids were drawn between the target and source and the target and convergence points.

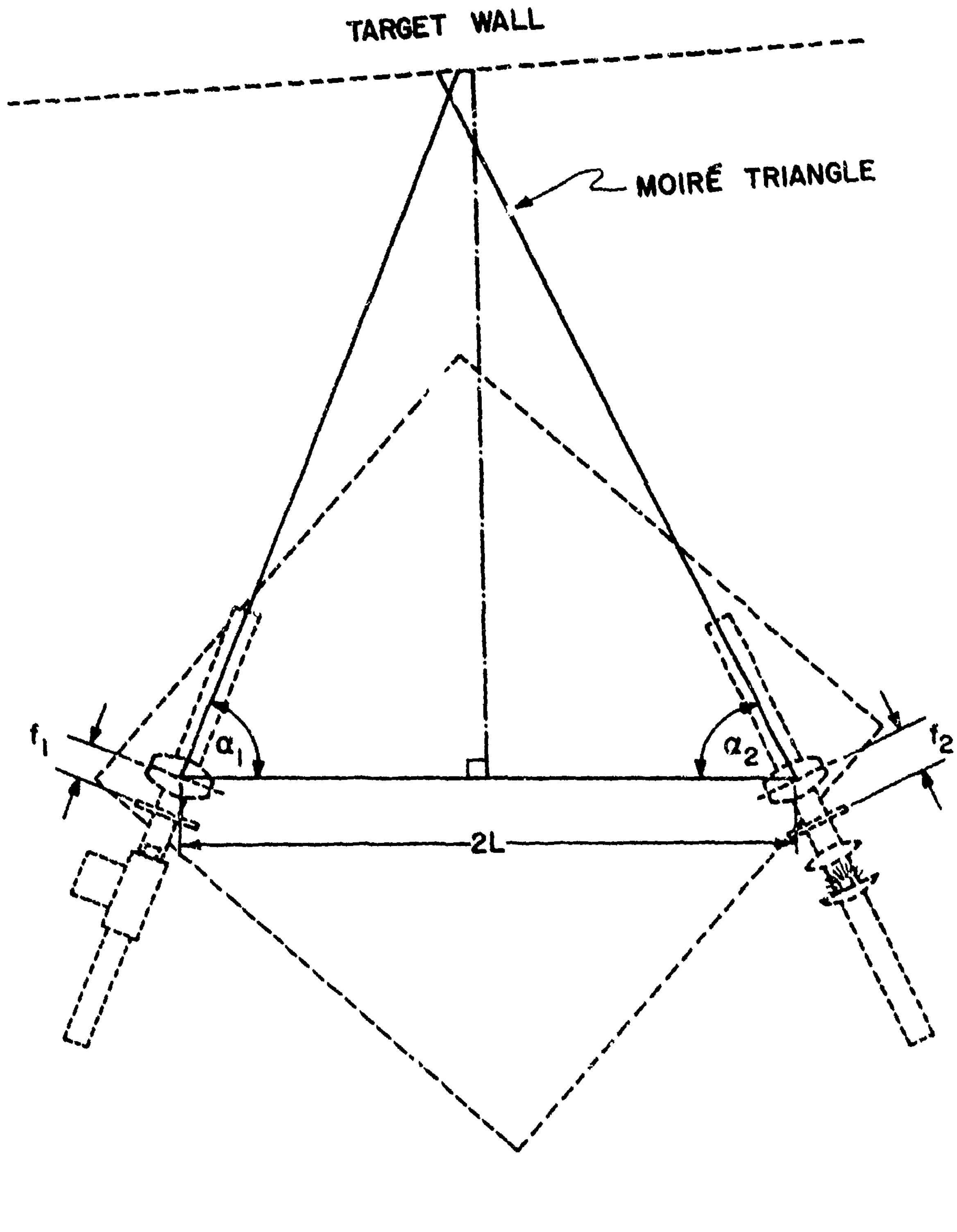

Figure 10. Moiré Triangle.

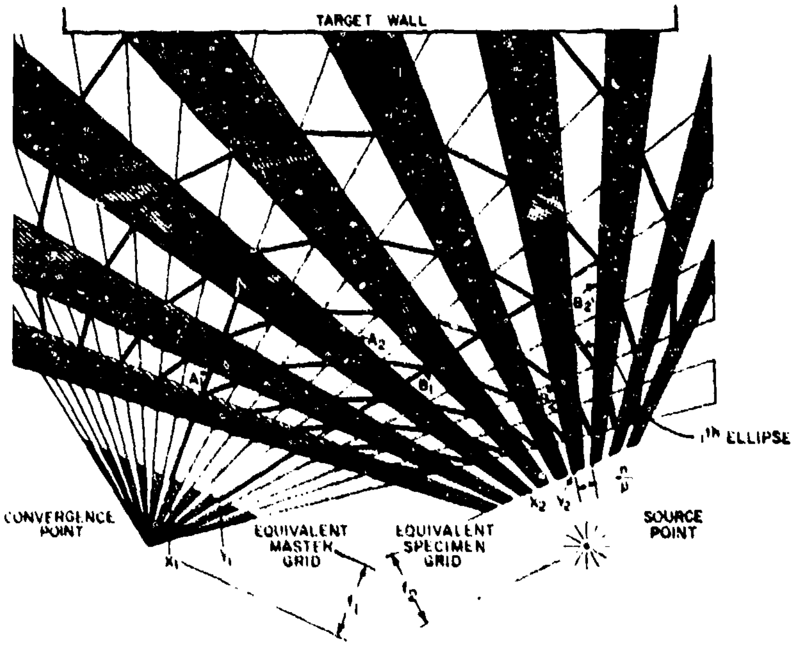

Figure 11. Moiré Geometric Interference Diagram.

The source and convergence points are points at which the rays appear to eminate from or converge to. These points are physically located at the lens principal plane furthest from the grid.

The equivalent specimen grid was positioned a distance f_2 in front of the source point; light and dark rays were produced as light was alternately passed and blocked by this grid. This resulted in the formation on the tank wall of a target grid with a varying pitch. Light from the target grid was alternately passed and blocked by an equivalent master grid located on the photographic optical axis, a distance f_1 in front of the convergence point.

Regions in which light was blocked by the Ronchi rulings are heavily shaded in the illustration. The heavily shaded areas of the master grid are extended as lightly shaded areas to facilitate the description of the model. Any point of the target that falls in the heavily shaded region is not visible

because the light to that point is blocked by the specimen grid. Any point on the target which lies in a lightly shaded region is also not visible because it lies behind an opaque portion of the master grid.

Lines can be drawn which always fall in a heavily or lightly shaded region. One set of these is the segmented lines shown in Figure 11. A surface along one of these lines is totally dark and not visible, and one midway between these lines is relatively bright. However, the target generally intersects several of the segmented curves, and thus appears alternately dark and light.

An observer viewing the master grid from the convergence point sees the combination of the master grid and the superimposed image of the target grid. The result is a moiré fringe pattern which changes as the target undergoes out-of-plane motion. In-plane motion of the target does not affect the target grid and therefore does not produce a change in the fringe pattern.

The straight line segments drawn on the moiré model in Figure 11 connect junction points (opposite corners of heavily and lightly shaded regions) and extend ultimately through both the source point and the convergence point. It can be shown that the junction points for one segmented line lie on a smooth curve. Data reduction was greatly simplified by the deduction that these curved lines are sections of ellipses. This deduction is explained later.

Figure 11 shows the scheme for relating points on the curves to points on the grids. Arbitrary reference points are chosen at X_1 and X_2 on the master and specimen grids. Rays A_1 and A_2 pass through the grids at these points and intersect on the i^{th} ellipse. Rays B_1 and B_2 pass through the grids at Y_1 and Y_2. It is observed that when X_1Y_1 equals X_2Y_2, the rays B_1 and B_2 intersect on the i^{th} ellipse.

Ray B'_2 passes through the specimen grid at a distance n/p from Y_2 (n=1 is illustrated). Ray B'_2 intersects ray B_1 on the $(i+n)^{th}$ ellipse.

The curves illustrated in Figure 11 are called dark curves since their intersections with surfaces produce dark fringes. As the dark fringes are the most convenient for measurement and the dark curves are the simplest to illustrate, they are discussed here exclusively. However, the analysis can be generalized to any ellipse, dark, light, or some fixed intermediate shade.

The analytic description of the dark curves is based on the moiré triangle with the equivalent specimen and master grids drawn normal to the optical axes. To show that the junction points, referred to above, lie along ellipses the moiré construction shown in Figure 12 is used. The moiré triangle and the equivalent grids are shown as bold lines.

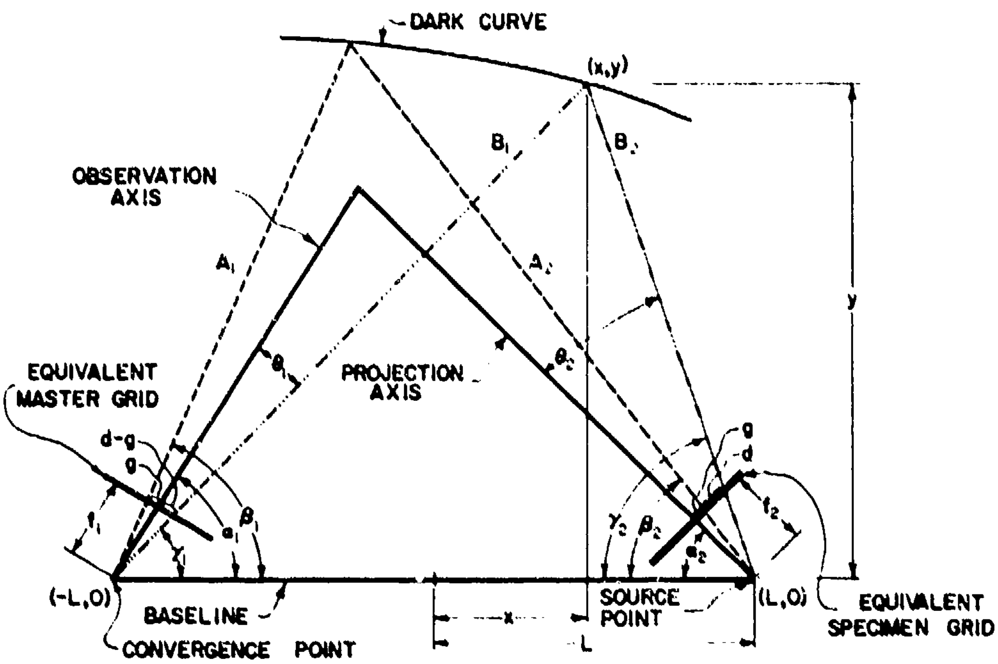

Figure 12. Moiré Analytical Diagram.

The triangle is described by three parameters; the angle between the observation axis and the baseline, α_1, and the angle between the projection axis and the baseline, α_2, and the length of the baseline, 2L.

The location of the dark curves and their characteristics may be formulated as follows. An arbitrary ray, A_2, is chosen (shown as a dashed line in Figure 12) to pass through the equivalent specimen grid at a distance, g, from the projection axis. This ray intersects a complementary ray, A_1, which passes through the equivalent master grid also at a distance g from the observation axis. The distance g can be chosen such that the two rays intersect on one of the dark curves shown in Figure 11. The angles between these rays and the baseline are β_2 and β_1 as shown in Figure 12. A second pair of rays B_2 and B_1, which intersect on this same curve, is illustrated by the dotted lines. For these rays to be on the same curve, they must cross both grids at the same distance, d, from the first rays as demonstrated previously from Figure 11. With respect to an origin at the center of the baseline, the intersection of B_2 and B_1 is the point (x,y). From the geometry, the distance y can be written as

$$y = 2L \frac{\tan \gamma_1 \cdot \tan \gamma_2}{\tan \gamma_1 + \tan \gamma_2} \tag{4}$$

It is necessary to make the proper substitutions in Equation 4 so that y can be written as a function of x and the physically measurable moiré parameters: L, α, α_2, g, f_1, and f_2. The first step is to make the substitutions

$$\begin{aligned} \gamma_1 &= \alpha_1 - \theta_1 \\ \gamma_2 &= \alpha_2 + \theta_2 \end{aligned} \tag{5}$$

where α_1 and α_2 are the base angles of the moiré triangle and the angles θ_1 and θ_2 are taken as positive if they represent clockwise rotations from the optical axis. Next, θ_1 and θ_2

must be replaced. This can be done by writing Θ_2 as a function of Θ_1 and then solving Θ_1. Thus, Θ_2 can be written in terms of Θ_1 by solving the equations

$$\tan \Theta_1 = \frac{d-g}{f_1}$$

$$\tan \Theta_2 = \frac{d+g}{f_2} \tag{6}$$

simultaneously to get

$$\tan \Theta_2 = \frac{2g + f_1 \tan \Theta_1}{f_2} \tag{7}$$

And Θ_1 can be determined from

$$\tan (\alpha_1 - \Theta_1) = \frac{y}{L+x} \tag{8}$$

After expanding $\tan (\alpha_1 - \Theta_1)$ as $(\tan \alpha_1 - \tan \Theta_1)/(1 + \tan \alpha_1 \tan \Theta_1)$, Equation (8) can be written as

$$\tan \Theta_1 = \frac{(L+X) \tan \alpha_1 - y}{y \tan \alpha_1 + (L+X)} \tag{9}$$

Finally, Equation (4) can be rewritten and simplified as

$$y = 2L \frac{Ay^2 + By\,(L+x) + C(L+x)^2}{Dy^2 + Ey\,(L+x) + F(L+x)^2} \tag{10}$$

where the coefficients are defined as:

$$\begin{aligned}
A &= 2g \tan \alpha_1 + f_2 \tan \alpha_2 \tan \alpha_1 - f_1 \\
B &= f_1 \tan \alpha_1 + f_2 \tan \alpha_2 + 2g \\
C &= 0 \\
D &= f_1 \tan \alpha_2 + f_2 \tan \alpha_1 - 2g \tan \alpha_1 \tan \alpha_2 \\
E &= 2g\,(\tan \alpha_1 - \tan \alpha_2) + f_2 - f_1)\,(1 + \tan \alpha_1 \tan \alpha_2) \\
F &= B
\end{aligned} \tag{11}$$

Equation (10) can be rewritten in the form of the general ellipse;

$$\mathcal{A}x^2 + \mathcal{B}xy + \mathcal{C}y^2 + \mathcal{D}x + \mathcal{E}y + \mathcal{G} = 0 \quad (12)$$

where the coefficients are defined as

$$\mathcal{A} = f_1 \tan \alpha_1 + f_2 \tan \alpha_2 + 2g$$

$$\mathcal{B} = 2g (\tan \alpha_1 - \tan \alpha_2) + (f_2 - f_1) (1 + \tan \alpha_1 \tan \alpha_2)$$

$$\mathcal{C} = f_1 \tan \alpha_2 + f_2 \tan \alpha_1 - 2g \tan \alpha_1 \tan \alpha_2$$

$$\mathcal{D} = 0 \quad (13)$$

$$\mathcal{E} = L (f_1 + f_2) (1 - \tan \alpha_1 \tan \alpha_2) - 2g L(\tan \alpha_1 + \tan \alpha_2)$$

$$\mathcal{G} = -L^2 \mathcal{A}$$

Equation (12) shows that the curves in Figure 11 are ellipses, and the coefficients in Equation (13) relate the ellipses to the moiré parameters.

Finge data are reduced by measuring the parameters f_1, f_2, α_1, α_2 , and L. Values of g, separated by 1/p, are used with Equation(8)to calculate the six coefficients of any desired ellipse. The displacement of a point on a moving panel through which a given fringe passes can be easily calculated using Equation (12) if the value of g is known and the x-position of the fringe is measured. Equation (12) is then solved for y, the distance of the fringe from the baseline.

An example of the ellipse generated by the moiré data is shown in Figure 13. These ellipses were based on the following data: $f_1 = 6.51$ cm, $f_2 = 7.34$ cm, $\alpha_1 = 72^\circ$, $\alpha_2 = 62.9^\circ$, L = 66.4 cm, and p = 78.7 lines/cm. Fifty values of g were

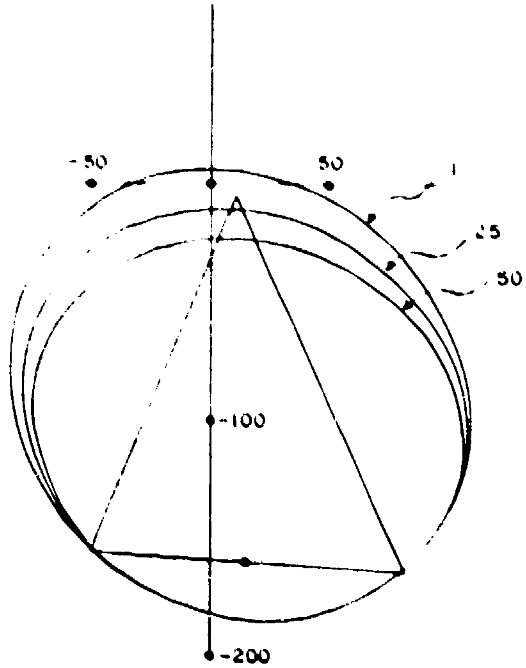

Figure 13. Moiré Ellipses.

used ranging from 0.127 to 0.495 in increments of 1/p. The ellipses were numbered from 1 to 50. Three of the ellipses are illustrated; numbers 1, 25, and 50. Figure 14 illustrates the tank panel shapes calculated for shot FT5B using this method.

3.2.1 Code Description

A computer code was written which uses the theory of moiré ellipses to calculate out-of-plane displacements of panels. As described above, the theory of moiré ellipses relates the fringe positions on the panel to intersections of the panel with a set of elliptic cylinders. These ellipses are completely determined by six parameters: p, the pitch of the Ronchi rulings; 2L, the length of the base of the moiré triangle; α_1 and α_2, the base angles of the moire triangle; and f_1 and f_2, the distances along the optical axes from the base vertices to the equivalent grids. The inputs required to generate the ellipse information and the outputs from the code are described below.

Two types of input are required for this program.

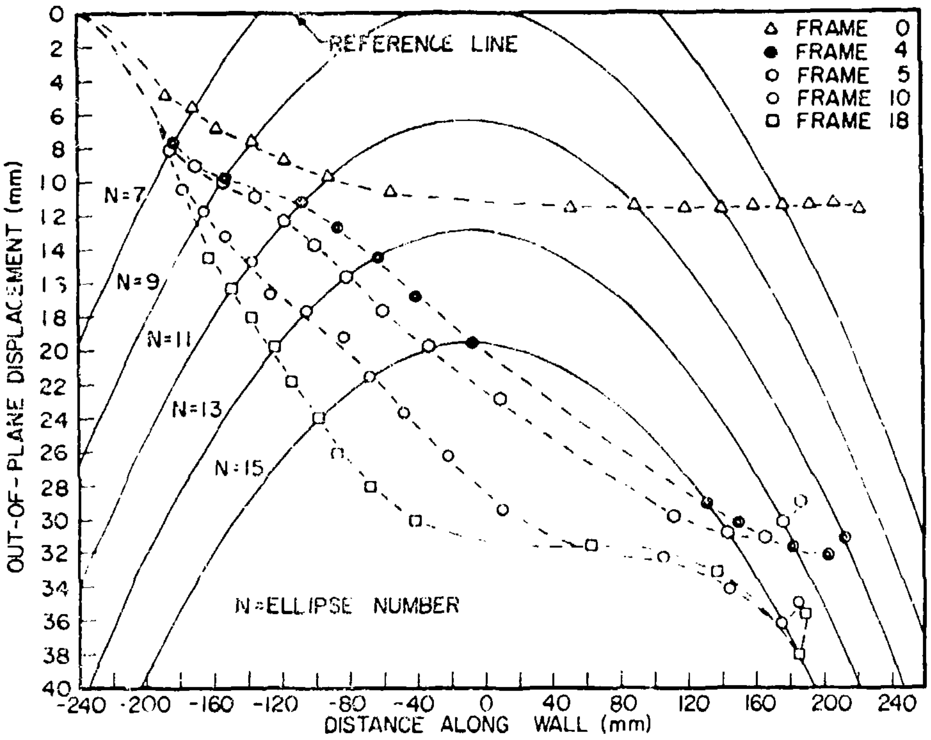

Figure 14. Panel Shapes Calculated for Shot FT5B at Various Times After Impact. Interframe time is 0.165 ms; frame 1 occurs between t=0 and t=0.165 ms.

The first type consists of measured moiré triangle parameters: the pitch of the Ronchi rulings, the base length, and the base angles. The remaining required information are the lengths f_1 and f_2. These distances are difficult to measure but can be determined precisely from fiducial pictures. The fiducial pictures are used to determine the coefficients of two ellipses (called calibration ellipses). Thus, the second type of input consists of the coefficients of the calibration ellipses, and, from these, f_1 and f_2 can be determined. Once the moiré parameters are known, the coefficients of any desired ellipse can be calculated.

The fiducial displacement data are determined by fixing a fiducial to the target wall and determining the intersections of the moiré ellipses with the fiducial. An illustration of the fiducial is shown in Figure 15. Data are required for two

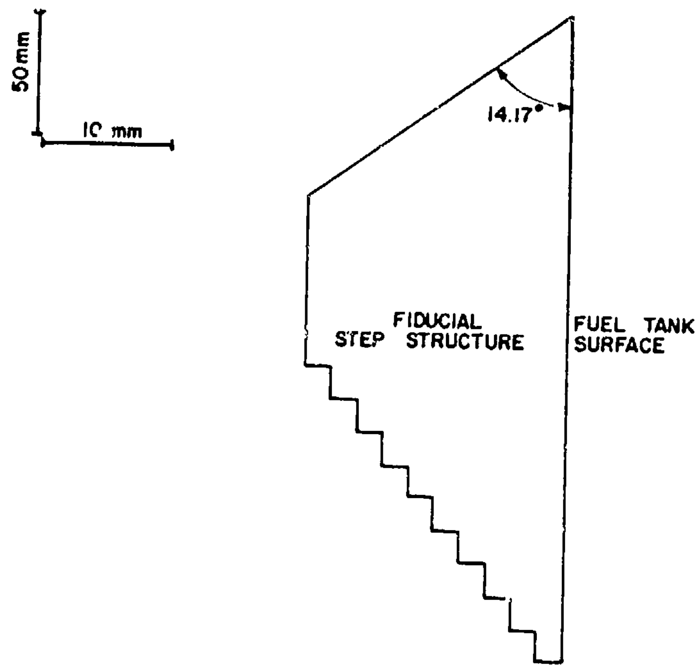

Figure 15. Cross Section of Fiducial Step Structure.

adjacent ellipses which intersect the fiducial (the calibration ellipses). Each set of calibration ellipse data is fit to the equation for an ellipse. Adjacent ellipses are chosen for the calibration data and are arbitrarily numbered as 10 and 11. The numbering system for the ellipses must meet the criteria: 1) the depth covered by the ellipses must be enough for any anticipated wall displacement (50 ellipses are currently used) and, 2) no ellipse can be labeled 0 or less.

An iterative scheme is used to determine the parameters f_1 and f_2. The distance between ellipses is determined from the calibration ellipse equations. The code then determines the f_1 and f_2 which give the measured separation between the ellipses.

The ellipse program consists of the main program, 10 subroutines, and three function subprograms. The main program performs no calculations but calls the appropriate subroutines. The subroutines are described briefly below.

1. READIN

All data is input through the same subroutine. There are two entry points to this subroutine READANG and READCAL.

2. CROSS 1

This routine solves the equation of the two calibration ellipses simultaneously to find their intersections. The result is, in general, a fourth degree equation in y whose zeros correspond to the y coordinates of the intersections of the ellipses. CROSS 1 calls ZEROS to calculate these intersection points, then chooses the desired pair.

3. ZEROS

This subroutine solves a fourth degree equation in y giving the intersection points of the two ellipses. In general, there are four intersection points and the two desired points are selected in CROSS 1.

4. CROSS 2

In the event that the two ellipses have no rotation or translation with respect to the baseline (their coefficients B and D are both zero), the simultaneous solution of the two calibration ellipse equations yields a quadratic equation. CROSS 2 solves this quadratic equation.

5. NEWORGN

The line which connects the intersection of the two ellipses is defined as the baseline for the moirė triangle. The midpoint of the baseline is taken as the origin of the moirė system. The coefficients of the calibration ellipses must be translated and rotated to align with the baseline at the origin. It is only from this reference system that the moire parameters can be used to generate the desired ellipses. NEWORGN locates this origin and executes the translation and rotations.

6. PARAM

This subroutine determines the moirė parameters needed to generate the desired elipses. One of its principal functions is to control the iteration steps in the search for

values of f_1 and f_2 which give the desired separation between ellipses.

7. GENCOF

This subroutine calculates the coefficients for the desired ellipse based on the moiré parameters. The ellipses are numbered from 1 to 50 with the largest ellipse being number 1.

8. REORGN

The coefficients for the 50 ellipses are translated and rotated back to the original reference system of the tank wall by this subroutine.

9. DISPLAC

The displacement of the tank wall, y, at a fringe position is calculated by DISPLAC which solves the equations of the ellipses, given the number of the ellipse and x' position of the fringe.

10. DYCALC

This subroutine calculates the distance between the calibration ellipses. This is used during the iteration procedure used to find the correct values of f_1 and f_2.

3.3 EMPIRICAL METHODS OF MOIRÉ FRINGE DATA REDUCTION

Two methods were developed for empirically converting fringe shift data to panel displacement information. Both are based upon study of the fringes produced on a fiducial surface. The first uses a step surface and the second a wedge surface.

3.3.1 Step Method

The step method of reducing fringe data was found to be the most useful empirical approach. In order to apply this technique a photograph is made of the fringes produced on a reference surface consisting of many steps. Figure 15 is a diagram of the fiducial step structure, and Figure 16 illustrates the fringes on this fiducial structure for shots FT5B and FT26A.

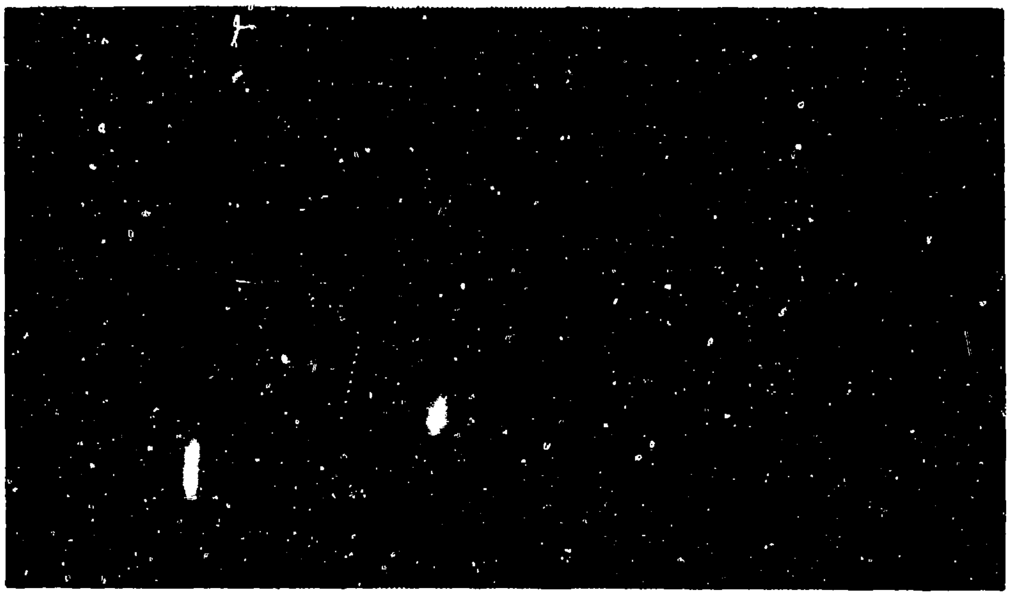

Figure 16. Fringes Produced on Fiducial Step Structure for Shots FT5B and FT26A.

Each fringe in Figure 16 is given a designation, and the positions on the photographic record at which each fringe appears on each step are measured. The positions of the troughs of the fringes are determined from the ramp portion of the fiducial structure. In this way a fringe "map" is prepared. Figure 17 is a demagnified reproduction of the fringe map prepared for Shots FT5B and FT26A. In the figure, values of fringe position, x', measured on the film along a line which was a true horizontal, are plotted against height, h, for each fringe. In Figure 17 the data obtained from the fiducial structure have been extrapolated to obtain fringe location beyond the fiducial structure. The extrapolation is facilitated by the fact that within the accuracy to which the film can be read, the difference in height between any two fringes, Δh, is constant at a given value of x'. In other words, the fringes are all congruent. The error in any value of h in Figure 17 was about one-tenth of a fringe separation; thus, the

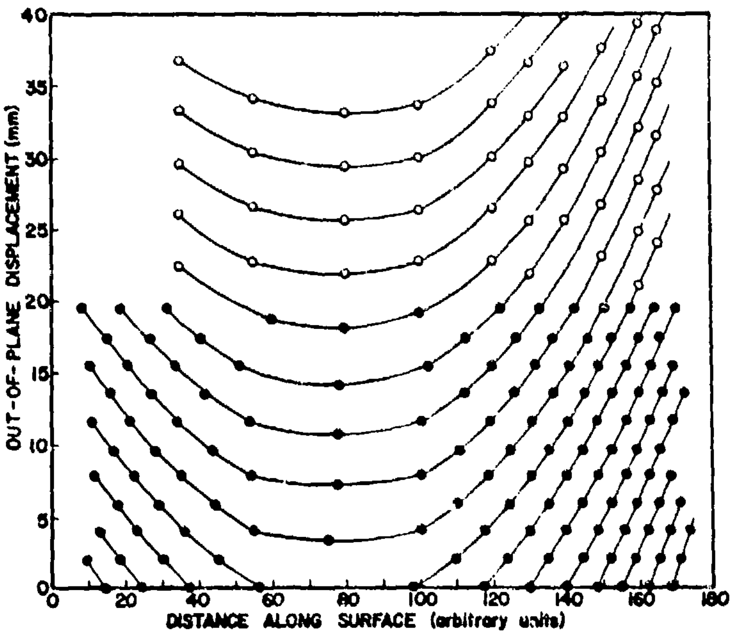

Figure 17. Fringe Map Prepared from Data of Figure 16.

accuracy was taken to be ±0.2 mm (0.008 in).

Data tables were prepared for x' as a function of frame number for each fringe. By use of the fringe map, these data were converted to h values for each fringe in each frame. Thus, the height of the wall surface at fringe locations in each frame was determined. With the aid of photographs of a reference grid, x' coordinates were transformed to x, the horizontal distance parallel to the undeformed target surface. These data are plotted and fit with smooth curves. Such a plot for Shot FT5B data is shown in Figure 18. The fitted curves are drawn dashed in the region of the center of the fringe pattern, where the fringes are farther apart and the panel surface less well determined. Because the data points are fitted with a smooth curve, it is possible that wall deflections of wavelength shorter than ~20 mm will be filtered out in this step.

The error in initial wall shape in Figure 18 is likely to be significant, as the undeflected target panel may have

been at an angle to the reference surfaces of Figure 15. However a few degrees misalignment will have an insignificant effect on relative displacement measurements. The data reported in Section V were obtained by subtracting the pre-impact curve from the various post-impact curves in Figure 18.

3.3.2 Wedge Method

Another method of data reduction is based on the observation that the slope of any fringe on a non-vertical fiducial plane, which intersects the undeformed target plane along a horizontal line, is a linear function of x. Thus, we can write

$$x = k\zeta + b$$

where ζ is the slope of the fringe (referenced to the vertical) and k and b are determined from a fiducial photograph. If the angle between the fiducial plane and the undeformed target

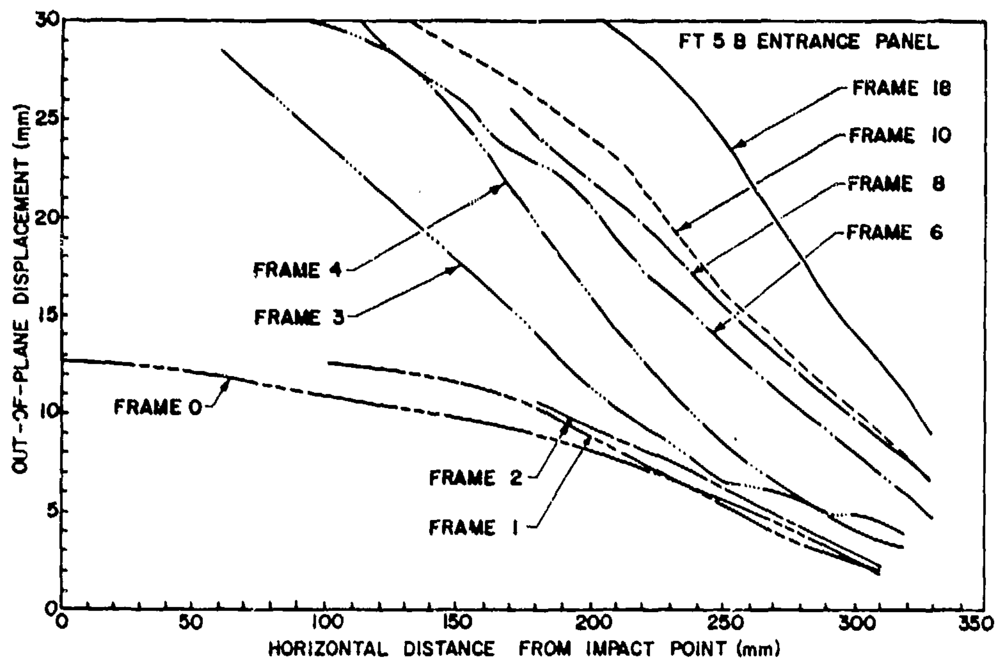

Figure 18. Panel Shapes Derived for Fringe Data from Shot FT5B and Fringe Map of Figure 17. Interframe time was 165μs.

plane is ϕ, it is straightforward to show that for any one fringe

$$\frac{dh}{dx} = \tan \phi \tan \zeta$$

where h and x lie along that fringe. Integrating gives

$$h_{i+1} - h_i = m \tan \phi \; \ln \frac{\cos \frac{(x_i - b)}{c}}{\cos \frac{(x_{i+1} - b)}{c}} , \qquad (14)$$

the displacement increment for a fringe which moves from x_i to x_{i+1} between ith and i+1th frames. Since Equation (14) only gives a fringe's displacement relative to its initial position, no useful information can be obtained until the initial tank surface is determined.

This technique has the advantage over the step method that data reduction involves more arithmetic and less graphical work. Unfortunately; however, the procedure for deducing the initial panel shape is rather imprecise, for it requires adding incremental displacements away from some reference point (such as a bolt). If the panel surface is well surveyed just prior to the shot, and that data is folded into the analysis, the wedge method would probably be as useful as the step method.

SECTION IV
EXPERIMENTS AND RESULTS

4.1 INTRODUCTION

A series of impacts into water-filled tanks was carried out to obtain data relevant to the objectives of the program. Impact velocities were varied from 1.18 to 2.38 km/s. Out-of-plane displacement data were obtained for bare and foam-backed entrance and side panels. Projectile trajectory and shock propagation data were obtained and used as input for the computational treatments. The shots for which data was obtained are listed in Table 1. Three technical areas received special attention during the shot sequence. These are discussed below.

4.1.1 Projectile Annealing

The projectiles used were commercial ball bearings, as described in Section 2.1.1. The initial shots in the program, FT1-FT3, were carried out with the bearings in the as-received condition. However, it was found that these bearings broke up on impact and fragmentation of the projectile in the tank greatly complicated analysis. In order to eliminate this problem, the bearings were annealed. They were annealed by heating to 400°C and holding for three hours followed by a one hour cool to room temperature. A vacuum furnace was used for the annealing process.

4.1.2 High Velocity Techniques

Shots FT10-25 were conducted for the purpose of developing launch techniques for high velocity projectiles. It was desired to achieve velocities in excess of 2.5 km/s. However, the main range was able to accommodate barrels up to only 2 m in length. Within the constraints on barrel length imposed by the range, such high velocities were found to be impossible

TABLE 1. SHOT MATRIX

Shot Number	Projectile diameter (mm)	Projectile impact velocity (km/s)	Target Tanks size A-760ℓ B-28ℓ	Target Tanks entrance panel alloy	Target Tanks foam thickness (mm) B-ballistic S-styrofoam	Data types*	Data damage severity 0-negligible 3-catastrophic
FT2	11.1	1.73	A	7075-T6	0	DF	3
FT3	11.1	1.73	A	7075-T6	0	DF,T,P	2
FT4	14.3	1.61	A	7075-T6	0	DF,T,P	3
FT5	11.1	1.53	A	2024-T3	0	T,P	0
FT5A	11.1	1.58	A	2024-T3	0		0
FT5B	11.1	1.55	A	2024-T3	0	DF	0
FT6	14.3	1.52	A	2024-T3	0	T,P	2
FT7	14.3	1.55	A	2024-T3	76B	DF,T,P	0
FT8	14.3	1.59	A	2024-T3	38B	DF,T,P	0
FT9	14.3	1.57	A	7075-T6	50S	DF,T	0
FT26	11.1	1.49	A	2024-T3	33B	DF	
FT26A	11.1	1.52	A	2024-T3	38B	DF	0
FT27	11.1	2.23	A	2024-T3	33B	DF,T	0
FT28	11.1	2.18	A	2024-T3	35B	DF	0
FT29	11.1	1.18	A	note 1	0	DS,P	note 1
FT30	11.1	2.22	A	note 1	0		note 1
FT31	14.3	1.81	A	note 1	0	T,P	note 1
FT32	14.3	1.77	A	note 1	0	DS,P	note 1
FT33	14.3	1.83	A	note 1	0	DS,T,P	note 1
FT34	14.3	1.83	A	note 1	38B	DS,T,P	note 1
FTA3	11.1	1.21	B	2024-T3	0	S	0
FTA4	11.1	1.60	B	2024-T3	0	S	0
FTA5	11.1	1.94	B	2024-T3	0	S	1
FTA6	11.1	2.21	B	2024-T3	0		3
FTA7	14.3	1.72	B	2024-T3	0		2
FTA9	14.3	1.46	B	2024-T3	0	S	2
FTA10	11.1	2.23	B	2024-T3	0	S	2
FTA11	14.3	1.44	B	2024-T3	12B		0
FTA12	11.1	2.38	B	2024-T3	11B	S	0

note 1: Precut hole in entrance panel. No damage to side panel.

*Data types:
DF - entrance panel displacement
DS - side panel displacement
T - trajectory in fluid
P - pressure in fluid
S - shock speed in fluid

except with one-piece lexan sabots. The one-piece sabots could not be sufficiently retarded in the blast tank, and impacted the target immediately after the ball bearing. Double impacts such as these were deemed not useful for the program. However, techniques were developed for launch of 14.3 mm spheres to velocities in excess of 2.2 km/s. The kinetic energy of such a projectile is 29 kJ. These high energy impacts were employed for study of side panel motion (Shots FT29-34).

4.1.3 Range Instrumentation

The range instrumentation performed generally satisfactorily during the program. The flash x-ray records were found to be extremely valuable for diagnosing projectile performance during sabot-development test shots. A typical radiograph of the projectile in flight is shown in Figure 19. This shows a sphere as it just touches a trigger screen. The sphere is not broken and all sabot parts have been satisfactorily stripped away.

4.2 DESCRIPTION OF PANEL DAMAGE

4.2.1 7075-T6 Aluminum Entrance Panels

In Shots FT2-4, the entrance panels were made from 7075-T6 aluminum alloy. The damage done to these panels by hydrodynamic ram is shown in Figures 20-22. Cracks initiated at the entrance site rapidly and propagated to the edges of the plates. In Shot FT3 one crack traversed the field of view of the framing camera recording the moiré fringe pattern. The average crack velocity over the first 450 mm of motion (to the fasteners) was 310 ± 40 m/s. This is about 1/5 of the sound velocity for water.

4.2.2 2024-T3 Aluminum Entrance Panels

A major purpose of the program was to obtain displacement data for panels. Thus, it was necessary to measure panel motion at several times before failure or measure motion of panels that did not fail. It was also desired to remain in the impact range characteristic of high-velocity fragments,

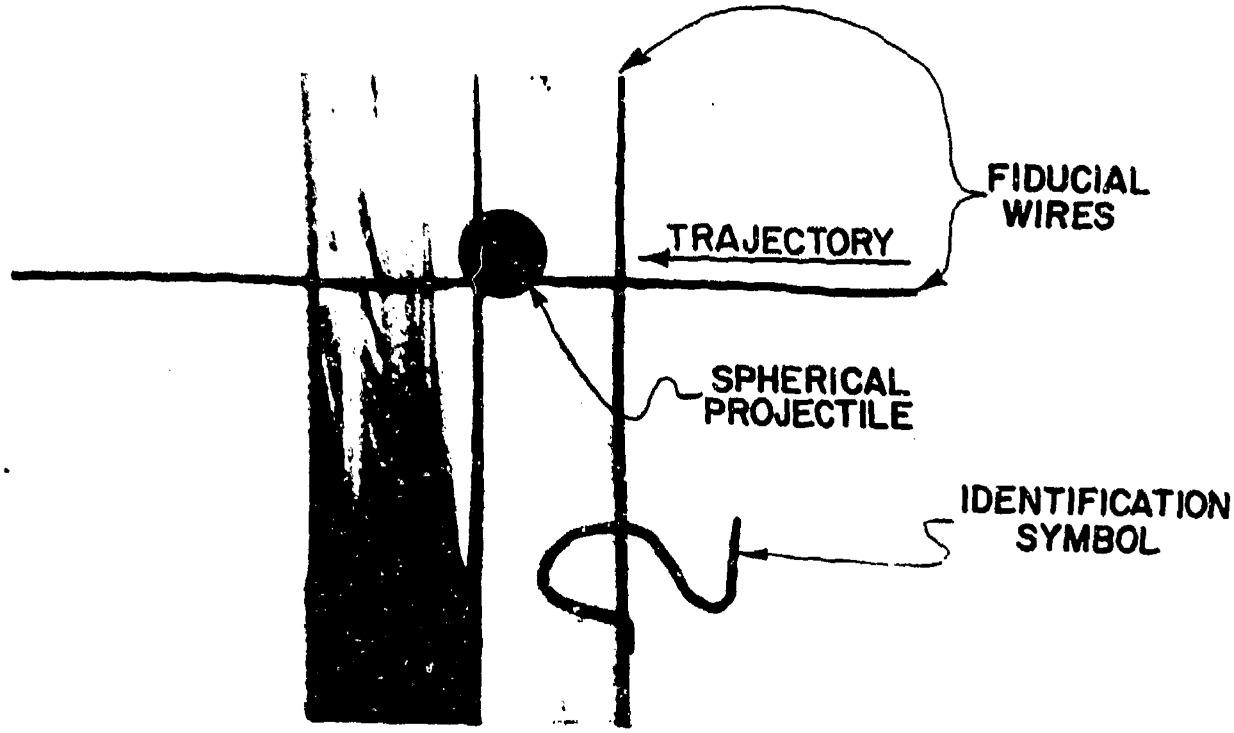

Figure 19. Flash X-Radiograph of 11.1 mm Diameter Projectile As it Contacts the Second Mylar Foil Switch in Shot FT26A.

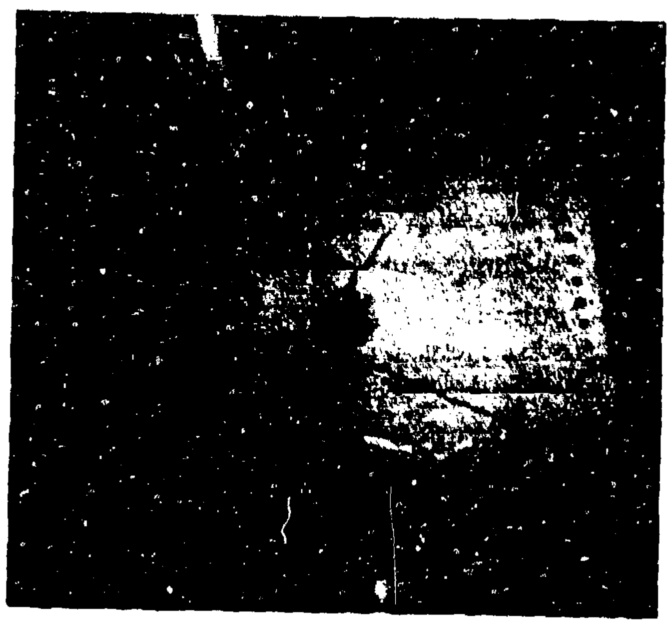

Figure 20. Panel from Shot FT2 after Impact. Panel is 1.6 mm thick 7075-T6 aluminum. Impact was 11.1 mm diameter sphere at 1.73 km/s.

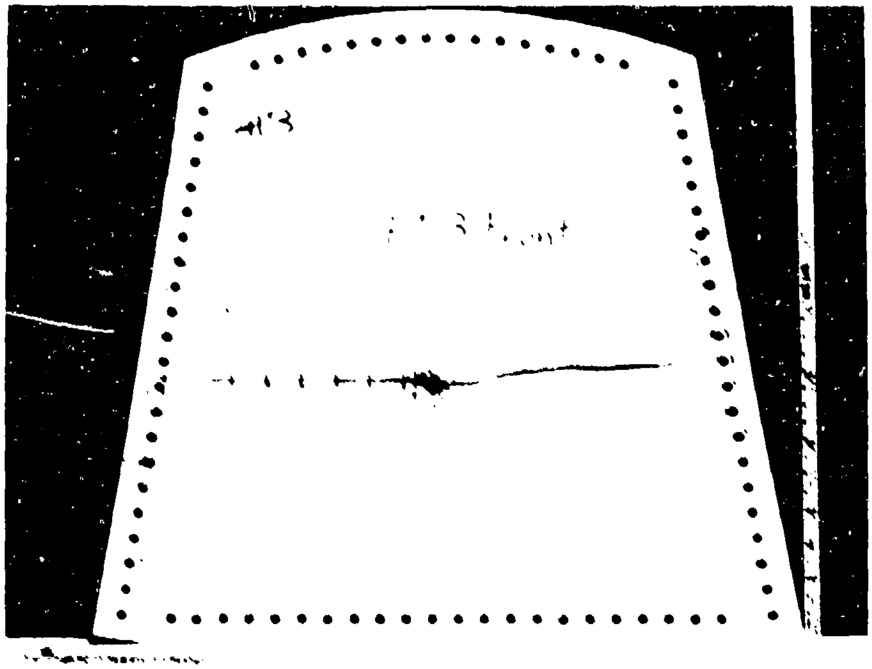

Figure 21. Panel from Shot FT3 after Impact. Panel is 1.6 mm thick 7075-T6 aluminum. Impact was 11.1 mm diameter sphere at 1.73 km/s. Scale divisions on panel are 51 mm apart.

Figure 22. Panel from Shot FT4 after Impact. Panel is 1.6 mm thick 7075-T6 aluminum. Impact was 14.3 mm diameter sphere at 1.61 km/s. Scale divisions on panel are 51 mm apart.

(e.g., 1.5 km/s). Failures were observed to occur very early with 7075-T6 entrance panels. Since 2024-T3 aluminum alloy is substantially more ductile than 7075-T6 alloy, entrance panels made from this material were likely to be more resistant to massive cracking. This turned out to be the case. Therefore, 2024-T3 entrance panels were used for the remainder of the program.

It was found that 11.1 mm diameter spheres at velocities less than about 1.6 km/s did not produce any cracks in the entrance panels. Cracks produced by higher velocity shots against 2024-T3 panels were relatively short. Figures 23 and 24 show examples of damage produced in 2024-T3 alloy entrance panels. A sequence of photographs which illustrate damage caused by increasing projectile velocities with the 28 ℓ tank is shown in Figure 25 through 30. At 1.21 and 1.60 km/s impact velocity no damage resulted (other than the round entrance perforation). At 1.94 km/s small cracks formed at the impact site, but did not grow. At 2.21 km/s four cracks grew which nearly cut the panel into four pieces. At 2.23 km/s the panel was cut into four pieces. However,

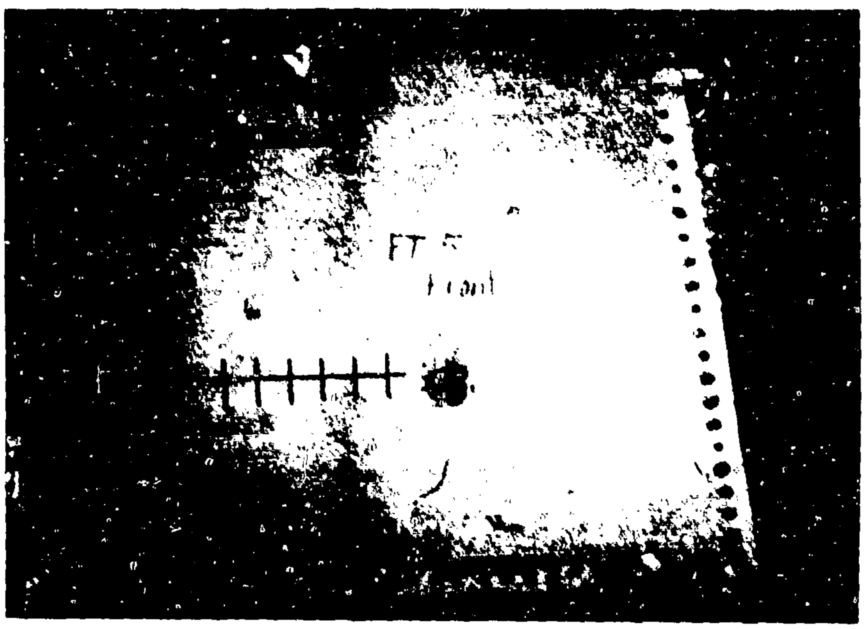

Figure 23. Panel from Shot FT5 after Impact. Panel is 1.6 mm thick 2024-T3 aluminum Impact was 11.1 mm diameter sphere at 1.53 km/s. Scale division on panel are 51 mm apart.

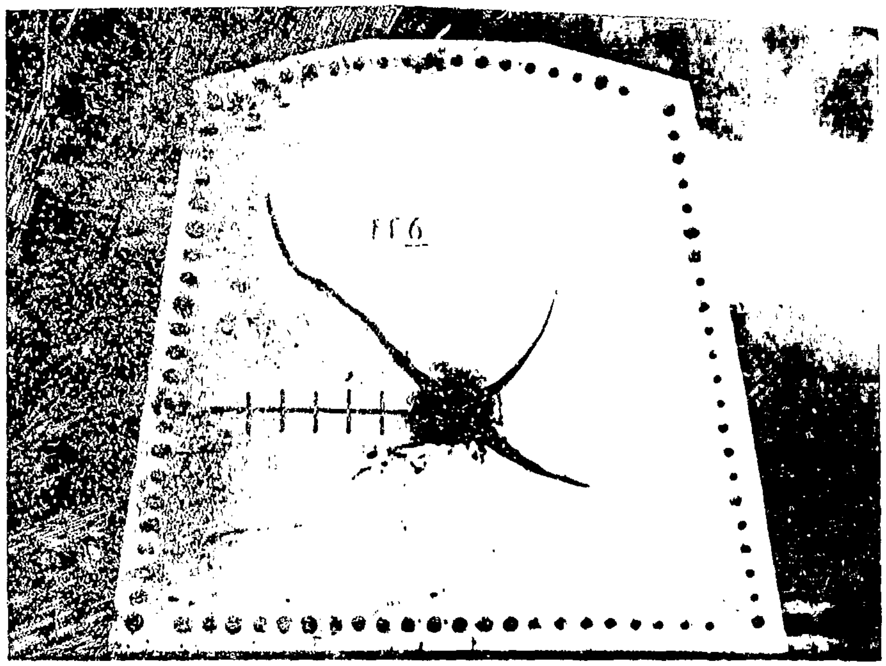

Figure 24. Panel from Shot FT6 after Impact. Panel is 1.6 mm thick 2024-T3 aluminum. Impact was 14.3 mm diameter sphere at 1.52 km/s. Scale Division on Panel are 51 mm apart.

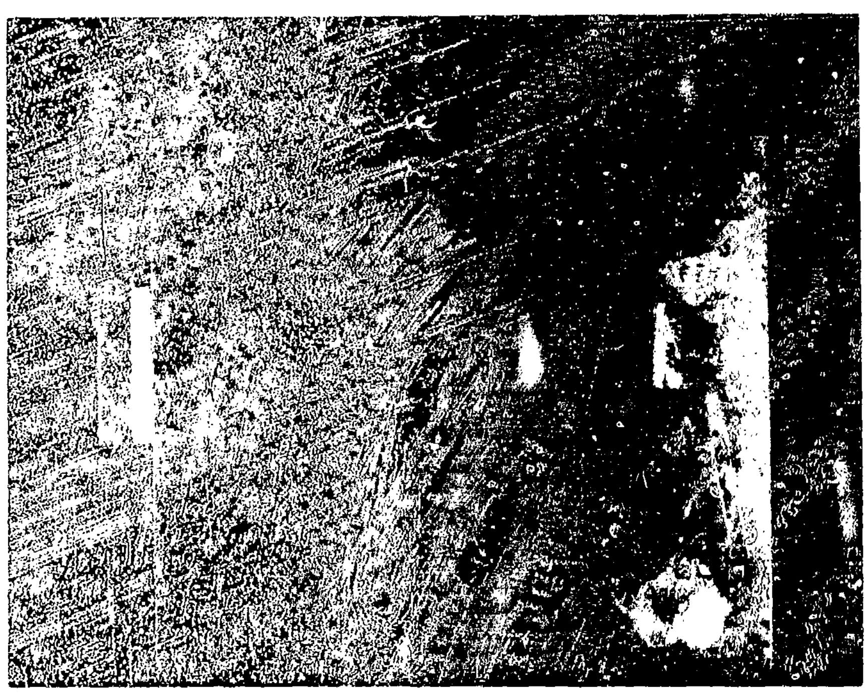

Figure 25. Panel from Shot FTA3, 1.6 mm thick 2024-T3 aluminum. Impact was 11.1 mm diameter sphere at 1.21 km/s.

Figure 26. Panel from Shot FTA4, 1.6 mm thick 2024-T3 aluminum. Impact was 11.1 mm diameter sphere at 1.60 km/s.

Figure 27. Panel from Shot FTA5, 1.6 mm thick 2024-T3 aluminum. Impact was 11.1 mm diameter sphere at 1.94 km/s. Second hole is Caused by Late-Time Impact of Lexan Sabot.

Figure 28. Panel from Shot FTA6 , 1.6 mm thick 2024-T3 aluminum. Impact was 11.1 mm diameter sphere at 2.21 km/s. Circular bend was Caused by Collision with Range Hardware after Impact.

Figure 29. Panel from Shot FTA10, 1.6 mm thick 2024-T3 aluminum. Impact was 11.1 mm diameter sphere at 2.23 km/s.

Figure 30. Panel from Shot FTA12, 1.6 mm thick 2024-T3 aluminum backed with 11 mm AVCO ballistic foam. Impact was 11.1 mm diameter sphere at 2.38 km/s.

at 2.38 km/s with 11 mm of ballistic foam, no cracking occurred. This illustrates dramatically the ability of foam backing to defeat hydrodynamic ram.

In summary, after a hydrodynamic ram event, 2024-T3 alloy entrance panels generally are bulged outward around the entrance hole. Figure 31 shows typical profiles. The tensile strains associated with the enlargement of the entrance hole radius may give rise to cracks which then propagate due to the loading applied during the drag phase.

4.2.3 Effect of Foam Protection on Hydrodynamic Ram Damage

Previous investigations showed that hydrodynamic ram damage to fuel cells can be significantly reduced by the presence of energy-absorbing substances[17-19]. The most promising technique appears to be a semi-rigid foam interface between the wall and the fluid. The usefulness of two types of foams for defeat of hydrodynamic ram was investigated in the present program: AVCO AX 5052-2.5 Thermarest ballistic foam and styrofoam.

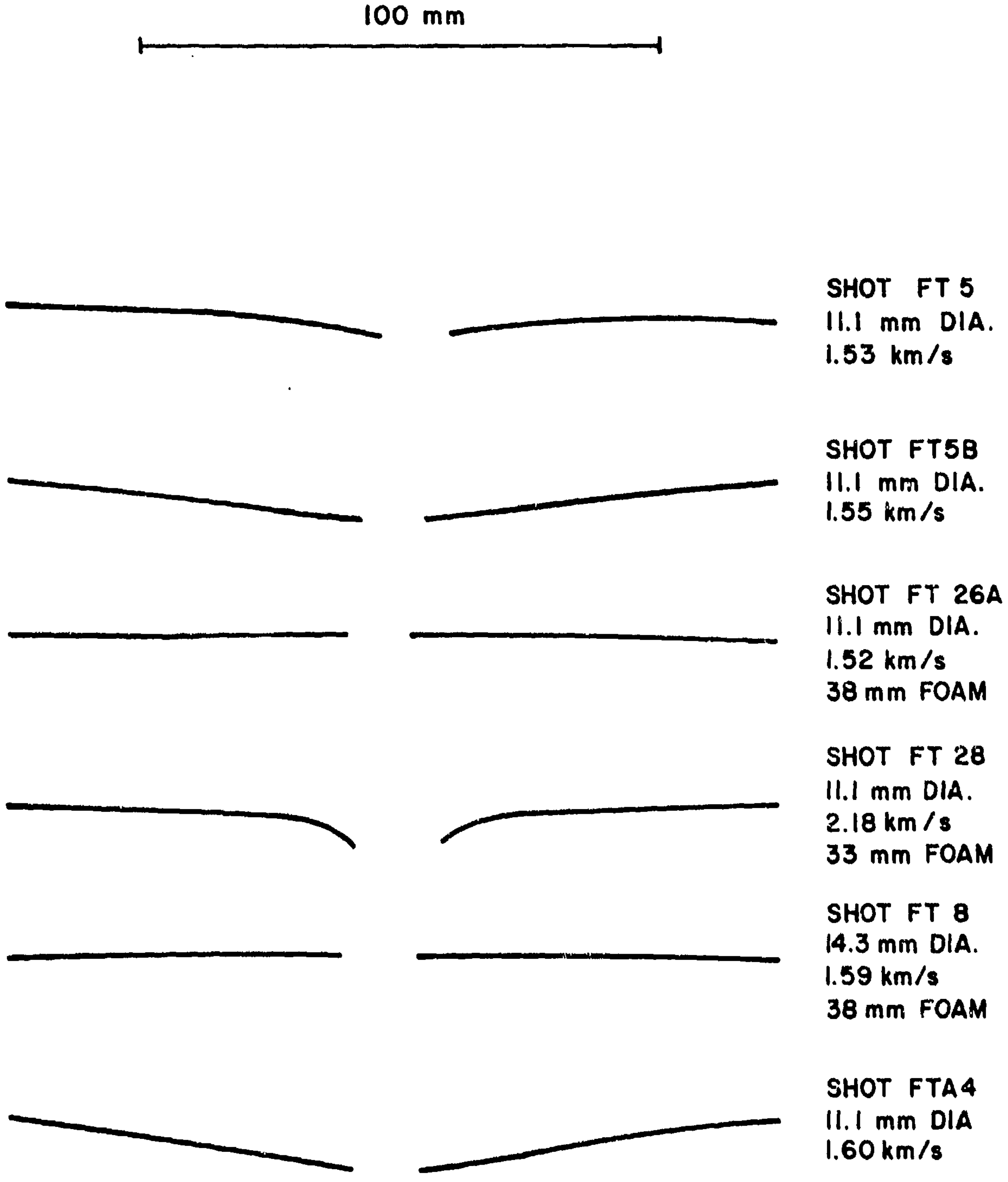

Figure 31. Profiles Through Impact Hole of Selected 2024-T3 Alloy Entrance Panels.

Most tests of foam were performed with the AVCO ballistic foam. In Shots FT7, FT8, FT26, FT26A, FTA11, and FTA12, varying thicknesses of AVCO foam were bonded to the entrance panel with epoxy. Initially 76 mm thick foam was employed, and that thickness proved extremely effective. The foam thickness was reduced in successive shots to determine a minimum useful foam thickness. In the final shots, the foam thickness was only 11 mm and yet the hydrodynamic ram mechanism was completely defeated. None of the foam-backed entrance panels were significantly damaged in these experiments. Comparison of Figure 30 with Figure 29 provides an indication of the effectiveness of a thin foam layer behind the entrance panel. The same projectile which destroyed a panel with no foam backing caused insignificant damage to the panel after it was protected with an 11 mm thickness of rigid foam.

The effectiveness of styrofoam was evaluated in Shot FT9. The entrance panel was 7075-T6 alloy. The extensive cracking which occurred on bare walls was completely eliminated by 50 mm of styrofoam.

Post shot observations of the foam-backed panels revealed that the foam was typically crushed within a radius of 120 to 150 mm centered on the impact hole in the panel. The severely damaged region was only 10 to 30 mm in radius on the side of the foam adjacent to the fluid. The large damage next to the panel probably resulted from dissipation of the shock wave in the foam. Fluid shock effects are reduced when the projectile strikes the foam backed fluid because the peak shock pressure is lower (see Figure 1), and the foam permits rapid release of the shock presures.

Some insight into the mechanics of projectile, foam, panel, and water interactions can also be obtained from analysis of Figure 31. Note that the permanent deformation which resulted in FT5, FT5B, and FTA4 (which represent nearly identical impact configurations) was completely absent in FT26A (the same impact configuration with the addition of foam). The relatively long wavelength of the deformation suggests

that it is caused by drag phase pressure. Therefore, the chief effect of the foam was apparently to rigidly shield the wall from the drag phase pressure pulse. As the ball size was increased (FT8), the response of foam-backed panels did not change. In the high velocity Shot FT28, large local deformation occurred. This was probably due to the shock phase pressure, which increases with impact velocity, and which propagates for a short distance into the foam. However, the lack of a larger wavelength bulge suggests that the overall rigidity of the foam shielded the entrance panel from cavity phase pressure. There are, therefore, two mechanisms by which the rigid foam defeats hydrodynamic ram at entrance panels: the crushing at the foam attenuates the shock pressure; and the flexural rigidity of the foam spreads the drag phase pressure.

One shot was carried out with ballistic foam on a side panel, Shot FT34. No side panel failures or large plastic deformations had been observed, and thus it was felt that a closer trajectory would be required to evaluate the foam. The trajectory was moved horizontally about 150 mm closer to the observed panel. No failure occurred, but moiré fringe data were obtained. The displacement results are reported in Section 4.3.

Because of the long trajectory in the water and low projectile masses, rear panels were only occasionally impacted with sufficient force to cause failure. The ability of foam to reduce rear panel damage was nevertheless investigated in Shots FT31-FT34. In all four shots the rear panel was cracked but not punctured. Neither 50 mm of styrofoam nor 12 mm of ballistic foam appeared to reduce the extent of cracking. The difference in foam effectiveness for entrance and side panels may be due to the fact that the fluid velocity vector is parallel to or away from the entrance panel but perpendicular to or toward the exit panel.

4.3 MEASUREMENT OF WALL DISPLACEMENT

Out-of-plane displacement data were reduced for six shots, as of the writing of this report. The shots reduced

were FT2, FT5B, FT6, FT8, FT26A and FT33. FT33 was a side panel shot but the remaining five were entrance panel shots. The "base" shot was FT5B; a 11.1 mm diameter sphere impacted at 1.53 km/s against a 2024-T3 aluminum panel. FT2 was similar to FT5, except the panel was 7075-T6 aluminum. FT26A was similar to FT5, except the panel was backed by 38 mm of ballistic foam. FT6 was the same as FT5, except that a 14.3 mm diameter sphere was used. FT8 was the same as FT5 except a 14.3 mm diameter sphere was used <u>and</u> the panel was backed by 38 mm of ballistic foam.

4.3.1 Entrance Panel Measurements

Figure 32 illustrates 8 successive frames from the base Shot FT5B. The target point is the cross on the tank surface in frame -1. Impact occurs between the two frames labeled -1 and 0. The interframe time is 164 μs. In frame -1, displacement of the center of the panel has caused the center of the fringe pattern to shift. By frame 2, the impact flash has dissipated sufficiently to view most of the target. Starting in frame 3 and continuing through frame 5 a discontinuity in the fringe positions appears to propagate away from the impact zone. In frames 5 to 7, a second discontinuity appears to follow the first. In later frames reflections of these motions from the bottom of the tank are apparent.

The moiré fringe records for this shot were read along horizontal and vertical lines through the impact point. The data reduction technique used was that described in Section 3.3.1. Figures 33 and 34 show the tank displacement determined from the moiré fringe data. As discussed in Section 3.3, the tank displacement given in the figures may be lacking some high spatial frequences, since data is only available at fringe positions and, during the data reduction procedures, a smooth curve was drawn through the measured fringe positions. The accuracy in displacement, $\delta(\Delta h)$, was generally $\pm$ 0.4 mm. The accuracy was somewhat reduced over the panel region on which the center of the fringe pattern occurred because fringes are farther apart. For example, for $100 \leq x \leq 200$ mm, $\delta(\Delta h)$ is probably about 0.5 mm. The effect of the accuracy in Δh is

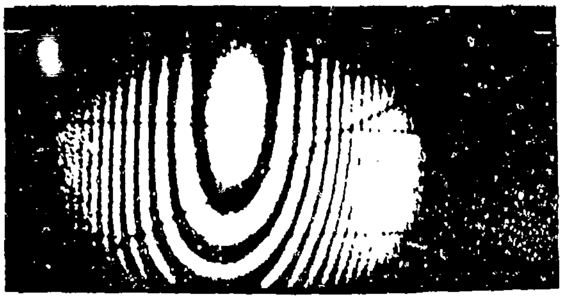

Frame -1 (before impact)

Frame 0 (after impact)

Frame 1

Frame 2

Frame 3

Frame 4

Frame 5

Frame 6

Figure 32. Framing camera pictures of moiré fringes from shot FT5B. Interframe time is 156 μs.

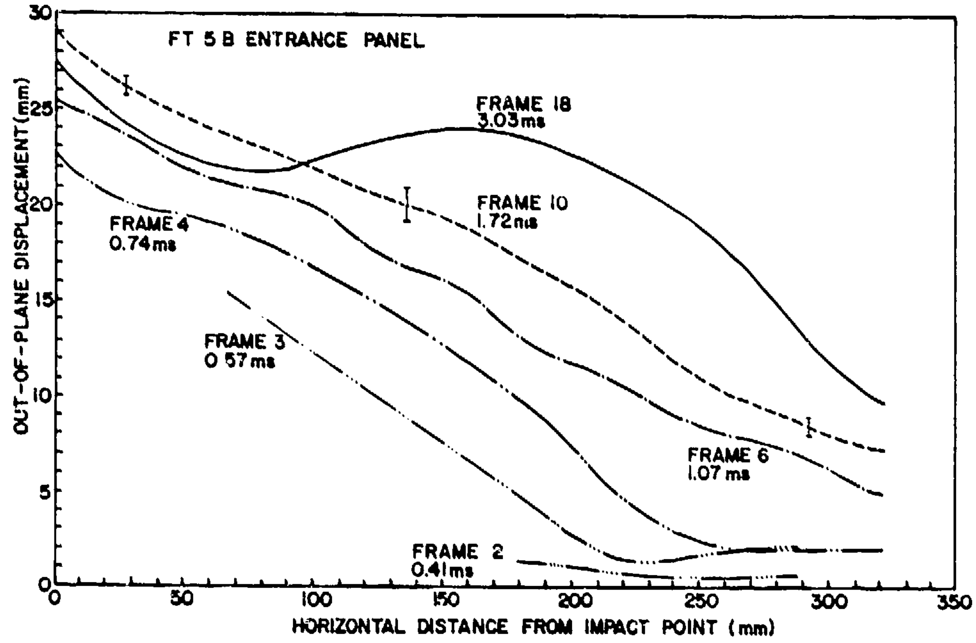

Figure 33. Out-Of-Plane Displacement (Measured from Pre-Impact Surface). Error bars indicate approximate uncertainty in displacement. Time uncertainty is ± 0.08 ms. Data are for entrance panel from Shot FT5B, an 11.1 mm diameter ball striking a 2024 T3 panel at 1.53 km/s.

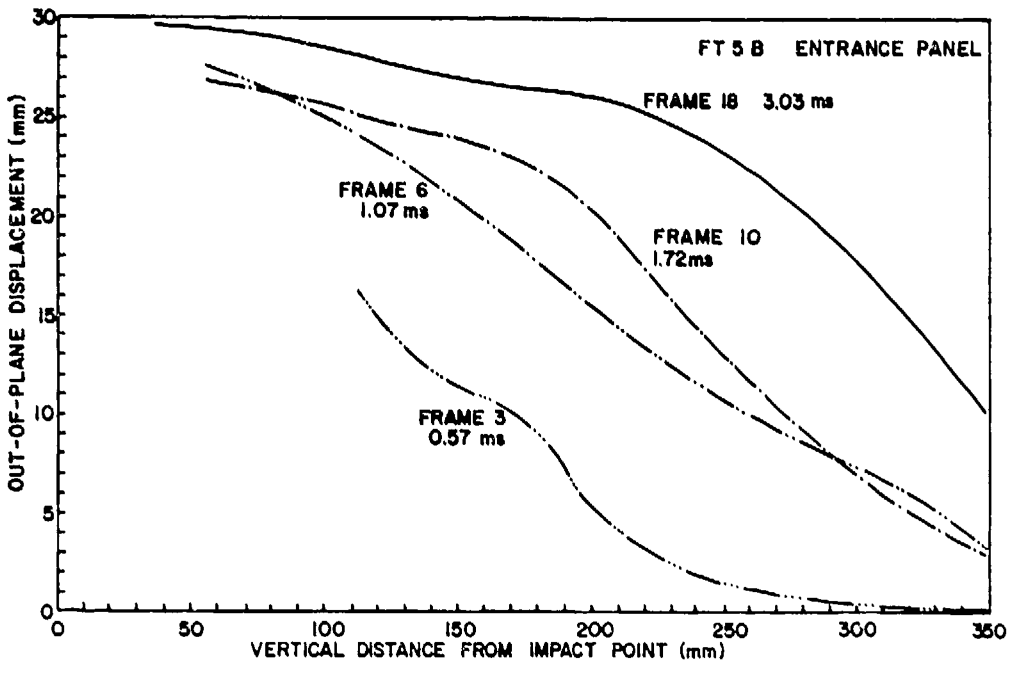

Figure 34. Same as Figure 33 Except for Vertical Line Through Impact Point.

that the curves in Figures 33 and 34 may be redrawn within bands of $\pm \delta$ (Δh) without conflicting with the moiré fringe data.

In FT5B the maximum displacement at the impact zone was approximately 29 mm, which was attained at about 1.7 ms after impact. Outward movement of the flanks of the panel continued beyond this time, while the peak displacement began to fall. Deflections on the line below the impact point are about 10% higher than at comparable distances measured horizontally from the impact point. Motion near the panel edges starts between 200 and 400 μs after impact. The "pucker" of the panel in the entrance hole region was established by 740 μs after impact, but was absent before this time. The initiation of major motion of the target panel propagates across the panel with a speed of 300 ± 30 m/s. A smaller negative displacement wave appears to propagate to about 100 mm distance at about 1 ms after impact with a speed of 122 ±24 m/s. (Displacement front motion can be measured directly from the moiré framing camera pictures).

Displacement data for the corresponding foam shot, FT26A, are presented in Figures 35 and 36.

The panel motion in FT26A was smaller in this shot. Peak displacement was only about 22 mm compared to 29 mm for FT5. Initial panel movement was considerably slower, but the maximum displacement in the impact zone was still reached at about 1.7 ms after impact. The curvature of the outward moving panel was also less in this shot. The major motion discontinuity was of smaller amplitude than that of FT5B, and only propagated at 170 ±14 m/s.

Figure 37 presents the displacement data for a similar shot with a larger diameter sphere, FT8. The profiles are very similar to those of Figure 36. FT6 is the companion large projectile shot with no foam. That panel failed, as is shown in Figure 24. The displacements along the horizontal scale to the left of the impact site are shown in Figure 38. In this shot, impact flash from a foil switch obscured the area within 75 mm of the impact site. Beyond that region, in spite of the failure which occurred elsewhere, the displacement along this parti-

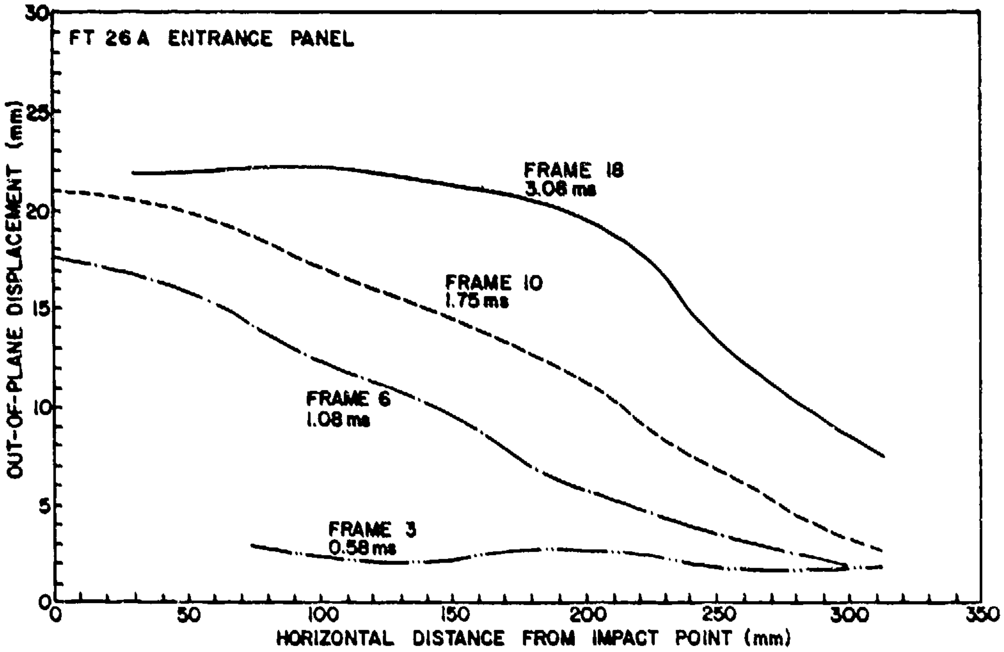

Figure 35. Same as Figure 33, But for Shot FT26A, an 11.1 mm Diameter Sphere Striking a 2024-T3 Panel Backed by 38 mm of Ballistic Foam at 1.52 km/s.

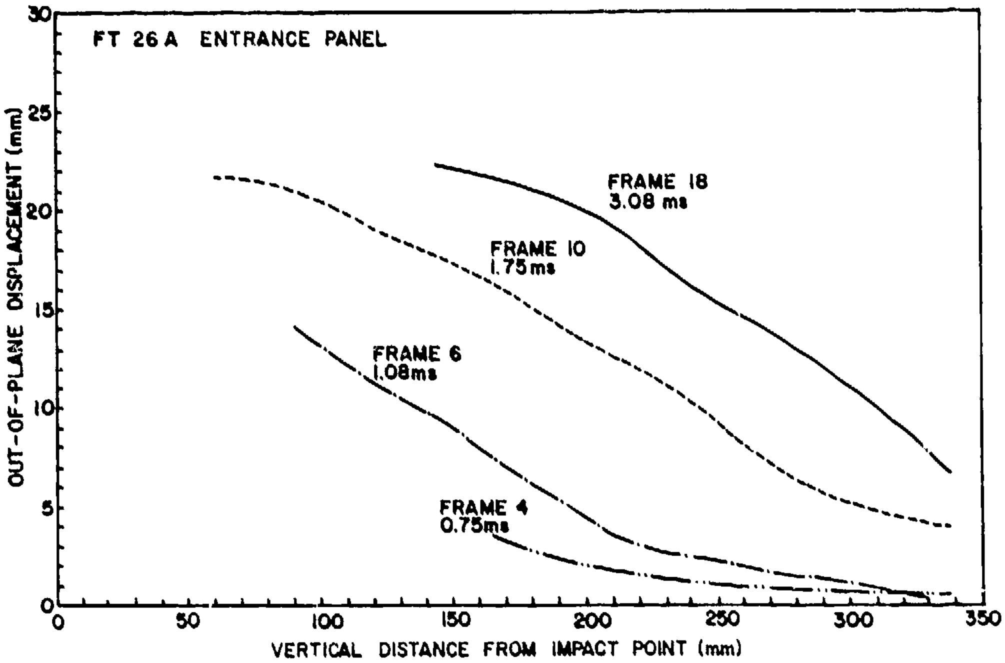

Figure 36. Same as Figure 35, But for Vertical Line Through Impact Site.

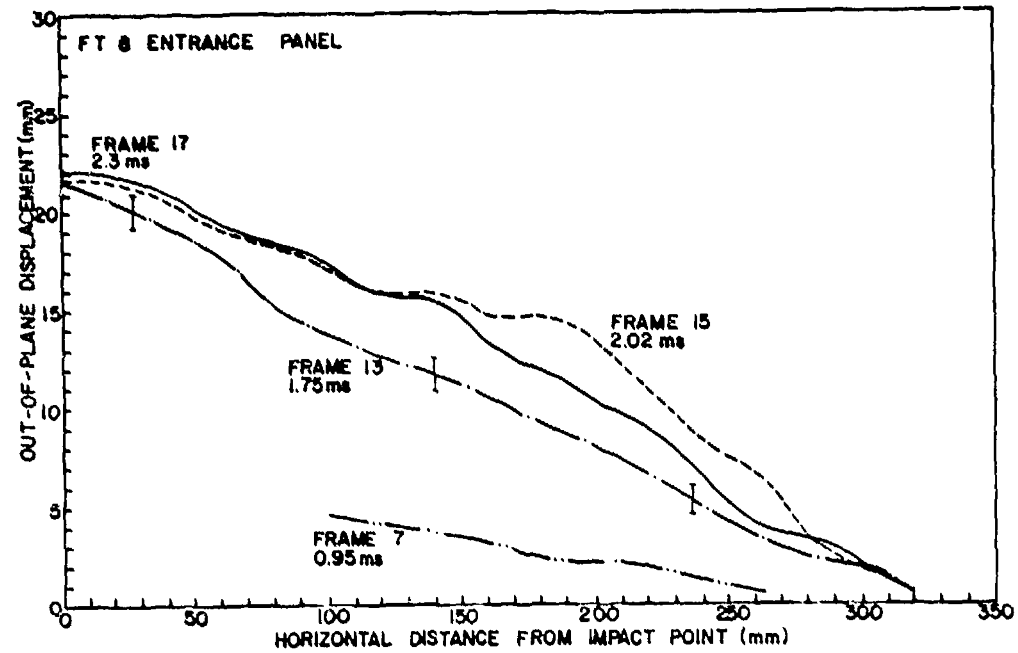

Figure 37. Same as Figure 33, Except for Shot FT8, a 14.3 mm Diameter Sphere Striking a 2024-T3 Panel Backed By 38 mm of Ballistic Foam at 1.59 km/s.

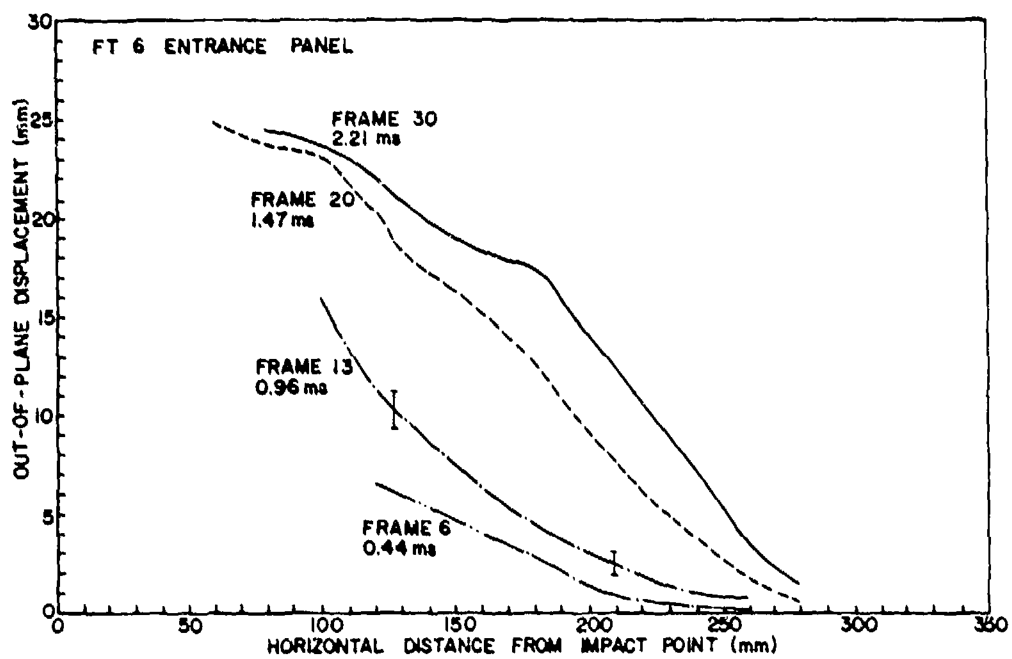

Figure 38. Same as Figure 33, Except for Shot FT6, a 14.3 mm Diameter Sphere Striking a 2024-T3 Panel at 1.52 km/s.

cular line is qualitatively similar to that of the unfailed panel of FT5. The major difference between these two shots is the relatively smaller amount of displacement near the fasteners of the failed panel.

Figure 39 presents entrance panel displacement data from FT2. This panel was made of 7075-T6 aluminum; a post-impact photograph of the failed plate is shown in Figure 20. For early times near the entrance region the movement is similar to that of Figure 35. However, the peak displacement at late times is very large, due to petalling.

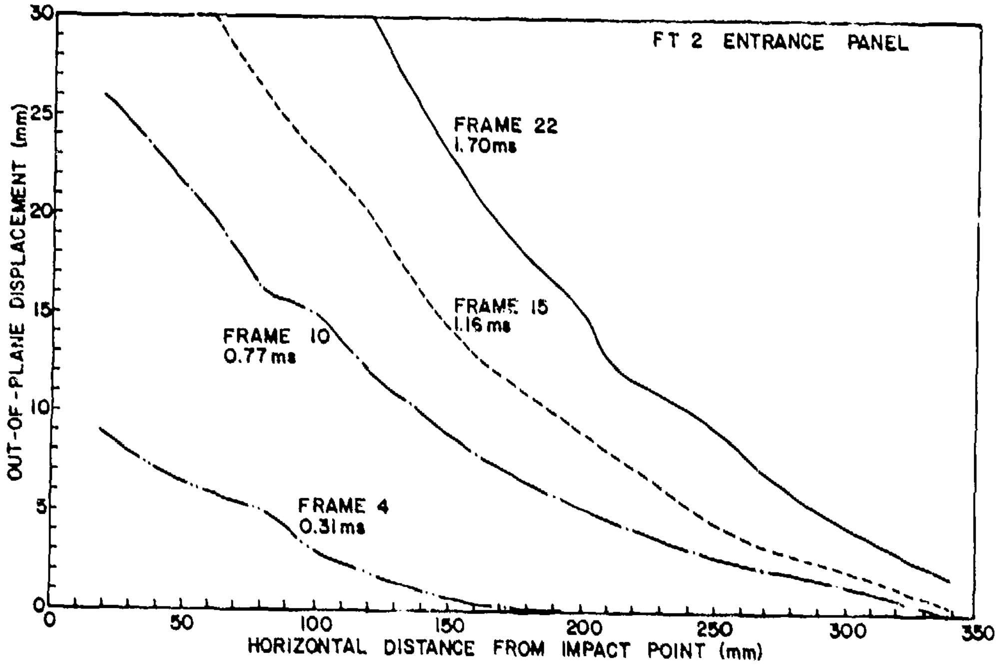

Figure 39. Same as Figure 33, Except for Shot FT2, an 11.1 mm Diameter Sphere Striking a 7075-T6 Panel at 1.73 km/s.

4.3.2 Side Panel Measurements

Moiré fringe data from the side-panel Shot FT33 were reduced along a horizontal line at trajectory height by the technique described in Section 3.3.1, and along a horizontal line 150 mm below trajectory by the technique described in Section 3.3.2. The out-of-plane panel displacement at various times are displayed in Figures 40 and 41. The origin on these plots is the center of a fastening bolt.

The uncertainty in wall shape in Figures 40 and 41 is about ± 0.25 mm. Thus, the inflection points in the central regions of the displacement curves seem to be real. The dip in the curves near the fasteners is believed to be due to twisting of the edge angle bracket caused by front panel loading.

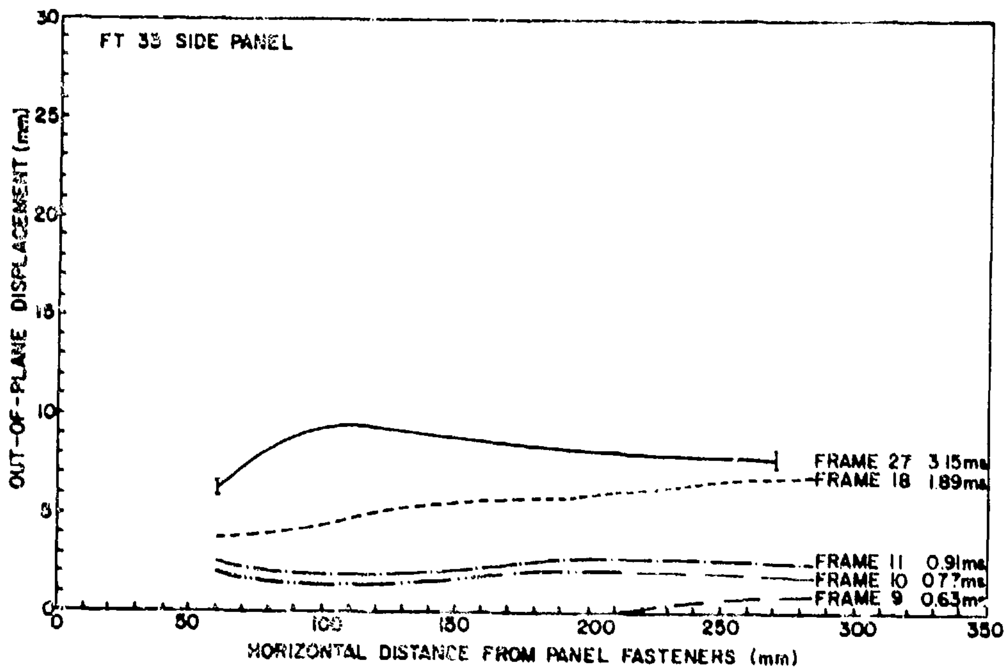

Figure 40. Same as Figure 33, but for Side Panel of Shot FT33, a 14.3 mm Diameter Sphere Striking at 1.83 km/s.

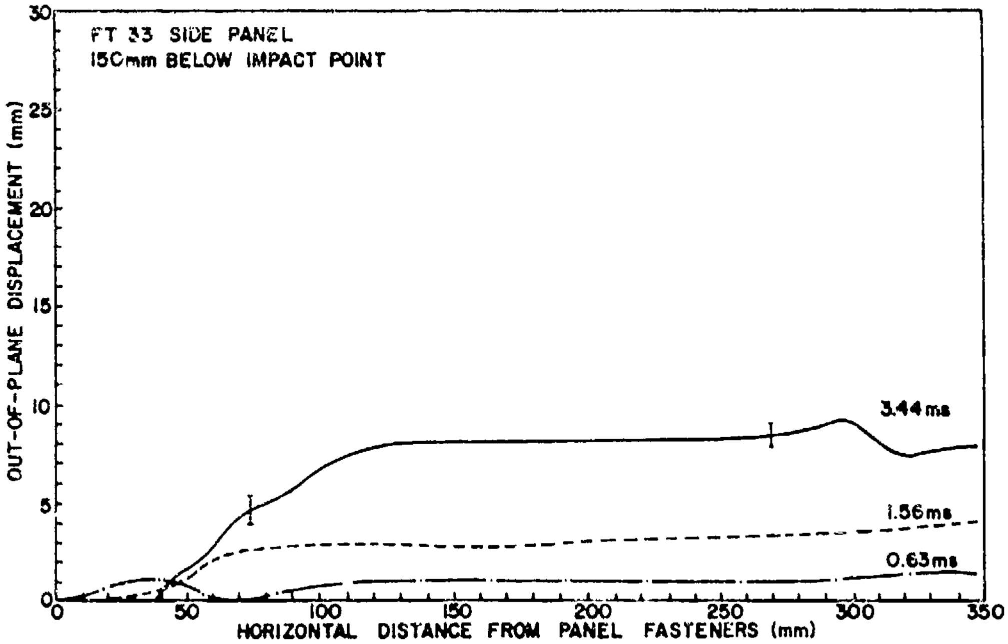

Figure 41. Same as Figure 40, Except for a Line 150 mm Below Trajectory.

The peak displacement experienced by side panels is not reached until relatively late--about 7 ms in FT33 and 6 ms in FT32. This is long after the projectile has exited the tank. The maximum displacement observed is about 25 mm. This is comparable to the entrance panel displacement in FT5B, even though the energy of the projectile in shot FT33 was almost three times that of the projectile in shot FT5B.

4.4 PROJECTILE DRAG DETERMINATION

Figures 42 and 43 show sequences of frames from typical film records of projectile and cavity motion in fluid filled tanks. Data were available from the large tank shots, (as shown in Figure 42) and also from the shock tank shots (as shown in Figure 43) at early times. These data were used to determine the projectile velocity and the cavity expansion and decay rates. The projectile velocity was used to determine

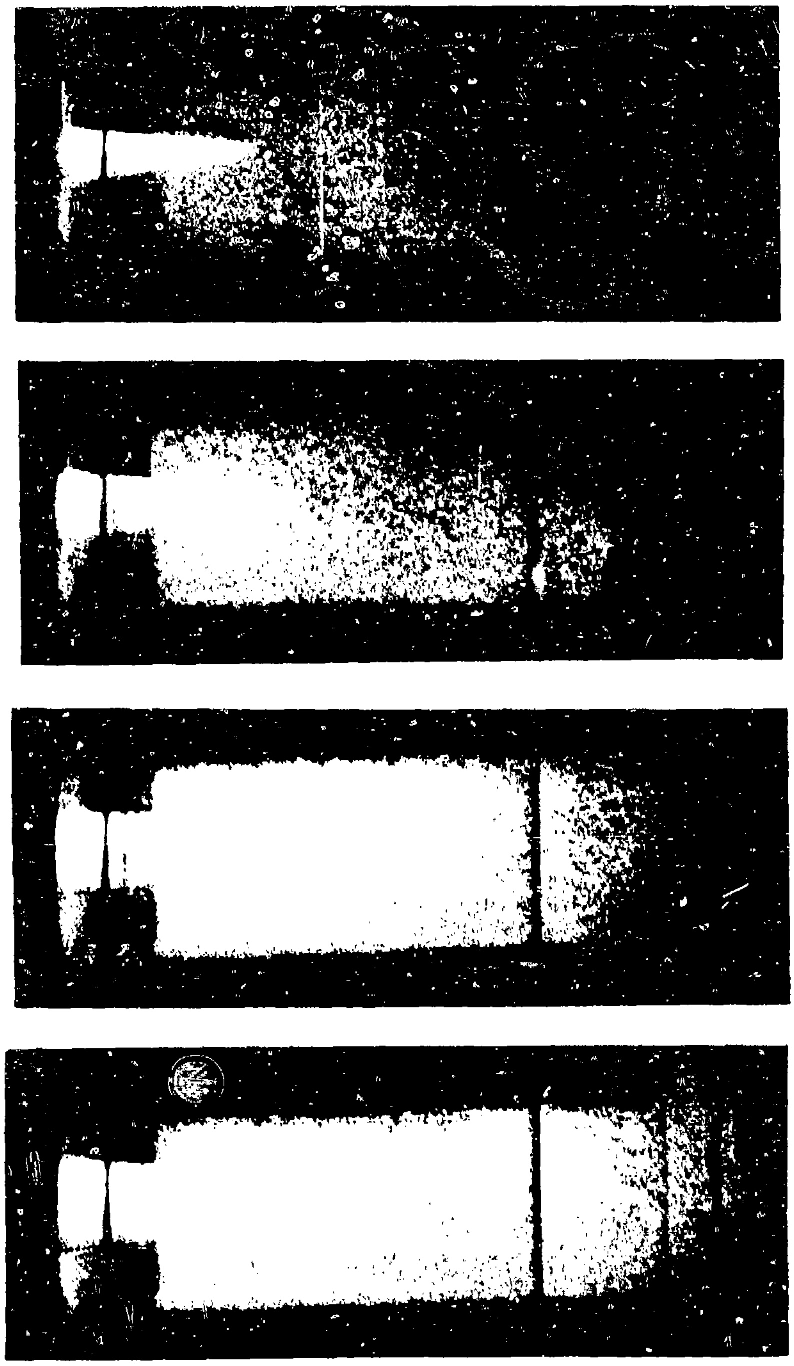

Figure 42. Projectile Entering Tank in Shot FT4. Inside wall of tank is just beyond left side of window. Interframe time is 146 μs.

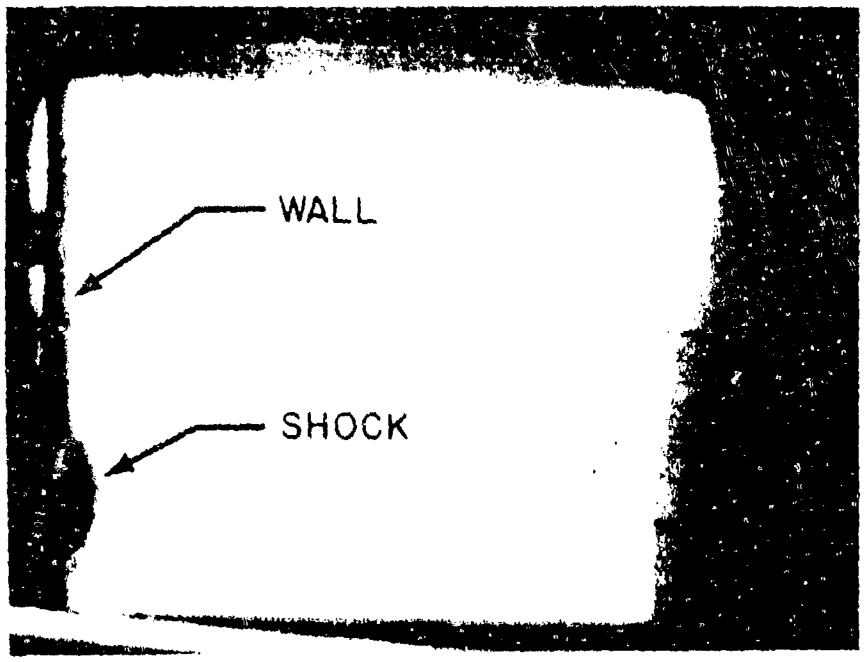

(a) Frame after impact

(b) Portions of three successive frames

Figure 43. Successive Framing Camera Photographs of Projectile Penetrating Fluid in Shot FTA9. Interframe time is 1.69 μs. Magnification is 0.68.

coefficient of drag, C_D, a parameter which was used as input to the fluid drag code.

The coefficient of drag is defined by the relation

$$-m \frac{du}{dt} = \frac{\rho u^2}{2} a\, C_D \qquad (15)$$

where m and u are the projectile mass and velocity, ρ is the density of the fluid, a is the projectile cross-section area and C_D is the coefficient of drag. The drag force on a body is, therefore, proportional to the stagnation pressure and the cross-sectional area of the body normal to the projectile velocity. The coefficient of drag is a constant and in general depends on the Reynolds number and mach number, as shown in Figures 44 through 46. The data in these figures were obtained for projectiles in air.

4.4.1 Projectile Reynolds Numbers

The Reynolds number for a sphere is given by

$$Re = \frac{\rho_f D u}{\mu} \qquad (16)$$

where ρ_f is the fluid density, D is the diameter of the sphere,

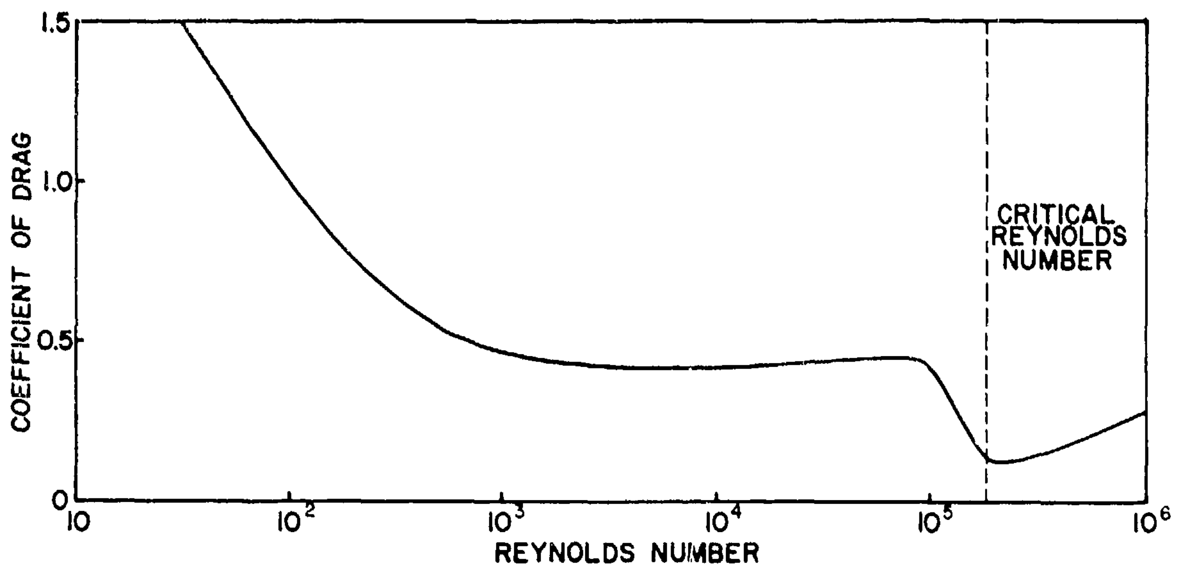

Figure 44. Drag Coefficient vs. Reynolds number for Spheres (Taken from Prandtl[23]).

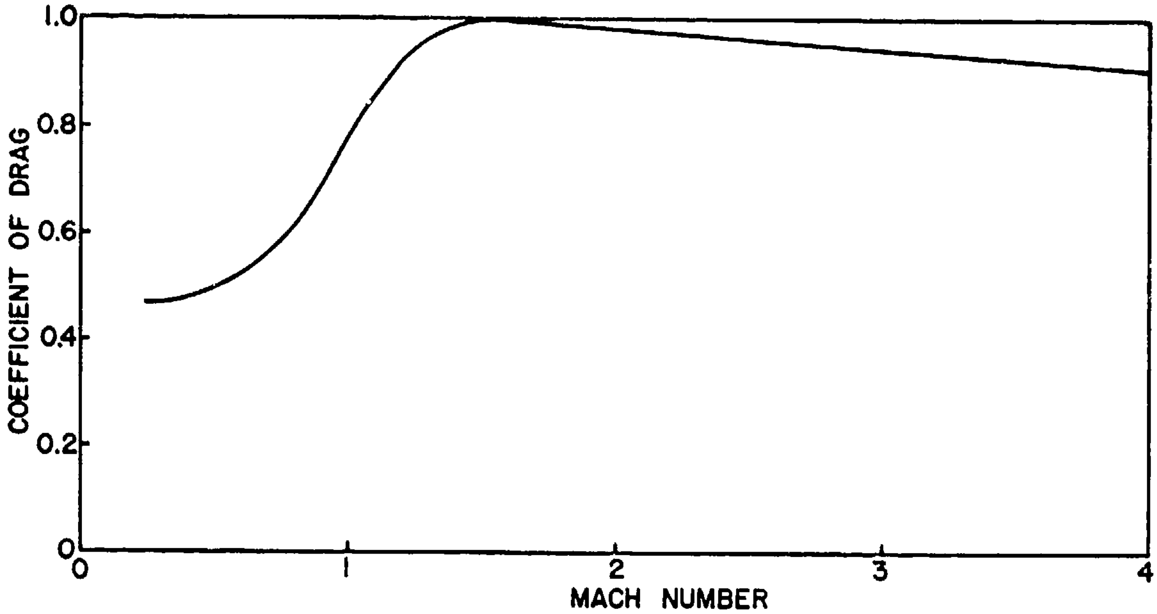

Figure 45. Drag Coefficient vs. mach number for Spheres (Taken from Shapiro[24]).

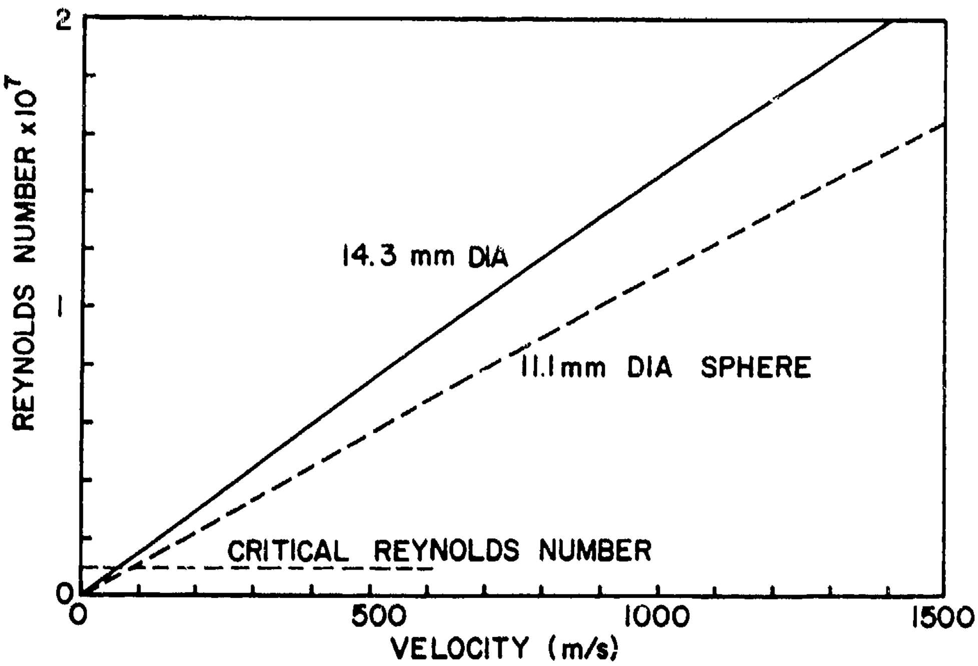

Figure 46. Reynolds Number vs. Velocity for Spheres.

V is the velocity and μ is the fluid viscosity. For water the viscosity is

$$\mu = 10^{-3} \frac{kg}{m \cdot s}$$

and the density is

$$\rho_f = 10^3 \frac{kg}{m^3}$$

The Reynolds numbers for 11.1 and 14.3 mm diameter spheres are plotted in Figure 46.

Comparing Figure 46 to Figures 44 and 45 one sees that the initial drag coefficient of the projectiles (which are slightly supersonic) will be 0.6 to 0.8. By the time a projectile is midway across the large tank (0.5 m travel) its velocity has usually dropped to a little less than half its initial value. Thus, C_D is expected to fall to about 0.4. The drag coefficient will then continue to decrease, unless the velocity falls below about 100 m/s. At that velocity, the critical Reynolds number regime is reached and C_D increases sharply. The observed values of C_D are consistent with these considerations.

4.4.2 Drag Measurements

To determine the coefficient of drag, the projectile position and time data were least-squares fit to the equation

$$x = \frac{\ell n \ (\kappa u_i t+1)}{\kappa} \tag{17}$$

where

$$\kappa = \frac{3 \ \rho_f \ C_D}{8 \ \rho_p \ R_o} \tag{18}$$

and u_i is the initial velocity of the projectile in the fluid. In Equation (18), ρ_f and ρ_p are the fluid and projectile densities, and R is the projectile radius. Equation (17) follows from Equation (15) after two successive integrations.

The value of u_i was determined before the large tank data was curve fit to Equation (17). This determination was based on displacement vs. time information, obtained from the shock tank shots. These measurements provided numerous data points for the first 5 to 10 cm of projectile travel through the fluid. The

projectile velocity was found to be essentially constant from about 10 to 50 μs after impact. Plots of initial velocity vs. the impact velocity are shown in Figure 47. For small spheres, velocity lost during impact was approximately a linear function of the impact velocity given by

$$u_o - u_i = 0.92\ u_o - 1.1 \qquad (19)$$

where u is expressed in km/s. Alternatively, Equation (19) can be written

$$u_i = 1.1 + 0.08\ u_o \qquad (20)$$

Only one large sphere data point was available, so no conclusion could be drawn concerning the behavior of large spheres.

Data were least-squares fit to Equation (17) using a u_i calculated from Equation (20). The resulting drag coefficients were used in the calculations. The range of variation was small, however, ranging from 0.32 to 0.36 and increasing with impact velocity. Figure 48 compares an actual trajectory with the predicted one for a typical case (FT5).

Another important result is evident in Equation (20). For small spheres, the initial velocity of the projectile is relatively insensitive to variations in impact velocity. Thus, the high velocity projectiles surrender increasing amounts of kinetic energy immediately at impact. This energy is absorbed in the strong shocks associated with high velocity projectile impacts.

There is evidence that the C_D has a value of approximately 0.6 in the region within about 15 cm of the entrance panel. Values in this range were computed by CRT using the AFTON code. The shock tank data also imply large values of C_D, but those data are considered unreliable for acceleration measurements due to the "lensing" effect of the shock wave.

4.5 SHOCK VELOCITY MEASUREMENTS

The propagation speeds of impact-induced shock waves in the fluid were measured using the shock tank. Peak pressure can be calculated directly from these data by using the Hugoniot relationship:

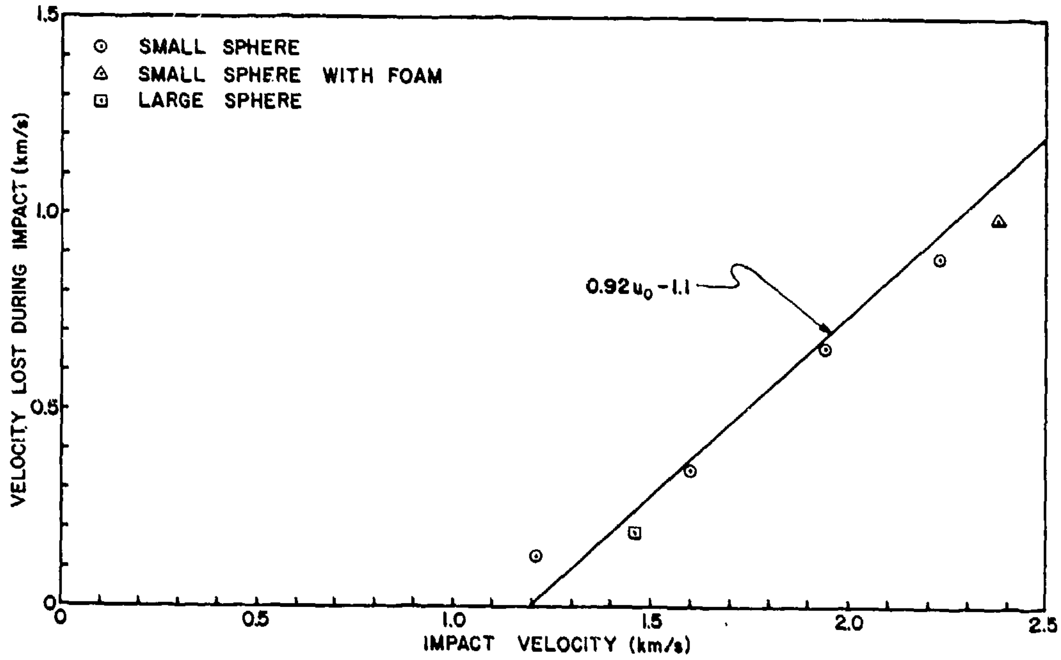

Figure 47. Initial Velocity vs. Impact Velocity for Spherical Projectiles.

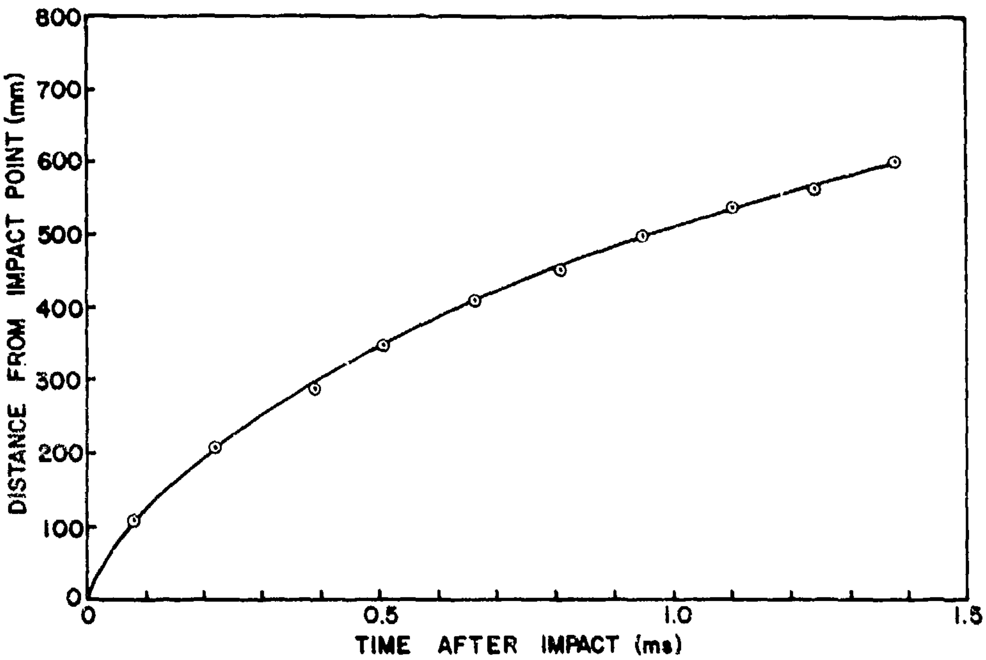

Figure 48. Comparison of Measured Projectile Trajectory and Trajectory Calculated from Best Fit Drag Coefficient for Shot FT5.

$$P = \rho_o \, uU, \tag{21}$$

(where u and U are, respectively, the particle velocity and the shock propagation velocity, measured relative to the material into which the shock is moving) and the known Hugoniot of water[12]

$$U = 1.51 + 1.85\ u \text{ (in km/s)}. \tag{22}$$

Values of peak shock pressure calculated from (21) and (22) and the measured values of U along the trajectory for Shot FTA9 are shown in Figure 49.

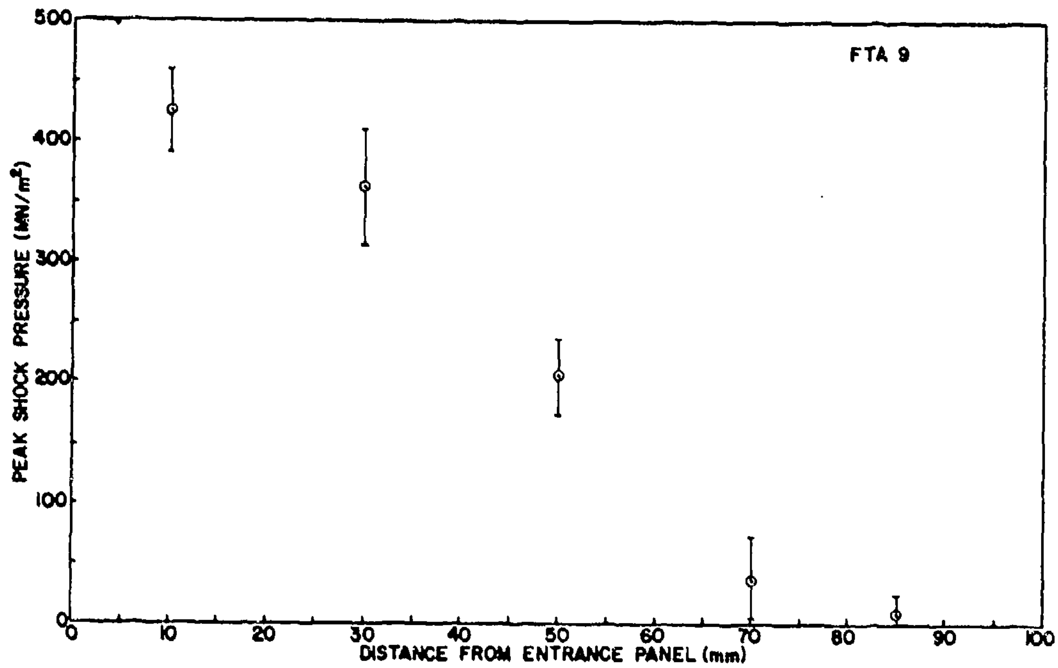

Figure 49. Peak Shock Pressure Calculated from Shock Velocity Data from Shot FTA9.

For present purposes, the shock position-time data were fit to an equation provided by Yurkovitch[7];

$$x = kt^{\psi} \tag{23}$$

where x and t are shock front position and time, and k and ψ are parameters derived from measurements. The properties of Equation (23) and the procedure used for deriving k and ψ are discussed in Section 5.

The effect of pressure relief on the front tank wall can be seen by comparing shock propagation (x, t) data into the fluid with that along the wall. For example, Figure 50 shows (x, t) data from Shot FTA9. The shock propagation velocities in the two propagation directions, at 30 mm in the tank, are 1.87 ±0.04 and 1.54 ±0.07 km/s, respectively. The corresponding pressures are 37.6 and 26.3 MN/m².

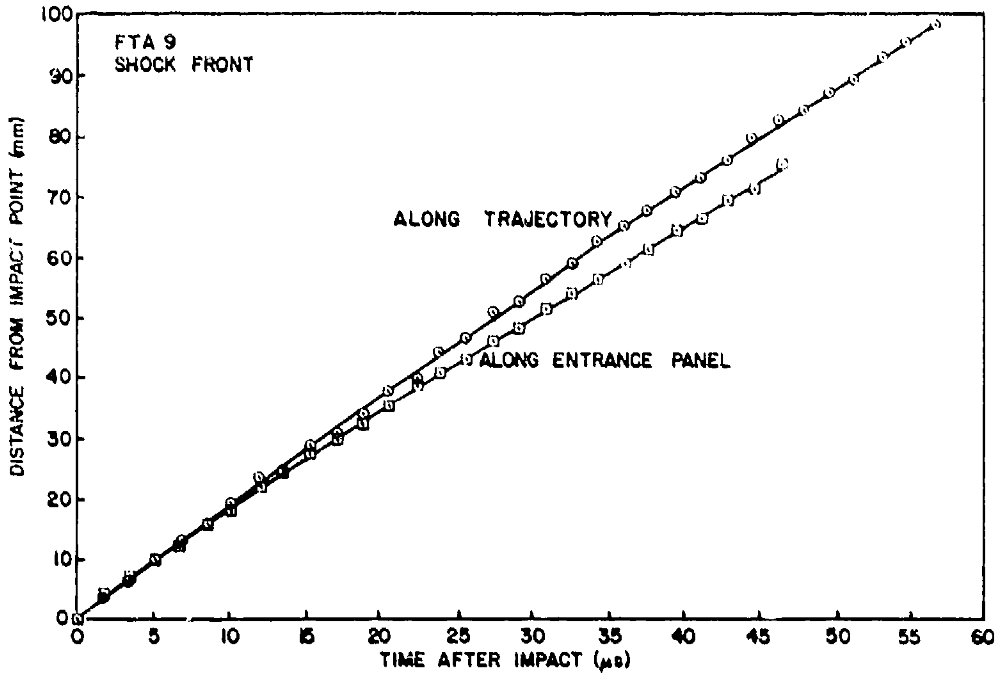

Figure 50. Shock Position vs. Time for Shot FT9.

The degree of pressure relief near the entrance panel is larger for foam-backed panels. In FTA12 (38 mm foam-backed panel) after ∿55 mm travel the shock speeds into the fluid and along the wall are, respectively, 1.78 ± 0.09 and 1.27 ± 0.25 km/s. Corresponding pressures are 21.3 and ∿0 MN/m^2.

4.6 PRESSURE MEASUREMENTS

Pressure transducers were included in most of the shots in order to provide data to check code-generated pressure values. The pressure data were recorded on wide bandwidth oscilloscopes. Time of arrival was usually determined from a fiducial mark superimposed on the data channel.

In many cases the initial pressure spike was off-scale on the oscillograph. In addition, high frequency noise (~100 kHz) from mechanical resonances was superimposed on many data traces. Figure 51 illustrates a typical example, taken from Shot FT31. The transducer was situated near the center of the tank. The initial arrival is off scale, but the trace returns about 30 μs later. There is a pressure plateau of about 1.7 MN/m^2, and the total duration of the pulse is about 150 μs. This transducer underwent a slight zero shift, which occurred in about one-third of the records. At later times there is a 2 kHz oscillation. This also occurred in many records, and is a little too fast to be ascribed to standing pressure waves in the fluid. More likely, it is caused by a resonance in the transducer-support apparatus.

For many records, the high frequency components were removed from the transducer output with 30 kHz cut-off filters. Two typical filtered records are shown in Figure 52. The initial peaks may have been slightly clipped, since their rise times are ∿10 μs. The remainder of the traces are a great deal easier to read than that of Figure 51. From the lower trace of Figure 52, which is from the transducer nearest the rear panel in Shot FT34, it can be seen that the initial pressure spike has an amplitude of ∿6.5 MN/m^2 and a duration of ∿100 μs. The pressure then falls to zero over 300 μs. Of the total impulse contained in the pulse, about half is in the leading

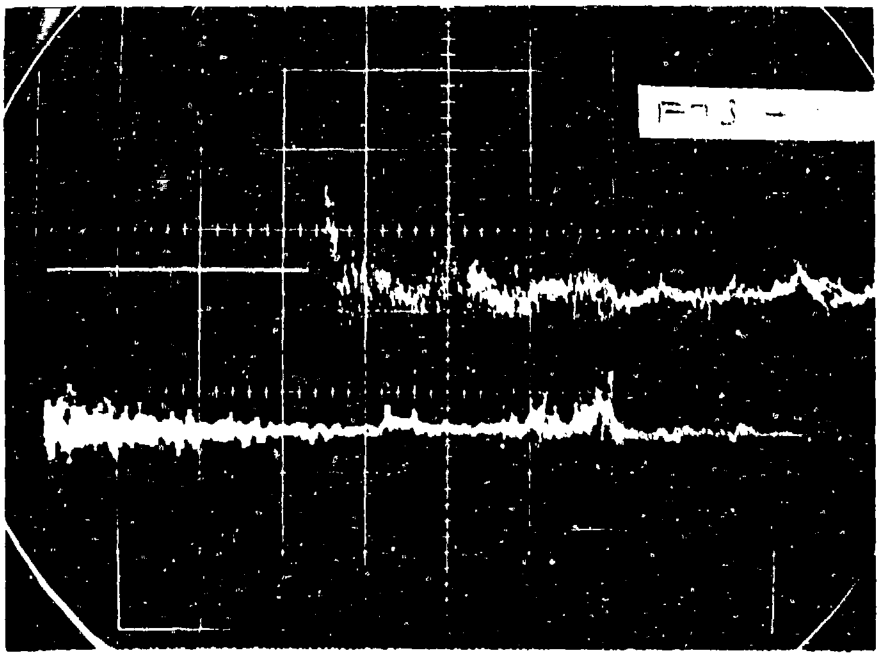

Figure 51. Shot FT31, Transducer T3 (431 mm from Entrance Panel, 100 mm Above Trajectory). Scope is triggered at Impact. 0.49 ms/div sweep rate. 1.4 MN/m^2/div vertical scale.

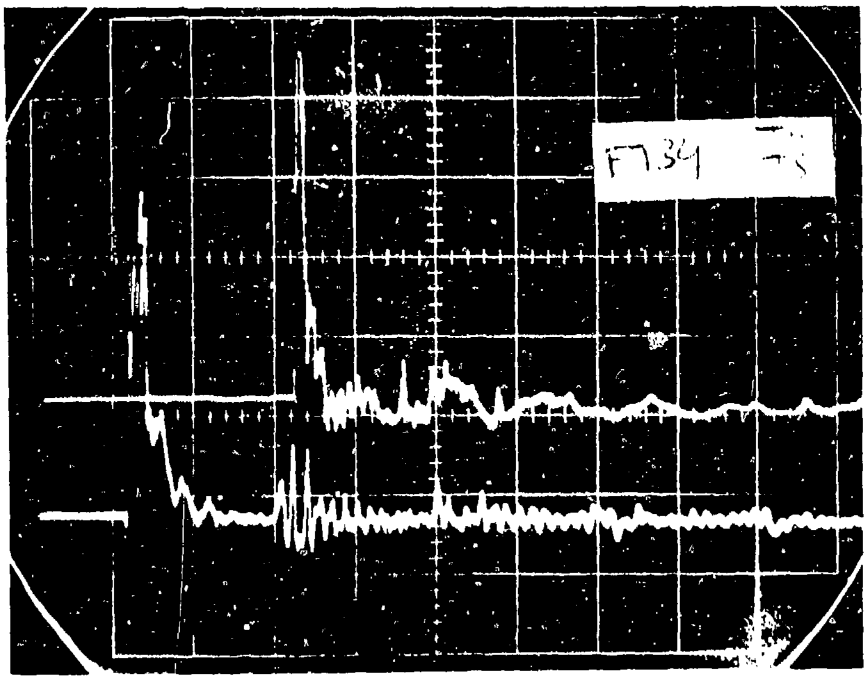

Figure 52. Shot FT34 Upper beam: Transducer T4 (737 mm from Entrance Panel, 180 mm From Trajectory) 1.35 MN/m^2/div Lower Beam: Transducer T5 (983 mm from Entrance Panel, 180 mm From Trajectory), 1.6 MN/m^2/div, 1.5 ms delayed sweep. 0.49 ms/div sweep rate.

spike. This indicates that even deep within the tank, hydrodynamic ram loading is a very rapid event measured in tenths of milliseconds.

Additional discussion of pressure records for individual experiments ca be found in Section V. There the measured pressures are compared with those predicted by numerical techniques.

SECTION V
CALCULATIONS

Two approaches have been taken to computer prediction of fuel tank wall motion. The first approach was based on a finite element computer code, BR-1A, originally developed by Northrop Corporation to calculate tank wall response to an internal blast. This code was modified to account for fluid loading of the tank walls, BR-1A (HR). A principal input is the fluid pressure that would exist at the boundary if the walls were absent. These pressures were generated from two computer routines; the description of the pressures in the fluid due to projectile drag uses a code developed by Lundstrom[14] (fluid drag code) and the pressure profile behind the shock front is a theory developed by Yurkovich[7] (fluid shock code). The loading pressures for the bare panel problem were calculated with the fluid drag code and fluid shock code and input into the BR-1A (HR) code. The finite element code does not have the capability of calculating the response of a wall backed by foam.

The second approach was based on a two-dimensional finite difference code (AFTON) together with a finite element code (WONSAP). AFTON finite difference calculations were used to treat the bare panel case as well as the foam backed panel case.

The threats and impact configurations selected for computer analysis are outlined in Table 2.

5.1 THE FLUID DRAG CODE (FDC)

5.1.1 Description of the Code

The fluid drag code (FDC) is described in Reference 3. It provides a technique for calculating the fluid pressure and velocity as functions of time at specified points within a

TABLE 2. CALCULATION MATRIX

Shot No.	Sphere Size (mm)	Impact Velocity (km/s)	Wall Material (Al)	Foam Thickness (mm)	Panel Considered BR1-A	
					BR1-A	AFTON/ NONSAP
FT5	11.1	1.53	2024-T3	0	Entrance	Entrance
FT26A	11.1	1.52	2024-T3	38	-	Entrance
FT2	11.1	1.73	7075-T6	0	Entrance	-
FT6	14.3	1.52	2024-T3	0	Entrance	Entrance
FT8	14.3	1.57	2024-T3	38	-	Entrance
FT33	14.3	1.83	7075-T6	0	Side	-

tank penetrated by a tumbling projectile. The code is very efficient and uses only seconds of computer time. The calculated pressures are sufficiently accurate for most purposes as long as certain assumptions made in the code are not violated. These assumptions are:

1. The projectile is subsonic.
2. The cavity does not influence the pressure field.
3. Boundaries of the fluid are either perfectly rigid, free, or perfectly transmitting.
4. The fluid volume is a rectangular solid.
5. The projectile drag coefficient is independent of projectile velocity (provision is made for changing drag coefficient due to projectile tumbling and case stripping, but these were not used for this work).

In previous work[3] this code was used to calculate the

pressure induced by tumbling armor piercing (AP) projectiles. The side panels of the tank were so far from the trajectory that their influence could usually be ignored. Bullet tumbling and jacket stripping in the fluid could not be measured very accurately; however, transducers recorded fluid pressure at typically five positions in the tank. Using the pressure data, the nine parameters in the FDC which pertain to bullet tumbling and stripping were varied to bring the computed pressures into agreement with the measured pressures. These parameter values could then be used to compute pressure elsewhere in the target tank.

In the present application, no tumbling or stripping of the projectile occurs, and the values of all input parameters were uniquely determined from measurements. The value of the drag coefficient (C_D) and the initial projectile velocity (u_i) were determined from the experimental data, as discussed in Section 4.4.

The coordinate system defined for the FDC consisted of an origin at the lower right hand corner of the entrance panel; + x pointed across the tank, + y was up, and + z was into the tank.

The volume occupied by fluid was $0<x<x_c$, $0<y<y_c$, and $0<z<z_c$, where x_c, y_c, and z_c were 0.850, 0.798, and 0.980 m, respectively.

Two minor modifications were made to the FDC. First, the IMAGES subroutine was modified to allow boundary conditions pertinent to the UDRI test tank. Pressure reflections from tank boundaries are accounted for by up to 27 images of the projectile moving in an infinite fluid. In the original version of the code, all images were of the same type, depending on whether the boundaries were rigid (+1 image), free (-1 image) or transmitting (0 image). In the present version, the values of the ASIGN matrix are altered to describe a tank with rigid boundaries at x = 0, and at y = 0, free surfaces at $x = x_c$, $y = y_c$, and $z = z_c$, and a transmitting boundary at z = 0.

The other modification necessary to the code was a provision to calculate and print the input data in the format required for the BR-1A (HR) code. The required input data are just twice the pressures as calculated by the FDC on the z = 0 plane. It was determined that the code could not calculate pressure at z = 0, so the entrance panel pressures were calculated for z = 0.5 mm. The code modifications were inserted into the MIRROR subroutine to calculate pressure and into the HRAM subroutine to write data. The modification made to the FDC, as well as sample input data, are listed in Appendix B.

5.1.2 Validation of Pressure Predicted by the FDC

Validation of the FDC was accomplished by comparing pressures predicted by the code with pressures measured by transducers or predicted by the AFTON code. In assessing the code, no input parameters were altered to improve agreement with the measured pressure profiles.

The best pressure transducer data were obtained from stations in the rear half of the target tank. For Shot FT33, the computed and measured pressure pulses for the T4 transducer are compared in Figure 53. The transducer was situated 740 mm from the entrance panel and 100 mm above trajectory. The oscilloscope record was filtered with a 30 kHz (30 μs rise time) cut-off filter. Thus, the pulse rise time may have been lengthened and reduced slightly. The record shown in the figure has been smoothed by hand to eliminate pulses shorter than ∿20 μs duration. Negative values of FDC predicted pressure are plotted as zero.

The agreement of the two pressure profiles is very satisfactory. The arrival time of the predicted pulse agreed with that of the measured pulse better than the estimated measurement error (±10 μs). Both pulses indicate that the peak pressure is attained within ∿25 μs after first arrival, and after the peak the pressure decays rapidly. After about 50 μs the decay becomes less rapid. Over two-thirds of the total impulse is contained in the more slowly decaying regime, which lasts for about 150 μs. The impulse delivered by the two pulses agree within the measurement accuracy (±15%).

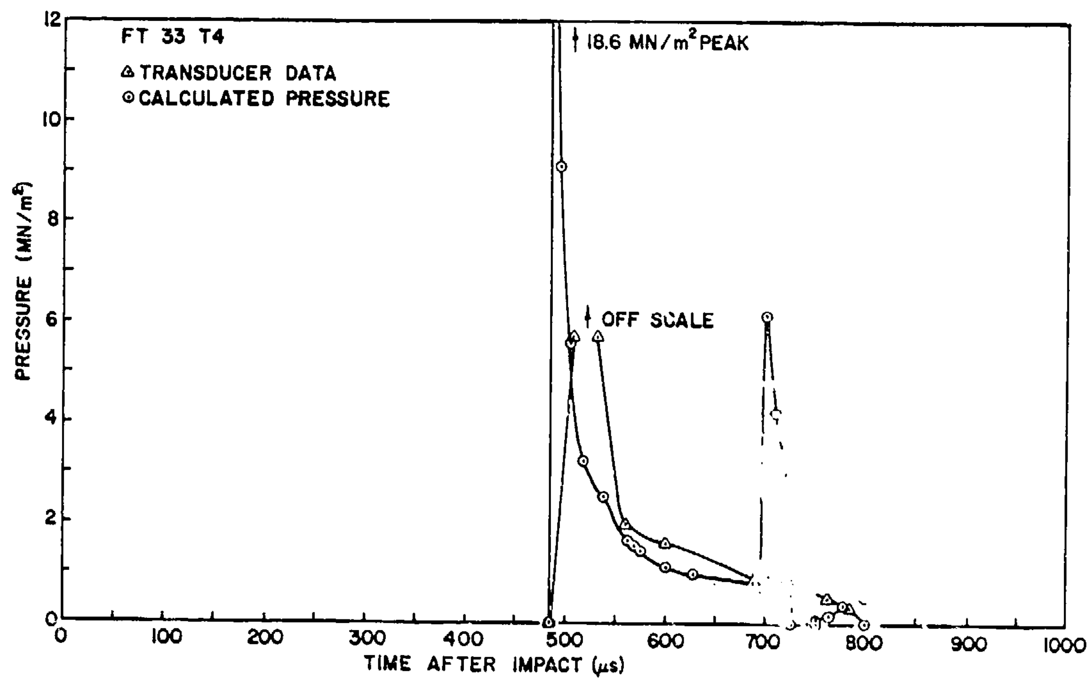

Figure 53. Comparison of pressure computed by FDC and pressure measured by a transducer in Shot FT33 at a point located at 100 mm above trajectory 740 mm from the entrance panel.

A spike which occurs at 700 μs in the FDC calculation is nearly absent in the transducer record. Inspection of the calculated fluid velocity components reveals that the spike is due to a reflection from the bottom of the tank, which was modeled as a rigid boundary. In the FDC, the reflection propagated through the cavity to arrive at the transducer station. In the actual experiment, of course, the cavity does not propagate waves. Fortunately, late time arrivals such as these carry little impulse and are not of great concern in assessing the usefulness of the FDC. The effect of similar cavity-related errors in the FDC treatment will be even smaller at the panels.

A similar comparison of pressure profiles for the T3 transducer in Shot FT33 (at z = 430 mm, 100 mm above trajectory) is shown in Figure 54. Consideration of the indicated zero shift in the transducer data brings the two profiles into good

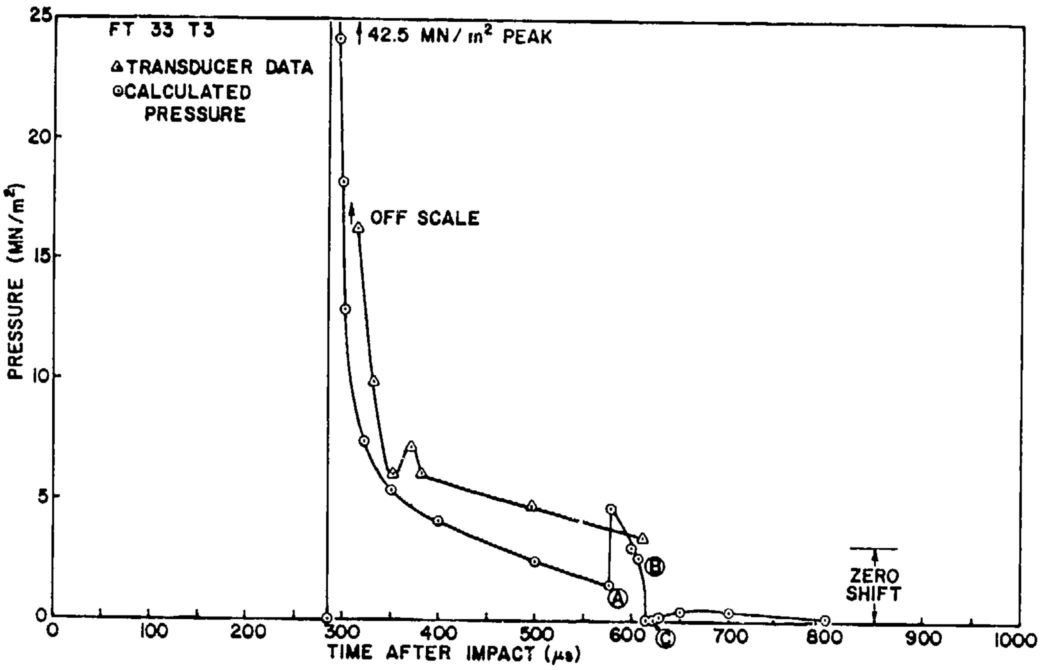

Figure 54. Same as Figure 53, except for a point 0.43 m behind the entrance panel.

agreement. The same general features noted previously apply here, too. On the computed profile, points A, B, and C mark, respectively, the arrival of reflections from the bottom surface, the free (top) surface, and the side surfaces. (Contrary to the appearance of the figure, it can be seen from examination of the printouts that the arrival from the sides had no effect on pressure and dP/dt did not change).

Figure 55 illustrates the agreement between the FDC and pressure data for the transducer placed nearest the entrance panel. The data from the T1 station (z = 133 mm, 220 mm above trajectory) in Shot FT5 are used. Again, arrival times agree extremely well. When the transducer record comes back on scale, it is in satisfactory agreement with the FDC pressure. The agreement is improved if the measured spikes at 230 and 290 μs are regarded as instrument noise. This is probably the case, since they appear on almost all T1 transducer traces. The accuracy of the FDC near the entrance panel can be assessed by comparison with the results of the AFTON calculations.

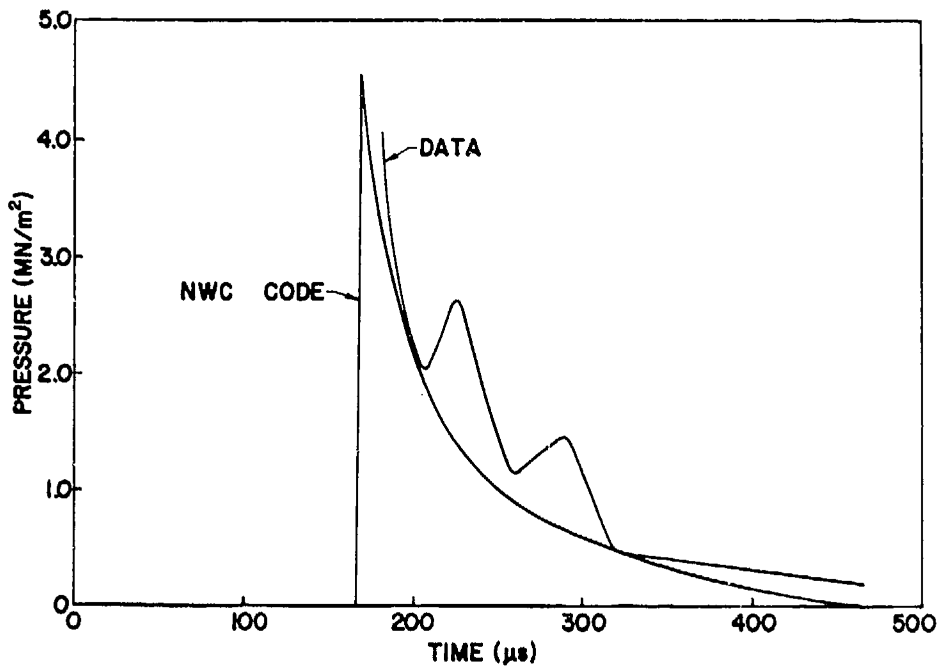

Figure 55. Same as Figure 52, but for a point 220 mm above trajectory and 133 mm behind entrance panel.

Figures 56 and 57 document two such comparisons within 100 mm of the panel. The FDC does not model shock wave formation, and hence fails to reproduce the leading peak on the AFTON profiles. The AFTON pressure is overall slightly higher because in the AFTON model of the FT5 event the projectile enters the fluid at 1.55 km/s, whereas in the FDC model, it enters at 1.24 km/s. The general agreement between these two totally different numerical treatments implies that both successfully model the effects of drag forces in the fluid.

5.1.3 Results of Calculations With FDC

The FDC was very helpful for obtaining a qualitative understanding of several phenomena in the target tanks. For example, most transducer records showed an abrupt drop to zero pressure about 200 μs after first arrival. This was shown to be due to the reflection of a pressure wave from the free surface. It was also shown that in general $P \gg \rho_0 U^2$ in the flow, so that the orientation of a transducer will not effect its

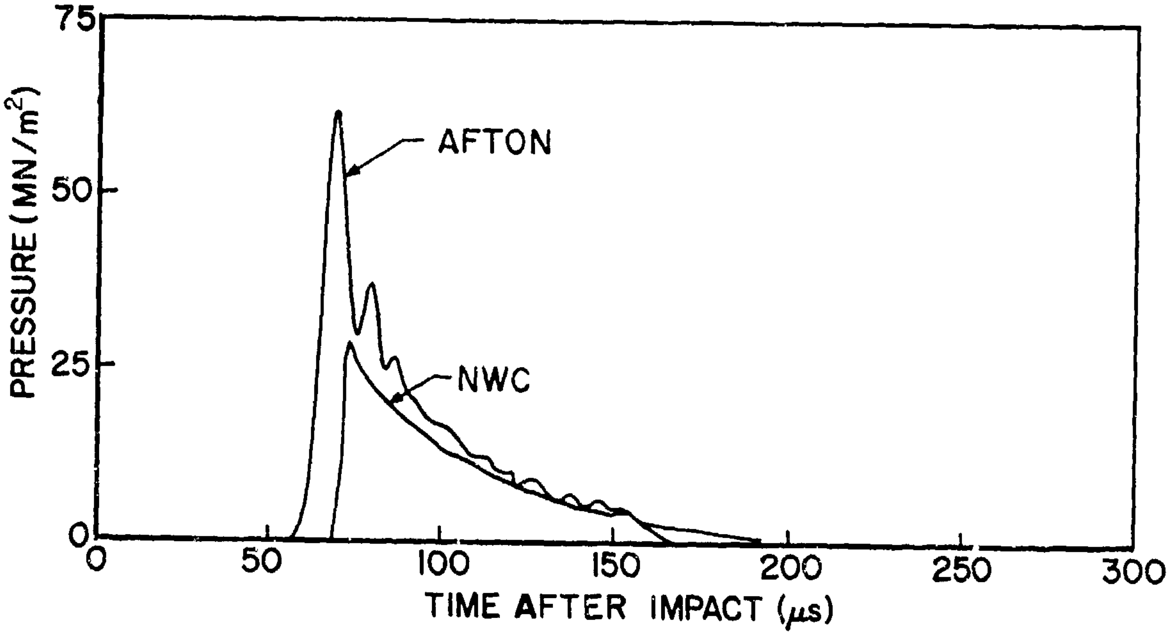

Figure 56. Comparison of pressure profiles predicted by FDC and AFTON for a point 100 mm behind the entrance panel and 100 mm off trajectory.

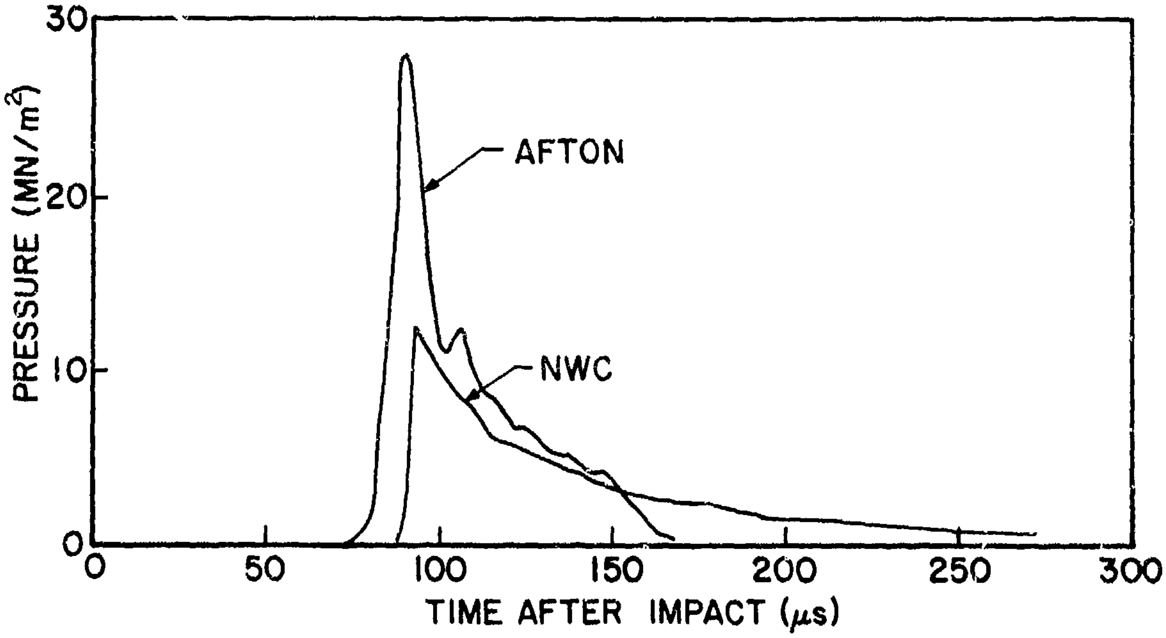

Figure 57. Same as Figure 56, but for a point 50 mm behind entrance panel.

reading. This was confirmed experimentally.

Lundstrom suggested[3] that negative values of calculated pressure be set equal to zero for computational purposes. This was done for the input to the BR-1A (HR) calculations. Lundstrom has suggested[20] that, at least near the trajectory, negative values of pressure may signify cavitation. In Figure 58, the observed cavity at z = 133 mm is compared with regions of (y, t) space in which the Lundstrom code predicts negative pressures.

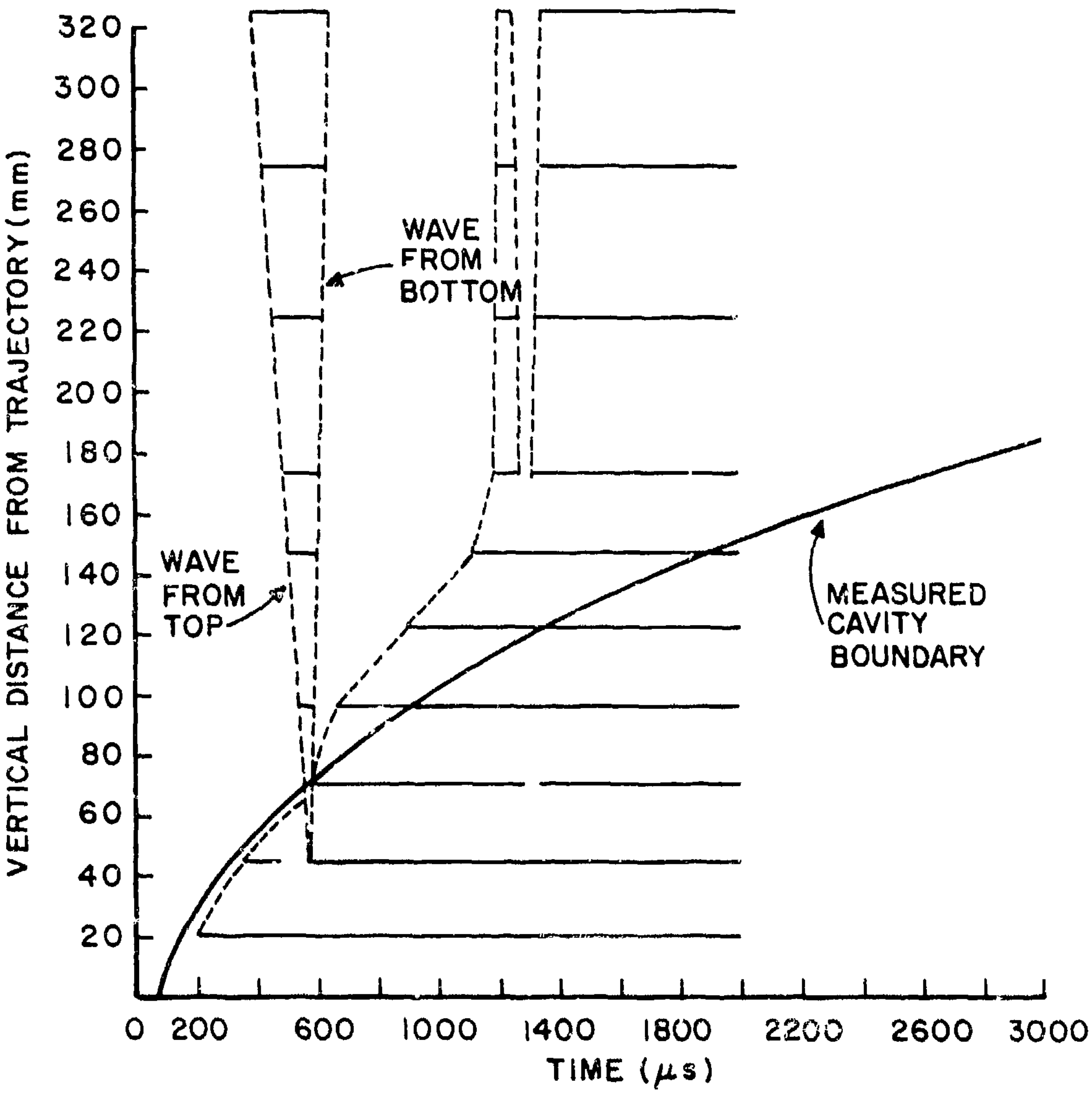

Figure 58. Comparison of experimental and predicted cavitation at z = 133 mm for Shot FT5. (Horizontal lines show region in which calculated pressure is less than zero).

The initial agreement with the projectile cavity is rather good. However, the code also predicts a cavitation wave from the upper free surface which was not observed within the space visible to the trajectory-viewing framing camera.

Figures 59 and 60 show examples at front panel pressures calculated for FT5 and FT5B. It can be seen that in the central regions of the tank, peak pressures are approximately 7 MN/m^2 (1000 psi) but drop by a factor of 10 in about 300 μs.

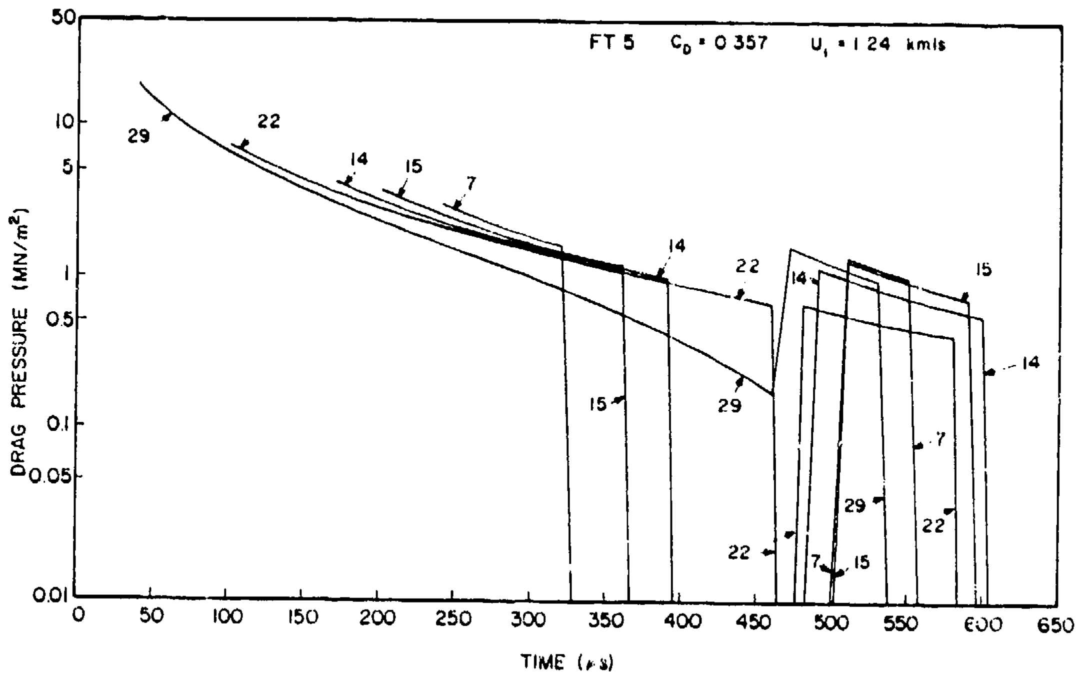

Figure 59. Pressure-time history predicted at selected points on trajectory for impact conditions of Shot FT5. The numbers identify pressure-history points. The coordinates of the pressure-history points can be found from Figure 64.

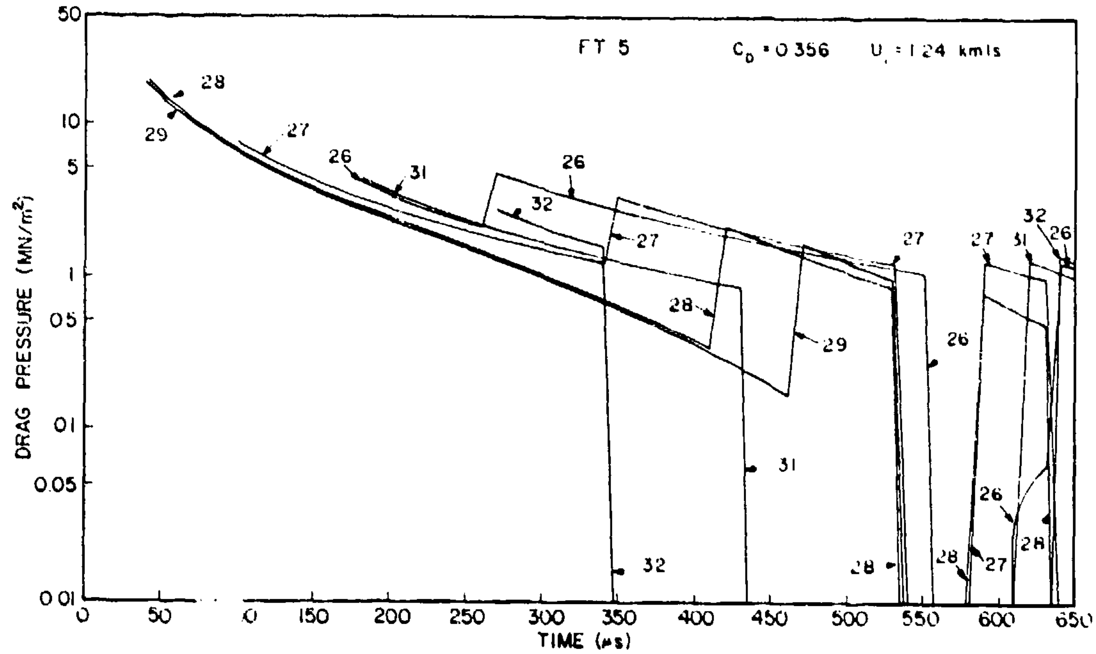

Figure 60. Pressure-time history for selected points above and below trajectory for impact conditions of Shot FT5. The coordinates of the pressure history points are given in Figure 64.

5.2 THE FLUID SHOCK CODE

The shock pressure in a hydrodynamic ram event loads a small portion of the entrance panel impulsively during the first 100 μs after impact. Pressure profiles behind a shock front are extremely difficult to measure, but using the theory described by Yurkovich[7], they can be calculated from measurements of the shock front velocity. His treatment uses a nondimensional form for the continuity equations and the equations of state, and is based upon the work of Bach and Lee[16]. For this study, only the portion of Yurkovich's work which treated the pressure behind a shock front is described.

The conservation equations and the equation of state are written in nondimensional form. The following definitions are needed;

$$\text{Shock Mach Number;} \quad M = \frac{U_{s_o}(t)}{c}$$

$$\text{Position;} \quad \bar{r} = \frac{r}{r_{s_o}(t)}$$

$$\text{Velocity;} \quad \bar{U}(\bar{r}, M_{s_o}) = \frac{U(r,t)}{U_{s_o}(t)}$$

$$\text{Density;} \quad \bar{\rho}(\bar{r}, M_{s_o}) = \frac{\rho(r,t)}{\rho_o} \tag{24}$$

$$\text{Pressure;} \quad \bar{P}(\bar{r}, M_{s_o}) = \frac{P(r,t)}{\rho_o U_{s_o}^{\,2}(t)}$$

In the above equations, subscript s_o, indicates quantities along the axis of symmetry, c is the sound velocity (1495 m/s in water) and a bar designates a non-dimensional quantity. Using these definitions, a profile of the pressure behind the shock front can be described. The equation for the pressure requires the non-dimensional density immediately behind the shock front, $\bar{\rho}_1$. To evaluate this quantity, a non-dimensional form of the adiabatic equation of state is combined with the Hugoniot relations to give:

$$M_{s_o}^2 = \frac{1}{n} \frac{\bar{\rho}_1^{\,n+1} - \bar{\rho}_1}{\bar{\rho}_1 - 1} \tag{25}$$

when n for water is 7.0 and total symmetry was assumed. The general equation for the pressure at any point behind the shock is then given by

$$P = P_1 + \left(\frac{\bar{\rho}_1}{q+2} P_2 \right) \left(1 - \bar{r}^{\;q+2} \right)$$

$$- \frac{\bar{\rho}_1}{(q+2)^2} \bar{P}_3 \left\{ 1 + \bar{r}^{\;q+2} \left[(q+2)(\ell n \bar{r}) - 1 \right] \right\} \tag{26}$$

$$+ \frac{\bar{\rho}_1}{(q+2)^3} \bar{P}_4 \left(2 - \bar{r}^{\;q+2} \left\{ \left[(q+2)(\ell n \bar{r}) - 1 \right]^2 + 1 \right\} \right)$$

The non-dimensional pressure terms for Equation (25) are given by:

$$\bar{P}_1 = 1 - \frac{1}{\bar{\rho}_1} \tag{27}$$

$$\bar{P}_2 = \bar{u}_1 (\bar{u}_1 - 1)(1-H) + \beta \left(\bar{u}_1 + M_{s_o} \frac{\partial \bar{u}_1}{\partial M_{s_o}} \right), \tag{28}$$

$$\bar{P}_3 = \bar{u}_1 H \left[1 + \bar{u}_1 (H-2) - \beta \right] - \beta M_{s_o} \frac{\partial}{\partial M_{s_o}} (\bar{u}_1 H), \tag{29}$$

$$\bar{P}_4 = \bar{u}_1^2 H^2, \tag{30}$$

where;

$$\beta = \frac{r_s \mathring{u}_s}{u_s^{\,2}} \tag{31}$$

and

$$H = \frac{\beta M_s}{\bar{u}_1} \frac{\partial}{\partial M_s} \ell n \, \bar{\rho}_1 \, . \tag{32}$$

For the case of a strong shock, the general form of the equation

can be simplified to:

$$\bar{P} = \bar{P}_1 + \frac{\bar{u}_1 \ \bar{\rho}_1}{q+2} (1-\bar{r}^{q+2}) \ (\bar{u}_1 + \beta - 1). \tag{33}$$

Yurkovich made the assumption that the shock would be strong. The simplified initial conditions led to the equation

$$\bar{P} = \bar{P}_1 + \frac{\bar{u}_1 \ \bar{\rho}_1}{q+2} (1 - \bar{r}^{q+2}) \ (\bar{u}_1 + \beta - 1)$$
$$+ (1-\bar{r}^{q+2}) \frac{\beta M_s}{(\rho_1)(q+2)} \frac{\partial}{\partial M_s} \ \bar{\rho}_1 \ . \tag{34}$$

The calculation of the pressures from the above equations is dependent upon the measurement of the shock front Mach number M_s, and the determination of the parameter β.

For this work, β was found by using Equation (31) and assuming that the shock front position as a function of time is described by

$$r_s = kt^{\psi} \tag{35}$$

Yurkovich selected the form of Equation (34) for convenience and because it described the shock waves produced by hypervelocity impact in previous experiments. Yurkovich used $\psi = 0.8$ as descriptive of water. The data for Shot FTA4 are fit by Equation (35) with the parameters $k = 2.54$ mm and $\psi = 0.901$ (for t in μs) or

$$r_s = 2.54t^{0.901} \tag{36}$$

A computer routine to perform the shock pressure calculations was written and is listed in Appendix B. The results of three methods of calculating the pressure are illustrated in Figure 61. The non-dimensional pressures are plotted as a

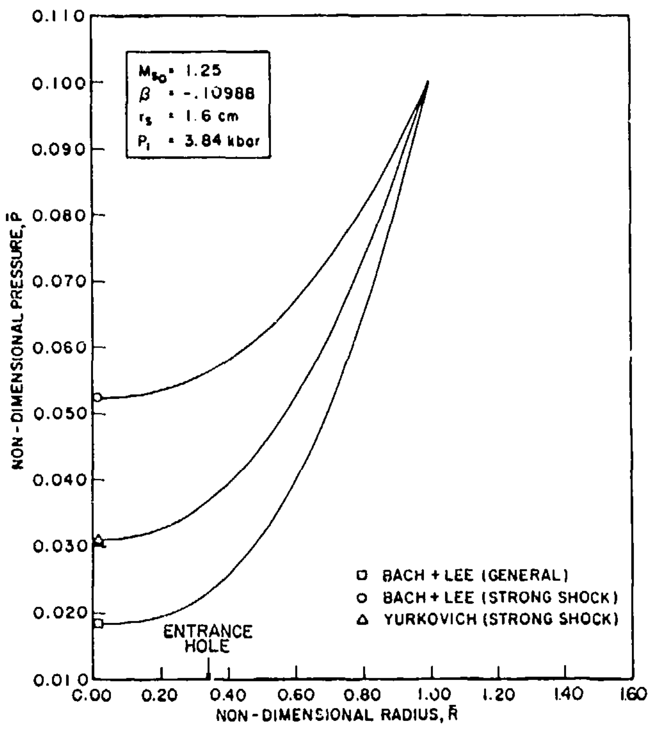

Figure 61. Typical pressure profile calculated by three methods.

function of the non-dimensional radius of the shock front. For the illustrated pressures, the shock front Mach number was 1.25 and the parameter β was -0.10988. From Equation (35), this corresponds to a shock radius of 16 mm at a time of 7.74 μs after impact.

The three pressure solutions converged at the shock front to 384 MN/m^2 (55.7 ksi). Near r = 0 the computed pressure significantly different for the three methods. However, it should be noted that the entrance hole extends from r = 0 to 0.347. No pressure can be exerted on a wall over this region. None of the three methods for calculating the pressures on the wall near the entrance hole takes into account the penetrating projectile.

The Yurkovich pressure equation (Equation (34)) was used to generate the impulse delivered to an element of the entrance panel immediately after penetration. The scheme for calculating the impulse is shown in Figure 62. The force on each region is

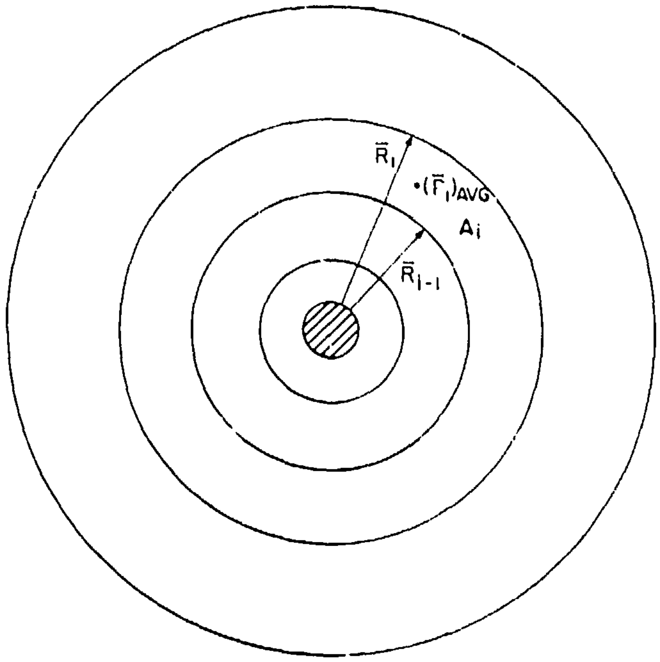

Figure 62. Scheme used in calculating the impulse delivered by the shock pressures to the entrance panel. No forces are applied to the entrance hole (shaded area). Forces on the remainder of the region are calculated from pressure averages.

computed as the average pressure $(P_i + P_{i-1})/2$ times the area of the region A_i. The area is given by

$$A_i = \pi(\bar{R}_i^{\ 2} - \bar{R}_{i-1}^{\ 2}) \tag{37}$$

and the force on the i^{th} region is given by

$$F_i = \rho_o u_s^{\ 2} \bar{P}_i A_i \tag{38}$$

The average pressure for the i^{th} section is read from pressure profile plots similar to those shown in Figure 61. Total forces were calculated at several different times after impact. The forces after impact for Shots FTA4 and FT5B are shown in Figure 63. The forces were integrated to obtain impulse values which were input into the BR-1A (HR) structure code.

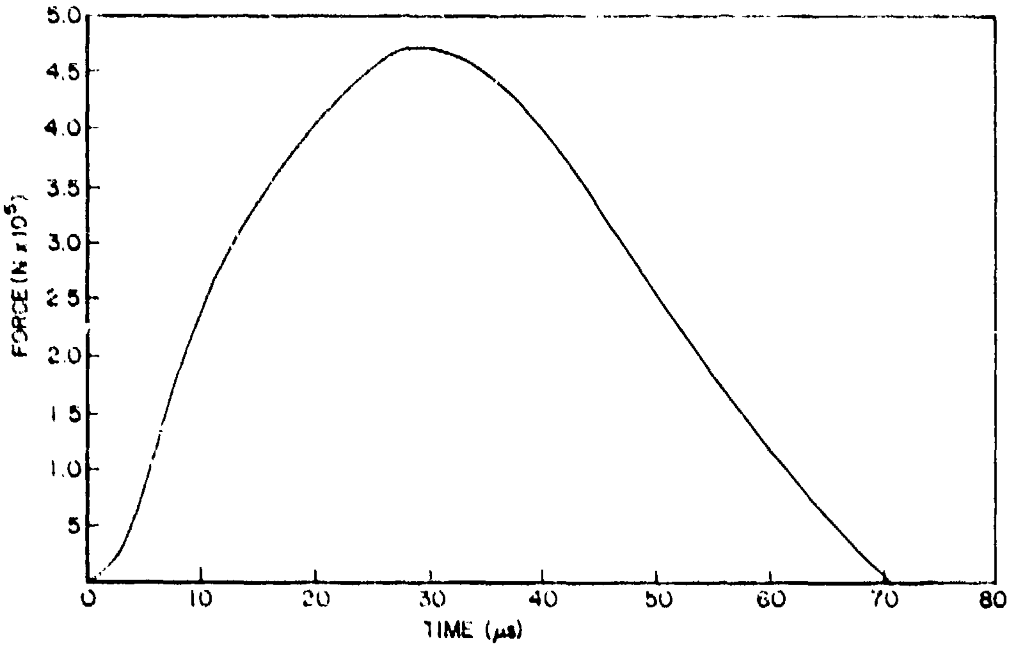

Figure 63. Plot of force vs. time for pressure calculated at entrance panel for Shot FT5B. Impulse was calculated from this plot numerically.

5.3 BR-1A (HR) STRUCTURAL RESPONSE CODE

Deflection of bare entrance and side panels was numerically computed using the BR-1A (HR) structural response code. The basic code, BR-1A, was developed by Northrop Corporation[15] to model blast loading of aircraft structures. For application to hydrodynamic ram problems, the code was modified (HR) at the Naval Post Graduate School[16].

Considerable effort was expended in developing a correct version of the BR-1A (HR) code. The original (HR) modifications were made on an IBM 360 version of the BR-1 code. After these modifications were made to the BR-1A code and a sample problem executed on the CDC 6600, the results did not agree with those of Reference 16. An error in the CDC 6600 BR-1A code was finally uncovered. The statement labeled 3431 in the XFORCE routine should read 3431 JJ = JJ + 2.

The HR modification to the code were based on one-

dimensional piston theory which calculates the pressure on a piston as

$$P = P_i + \rho c \, (u_f - \dot{w}) \; , \tag{39}$$

where p is the net pressure on a boundary wall, p_i is the incident fluid pressure (e.g., the pressure as if the wall did not affect the fluid), u is the incident fluid velocity normal to the wall, and $\dot{w}$ is the wall velocity.

The assumption that $P_i = \rho cu$ leads to

$$P = 2P_i - \rho c\dot{w}, \tag{40}$$

or

$$P = \rho c \; (2u_f - \dot{w}) . \tag{41}$$

The physical basis of these forms of piston theory is discussed in Reference 22. All are exact for planar incident waves at normal incidence. Equation (40) is exact for an arbitrary incident wave on a plane rigid wall, and Equation (41) is exact for an arbitrary incident wave on a plane free surface.

For nearly-free surface boundary conditions Equation (40 should give better solutions than Equation (39). Thin aluminum walls are expected to behave more like free surfaces at early times and like rigid boundaries as membrane strains develop. On the other hand, in the motions which are considered in this report, it turns out that $P_i \gg \rho c u_f$. Thus, the use of Equation (40) will lead to greater driving stresses than the use of Equation (41). Since, in general, use of the BR-1A (HR) code leads to underprediction of displacement, we have used the form of piston theory of Equation (40) throughout. This same procedure was used in Reference 9 for the same reason. With this form of piston theory, the input required for the BR-1A (HR) is twice the incident pressure P_i, which would be present if there were no fluid-wall coupling. This pressure was provided by the FDC and fluid shock programs described in the preceding sections.

5.3.1 Calculations of Entrance Panel Motion

The elements used to model one-half of the front face of the tank are shown in Figure 64. Circled numbers designate the plate elements and the uncircled numbers designate the joints. The projectile impact occurs at joint 32. The line between joints 29 and 36 is a line of symmetry. The bottom and top edges of the tank are assumed simply supported; however, the slant side is not as easily modeled. The allowable constraints provided by the code are in the global coordinate system, and it is desirable to let the slant edge rotate about a line parallel to the edge. This was done by allowing side joints to rotate about both the x and y axes.

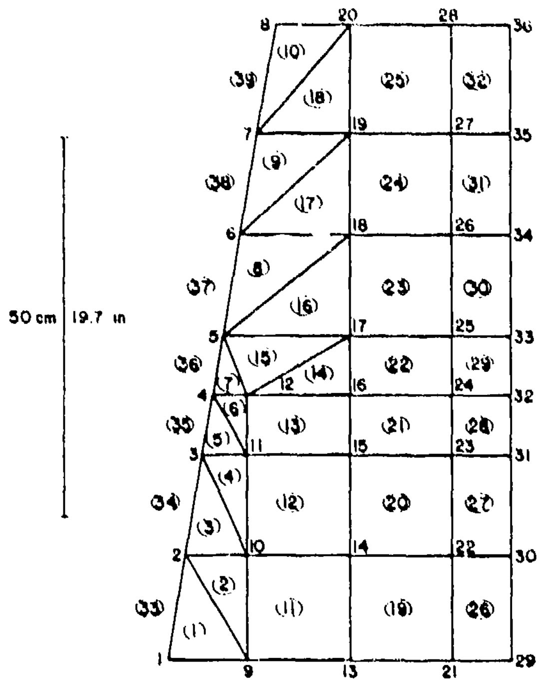

Figure 64. Finite element model of left side of a fuel tank entrance panel. Impact occurs at joint 32. The right side of the tank wall is treated as symmetric.

One very important shortcoming of the program is its inability to handle the initial static deflection due to the hydrodynamic pressure in the tank. It was initially thought that this could be done by applying the hydrostatic pressure as a step function, running the problem to equilibrium and then applying the shock and drag pressures. However, due to the small time step required by the program for numerical stability, this was not possible without an unacceptible use of computer time. An initial attempt at this problem using 100 time steps (total time of 0.0014 seconds) required 570 seconds of CP time and over an hour of IO time on the CDC 6600. A run to equilibrium might take ten times this long. The efficient solution of this problem would require modification of the program to provide a solution to the initial static problem.

An additional weakness in the program is the necessity of providing input pressures which are constant over an element. This makes modeling of the initial impact and early drag forces rather arbitrary since the pressure gradients are very large. This problem could be ameliorated but not eliminated by using smaller elements.

5.3.1.1 Case of 11.1 mm Diameter Projectile Striking 2024-T3 Entrance Panel at 1.5 km/s

This case corresponded to experiments, FT5, FT5A, FT5B, and FTA4 and was also calculated with the AFTON/NONSAP codes (see Appendix A). Samples of the pressures calculated with the FDC and input into the BR1-A (HR) code are given in Figures 65 and 66. The running time was typical, 431 s CP and 1993 s IO.

It is apparent that the discrepancy between predicted and observed panel displacement is very severe. In the calculation, the peak displacement is reached in about 600 μs, and is 15 percent of the eventual peak displacement observed for that experiment. The calculation also fails to show the relatively sharp increase in displacement which propagates away from the impact point. Thus, the computed panel displacement profile is neither in qualitative nor quantitative agreement with observation.

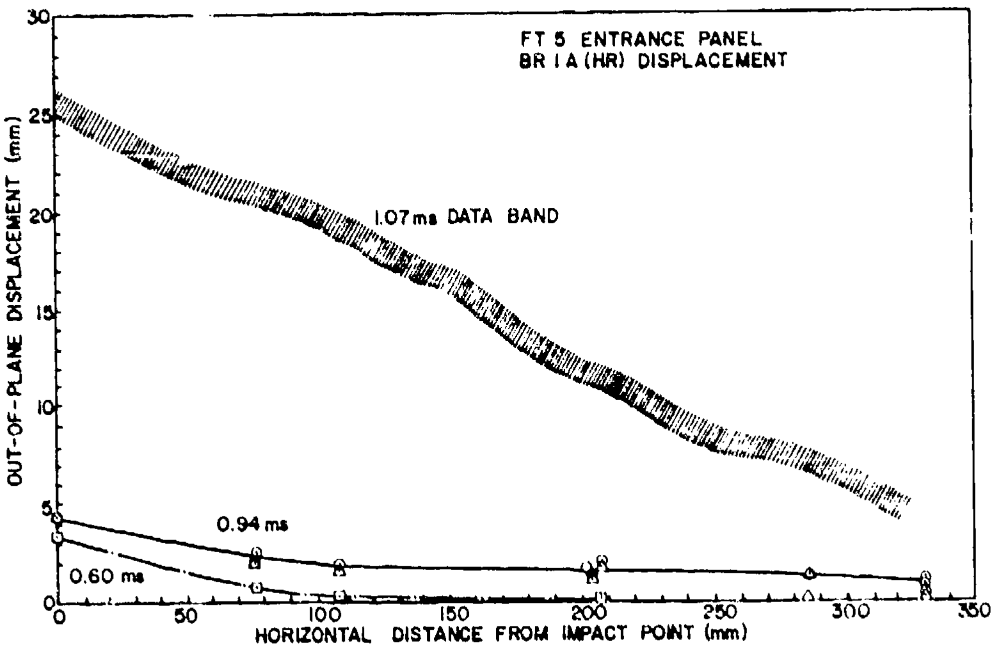

Figure 65. Comparison of panel profiles predicted by BR-1A (HR) code and measured during Shot FT5B. Impact condition is 11.1 mm diameter sphere striking 1.5 mm thick 2024-T3 aluminum panel at 1.5 km/s. BR-1A (HR) was driven by pressures calculated with FDC and shock code.

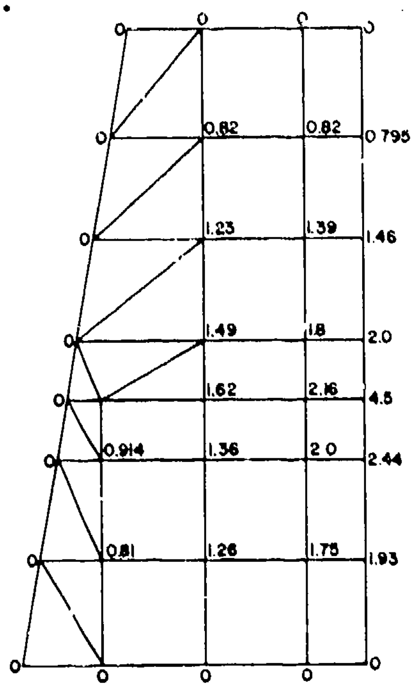

Figure 66. Out-of-plane displacement at nodes of calculation shown in Figure 65, at 0.89 ms after impact.

The outward velocity of the panel at node 16, which is 202 mm away from the impact point, is shown in Figure 67. The panel begins to move out at 80 μs after impact; this motion is due to the affects of the early-time shock, which have propagated through the aluminum. The pressure wave in the fluid arrives at about 130 μs. At that time the panel accelerates outward. At times later than about 200 μs, the panel decelerates, and by 600 μs the panel has stopped moving. This behavior is completely contrary to observation.

The deceleration of the panel can only be due to an inward-directed force. The strains in the panel at these times are too small to provide such a force. The restraining forces arise from the piston theory embodied in the BR-1A (HR) code.

The piston theory term for this node, $2P-\rho c\dot{w}$, is graphed in Figure 68. (The incident pressure can be seen in Figure 59). Note that this term is generally negative. This is because the incident pressure falls off rapidly from its initial maximum value. Physically, such an incident wave would cause the front wall to spall away from the fluid. However, the piston theory does not allow cavitation, and so a negative pressure is exerted on the panel causing it to decelerate and stop. Previous investigators have also noted this phenomenon, both in calculations[9] and experiments[25].

Another cause for error in the BR-1A (HR) treatment of entrance panel motion lies in the derivation of the incident pressures themselves. It is assumed that the pressure incident on any element of the panel is independent of the motion of other elements of the panel. This is clearly not the case. Motion of the panel in the region near the entrance hole will attenuate fluid pressure waves before they reach more distant elements. This is particularly evident in the case of the shock wave. As discussed in Section IV, the observed shock fronts are not hemispherical, which indicates that the peak pressure at the front decays more rapidly along the panel than in the fluid; this behavior is not mimicked by the calculations.

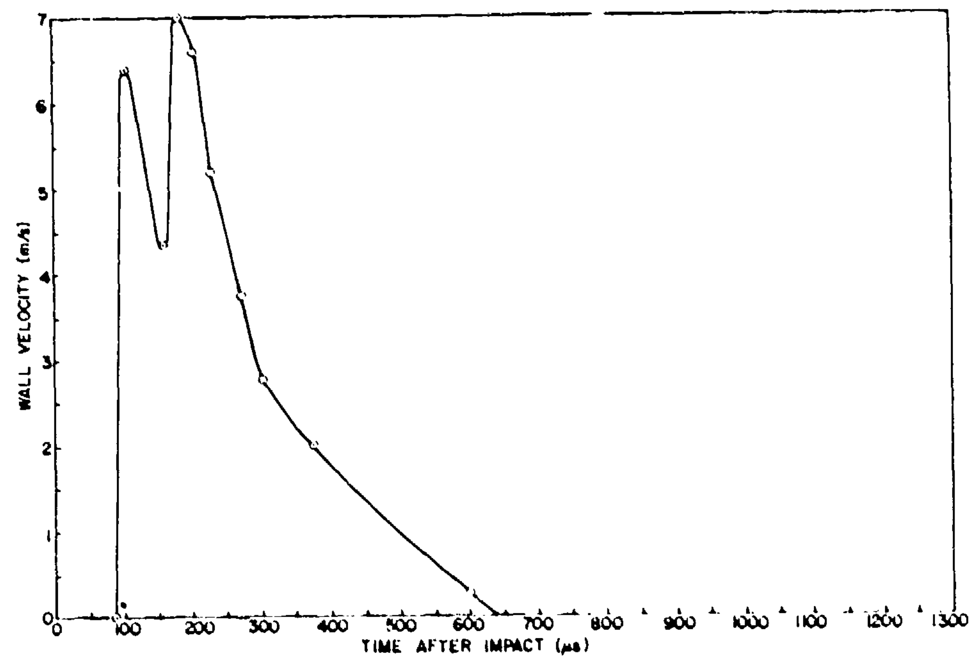

Figure 67. Panel velocity at node 16 (see Figure 64) for calculation shown in Figure 65.

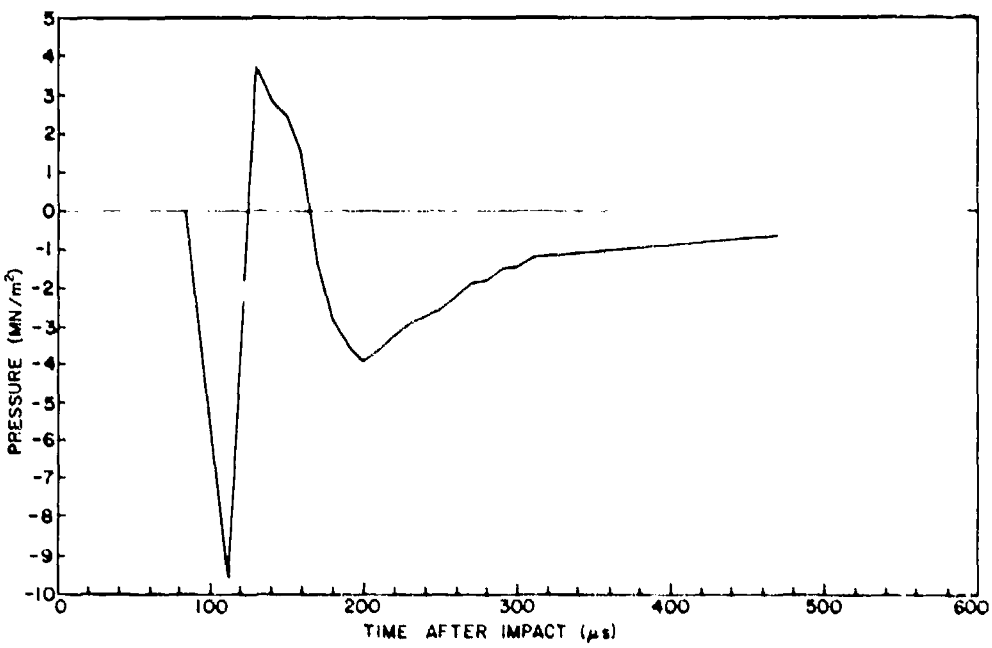

Figure 68. Piston theory pressure at node 16 for the calculation shown in Figure 65.

Note that these two sources of error are in opposite directions. The failure to treat cavitation leads to reduced displacement, while the failure to treat incident wave attenuation leads to increased displacement.

In order to evaluate the BR-1 code without the uncertainties introduced by piston theory, a calculation of the FT5 experiment was carried out using pressure data generated by the AFTON code. The pressure was calculated at points 1 mm behind the entrance panel, which was modeled by mass-loads only (e.g., no tensile strength). The pressure data supplied by CRT were integrated and interpolated by hand to derive input data for a BR-1A (run without the HR option). The results are shown in Figure 69.

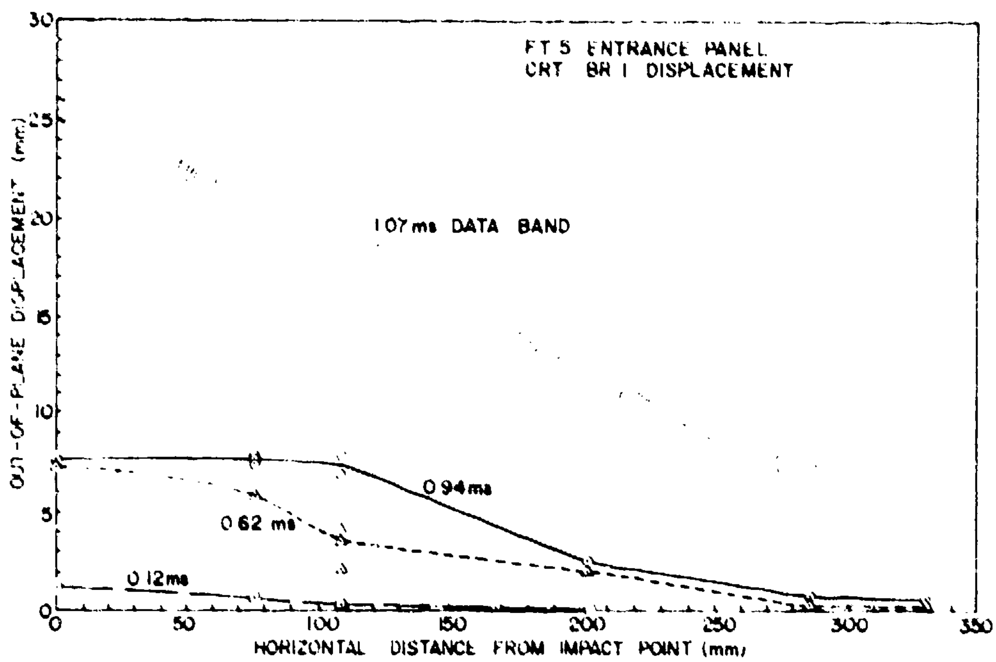

Figure 69. Comparison of BR-1A calculation with experimental data for case of 11.1 mm diameter sphere striking 1.5 mm thick 2024-T3 panel at 1.5 km/s. BR-1A was driven by pressures calculated by AFTON code.

The displacements predicted by this calculation are up to four times greater than those from the previous calculation. There has also been a significant qualitative improvement in the profile. At 940 μs the panel is continuing to move outward, and it appears the final displacements will be about twice the values at that time. The regions of relatively sharp increase in displacement at about 250 mm and 90 mm are qualitatively reproduced. Quantitative accuracy of the calculated displacement at 900 μs is still poor; the peak value is low by a factor four. It appears that beyond the immediate entrance region, final displacement will be about 50% too low.

The displacements are also considerably less than those of the corresponding NONSAP calculation (Figure A-8). At 600 μs the discrepancy is only about 15%, but in the entrance region, it is a factor 3. At 1 ms the agreement is improved because the NONSAP panel has begun to rebound, and the BR-1A panel has not.

The difference between these two calculations is apparently due to the number of elements. The NONSAP calculation used 56 annular elements. The BR-1A used 32. However, a horizontal radius in the BR-1A calculation only passes through four elements, the first of which is 76 mm wide. Given the coarse zoning, the degree of disagreement between these calculations is not unreasonable. It is also clear that the BR-1A cannot treat the region immediately adjacent to impact without a great increase in zone density, and hence running time.

One run was carried out in which the usual driving pressures were inserted into the BR-1A (HR) code, but the (HR) option was not exercised. The particular input pressures used were those from Shot FT2, which was at a 12% higher impact velocity than the shot considered above. As expected, neglect of the piston theory yielded dramatic displacements. Zones around the entrance panel failed at once. This calculation was run out to 145 μs. At that time the peak deflection was over 75 mm. Zones adjacent to the impact site were moving out at 250 m/s. Thus, neglect of piston theory is not a viable means of bringing BR-1A calculations into agreement with observation.

5.3.1.2 Case of 11.1 mm Diameter Projectile Striking 7075-T6 Entrance Panel at 1.73 km/s

This case corresponds to Shots FT2 and FT3. In both shots, the entrance panels failed catastrophically.

The FDC calculation was carried out with $C_D = 0.356$ and an entrance velocity of 1.26 km/s. The shock loading was obtained by scaling up the impulse loads from the previous calculation by the ratio of impact velocities.

No failure in any zone was predicted by the code. The computed wall deflections were once again minimal. A horizontal profile across trajectory is shown in Figure 70.

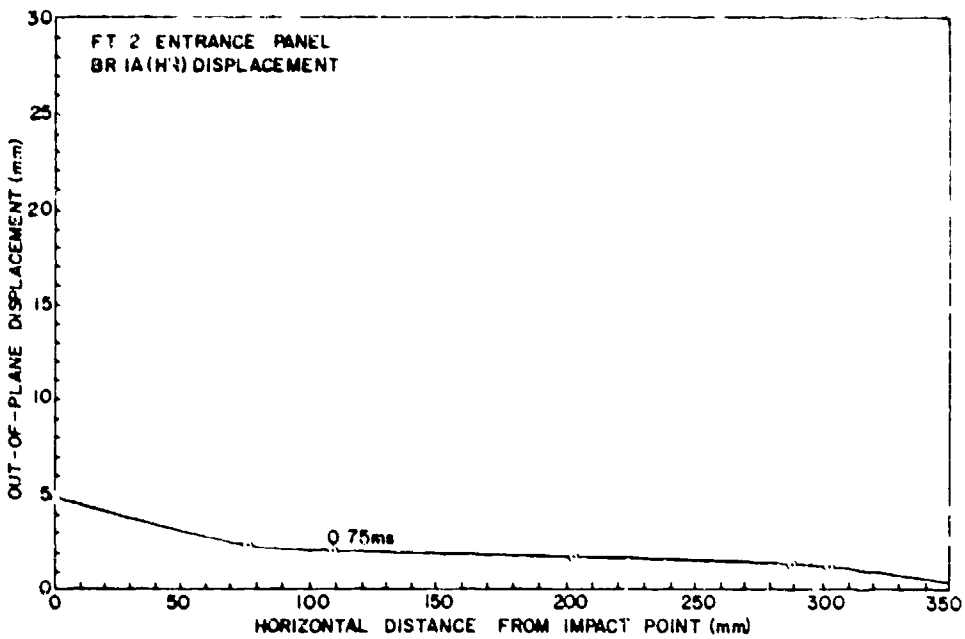

Figure 70. Displacement profile predicted for case of 11.1 mm diameter sphere striking 1.5 mm thick 7075-T6 panel at 1.73 km/s. Contrary to experiment, no failure was indicated by calculation.

5.3.1.3 Case of 14.3 mm Diameter Sphere Striking 2024-T3 Panel at 1.52 km/s.

This case corresponds to Shots FT6 and FTA9. A problem was encountered in the shock analysis for this run. The decay parameter, n, determined along trajectory, was found to be 0.988. This was apparently caused by the motion of the large projectile driving the shock. The shock fronts calculated by the fluid shock code with this value of n decayed slower than 1/r; thus, the energy deposited in the entrance panel by the shock wave increased with time. This is a non-physical effect caused by the fact that attenuation of pressure at outlaying zones by close-in zones cannot occur in the calculation. To keep some degree of reality in the input, the shock loading was arbitrarily terminated at 50 μs. The calculated wall displacements, shown in Figure 70, reveal the effect of the intense shock loading. However, no failure was indicated by the calculation, even though massive failure occurred in the actual experiment.

5.3.2 Calculations of Side Panel Motion

The elements used for calculations of side panel motion are shown in Figure 71. The nomenclature is the same as for Figure 64. The boundaries are taken as simply supported. The panel properties were chosen for 7075-T6 aluminum.

5.3.2.1 Case of 14.3 mm Diameter Sphere Striking at 1.83 km/s

This case corresponds to Shots number FT32, FT33 and FTA9. The FDC code was run with a coefficient of drag equal to 0.334. The entrance velocity of the sphere in the fluid was taken as 1.56 km/s. As noted in Section IV, the agreement of predicted and experimentally-measured fluid pressure in the tank interior was rather good for this case. The FDC calculation was carried out to 1.25 ms, at which time the panel pressures were negligible. The BR-1A (HR) calculation was carried out to 2.5 ms.

The tank displacements at trajectory height predicted by the calculation are shown in Figure 72. Again the displacements are far less than those observed for Shot FT33. The

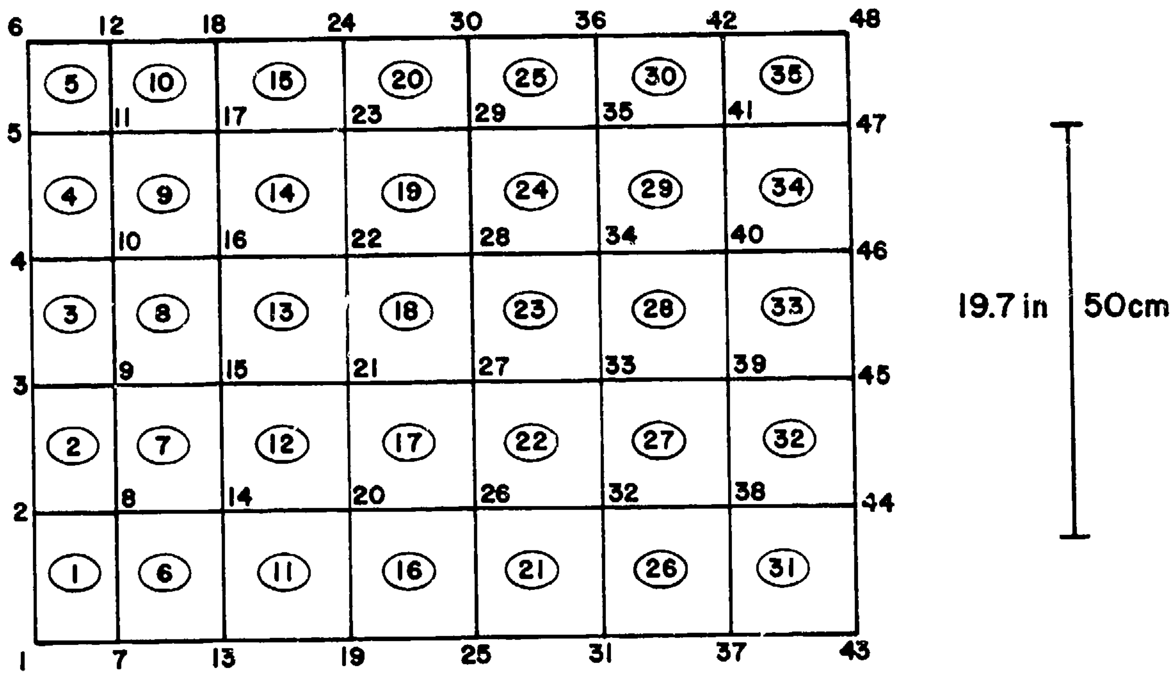

Figure 71. Element used in BR-1A calculation of side panel displacement.

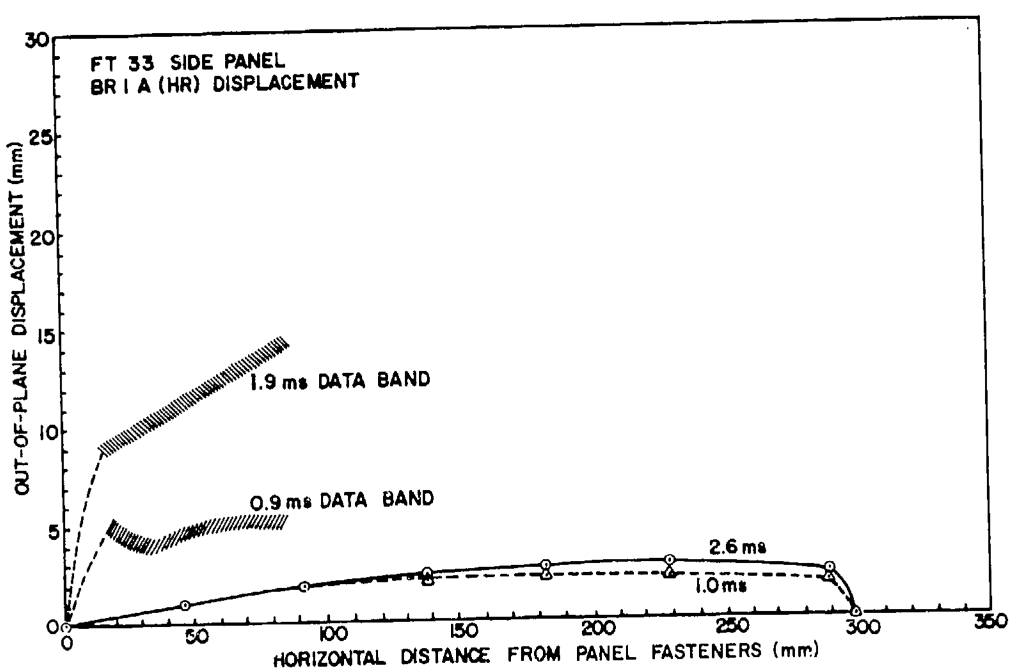

Figure 72. Comparison of side panel profile computed by BR-1A (HR) calculation and profile measured in experiment FT33.

calculated profiles show a shape which is basically correct, but especially at later times, their amplitudes are only about 15% of the actual values.

The failure of the code to account for maximum displacement is again apparently due to its neglect of cavitation. Figure 71 illustrates the computed wall velocity at a point near the center of the panel. The loading pressure applied to this region of the panel rises to a peak in 10 μs and falls to half its peak value in 30 μs; it has a second arrival at ∿200 μs after first arrival. Thus, it turns out that the piston theory term, $2P-\rho c w$, becomes negative within 100 μs. The reflected arrivals from the bottom and opposite side of the tank are evident in the velocity history. However, due to the retarding force, by 1.1 ms the panel has no outward velocity. In contrast, the actual panel has an average velocity of about 4 m/s between 0.9 and 1.9 ms and did not stop until ∿6 ms.

5.4 FINITE DIFFERENCE CALCULATIONS

Another computational routine used in this hydrodynamic ram study was the AFTON code of California Research and Technology (CRT). It is a two-dimensional, finite element wave propagation code. It is an established program, chosen for this work because it has been used on a large number of impact and penetration problems similar to hydrodynamic ram.

5.4.1 .50 Caliber Projectile Impacts

As part of the present program, several WAVE-L (a code similar to AFTON) calculations of hydrodynamic ram events were executed(5). A study of .50 caliber projectile impacts was completed and reported separately(5). A .50 caliber projectile was modeled and allowed to penetrate an axisymmetric tank through a flat entrance panel and exit the tank through a flat exit panel. The cross-sectional area of the projectile was varied to simulate the changing coefficient of drag observed during tumbling. Two tank models were used, both had 3.2 mm aluminum entrance and exit panels. The tanks had different depths, 76

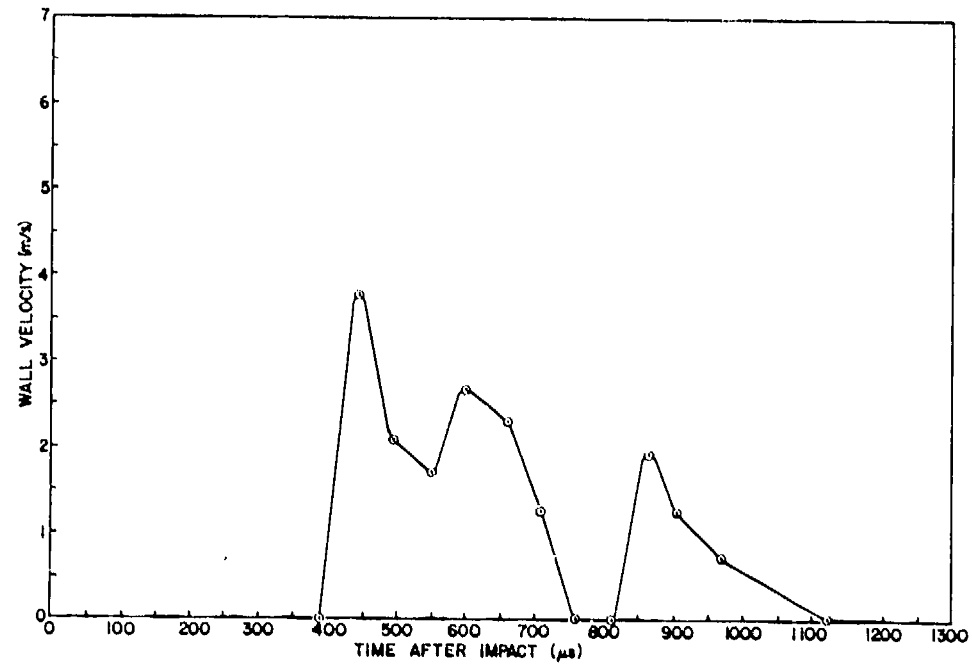

Figure 73. Panel velocity at node 27 (see Figure 71) of calculation shown in Figure 72.

and 381 mm. The 76 mm tank model was used for code verification and for an investigation of the effects of rigid foam. The 381 mm tank model was used for the principal studies where there was no foam in the tank. An illustration of the projectile penetrating the entrance wall is shown in Figure 74. As the projectile penetrated the fluid, the code calculated fluid particle velocity and pressures and tank wall motion. Fluid cavitation was observed as well as wall stresses sufficient to initiate cracks.

As the projectile traversed the 381 cm tank, it was allowed to tumble rapidly and was fully tumbled when it reached the exit wall. The resulting coefficient of drag is shown in Figure 75 contrasted to that postulated for a more slowly tumbling projectile. For comparison, the coefficient of drag of a high velocity steel sphere in water is also shown.

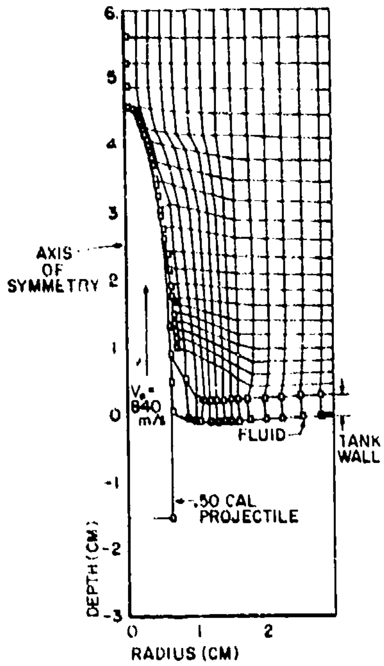

Figure 74. Finite element model of .50 caliber projectile perforating the entrance wall of a fuel tank.

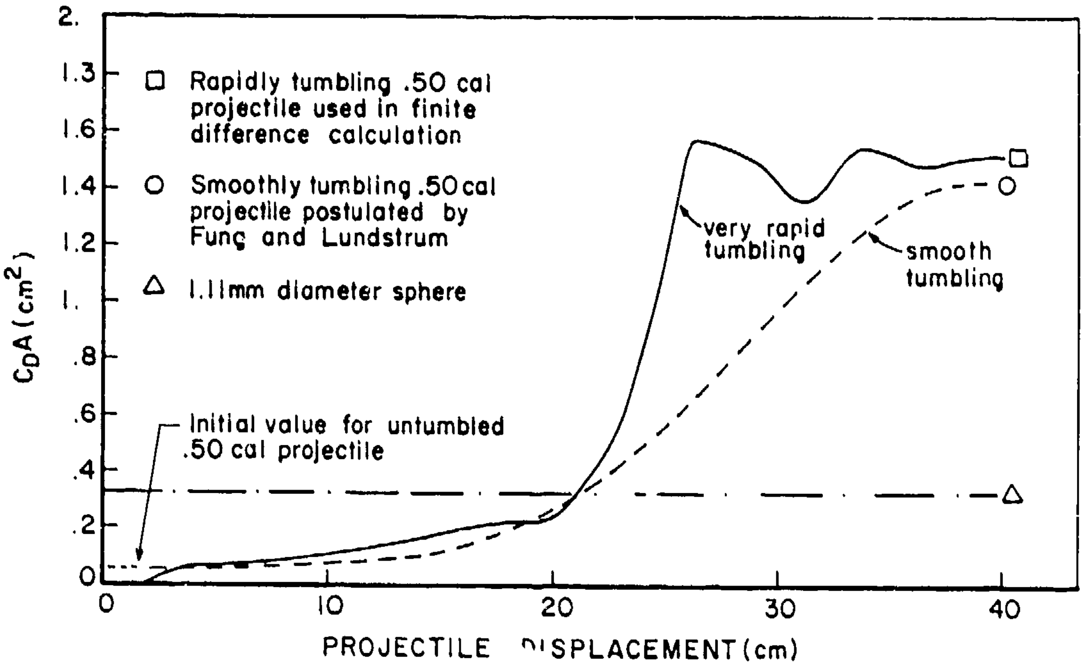

Figure 75. Drag parameter vs. projectile displacement for smoothly tumbling and rapidly tumbling projectiles and for an 11.1 mm diameter steel fragment simulator.

Rigid foam backing to the exit panel was also modeled. The equation of state for AVCO Thermarest® rigid foam was used. The compression of the foam was also computed with the finite difference code. A principal characteristic of the rigid foam is that it transfers all of the stress that it receives until that stress reaches the crushing strength of the foam (approximately 0.17 MN/m^2). The foam then yields, allowing expansion of the fluid and subsequent reduction of the fluid pressure. Studies with a one-dimensional model of the foam indicated that approximately 30 to 40 mm of foam would adequately protect a 3.2 mm thick exit panel. From these studies, it was recommended that the entrance panel be thin so that only a small amount of energy would be transferred directly to the panel during penetration. It was also recommended that the entrance panel have a large surface area backed by foam which would absorb the energy of the penetrating projectile.

5.4.2 Calculation of Hydrodynamic Ram Effects of High Velocity Fragments

For the high velocity fragment calculations a slightly different calculational technique was employed. The WAVE-L calculations conducted for the projectiles presented two important difficulties. Firstly, the Lagrangian formulation of the WAVE-L code did not model the high velocity flow around the projectile very well. Secondly, the finite difference formulation was not an efficient way to model the wall response.

The details of the calculation approach and principal results are given in Appendix A.

5.4.2.1 Outline of Approach

Recognizing that numerical solutions of impacts into fuel tanks must be efficient (inexpensive) in order to be useful, a number of important innovations were made for the high velocity fragment calculations. First, a coupled finite difference (FD)/finite element (FE) approach was implemented to avoid the serious problem which would be caused by tiny time steps if the plate were to be treated in a FD code. Second, a finite difference code (AFTON) which has characteris-

-tics which are well-suited to the fuel tank application was adapted and demonstrated.

Initially, a 11.1 mm diameter sphere at 1.55 km/s (Case A, corresponding to Shot FT5) was calculated with AFTON until the sphere penetrated many diameters and the entrance panel pressures decayed to the 0.1-1 MN/m^2 level (a time of 175 μs).

The pressure-time histories along the entrance panel provided the boundary conditions to a FE calculation (using the NONSAP code) of the panel, which was then carried out to 3 ms.

Comparisons between some of the calculated and measured panel displacements for this configuration are shown in Figure 76. (Additional comparisons are shown in Appendix A).

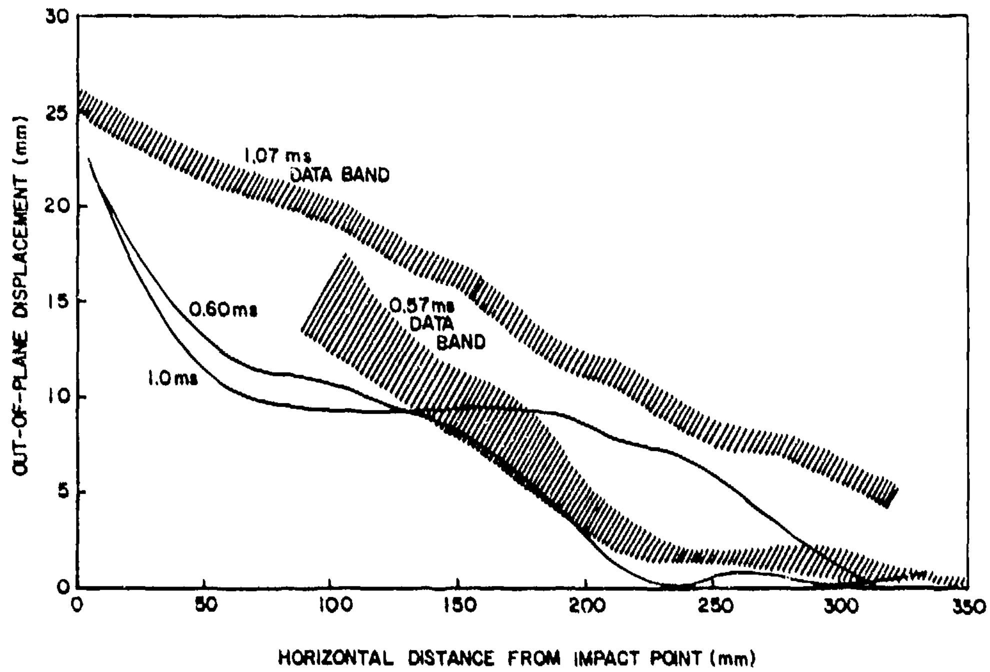

Figure 76. Comparison of AFTON-NONSAP calculation with experimental data for case of 11.1 mm diameter sphere striking 1.5 mm thick 2024-T3 panel at 1.5 km/s.

Figure 76 shows that at early times, up to about 0.6 ms, the computed and measured profiles are in approximate agreement. In fact, it can be shown that the predicted peak displacement is within the measurement uncertainty of the experimental value. However, apparently due to the premature termination of driving pressures in the calculation, the computed profiles rebound at later times, when the actual panels continued to move out. This can be seen in the figure by comparing the two profiles for 1 ms after impact.

Case B (Shot FT26), in which the panel was backed by 38 mm of foam, was then run to 175 μs on AFTON. The entrance panel pressures calculated in Case B were orders of magnitude smaller than had been calculated in Case A. It was, therefore, clear that failure would not occur in Base B, and it was decided to concentrate on an evaluation of the sensitivity of the NONSAP finite element analysis to some of the input conditions and assumptions.

Consequently, several additional NONSAP calculations of Case A were performed, namely:

(a) A FE solution was obtained of the static distortion of the panel under a uniform 0.05 MN/m^2 hydrostatic load, representing the pre-impact water head at the level of the impact point on the tank. This solution produced a maximum displacement, at the center of the panel, of 5 mm. This was about half the static displacement which was observed in the test panels. This difference indicates that the test panel shape (trapezoidal) and edge constraint conditions substantially affect its static response.

(b) The dynamic FE calculation of Case A was repeated, except that the panel was initially statically deformed to simulate the effect of the static hydrostatic load on the dynamic displacements. The minimal differences between this repeat and the original Case A analysis indicated that the initial static distortions in this case were not significant to dynamic response.

(c) Several short calculations in which the inelastic properties of the aluminum were varied did not produce changes that would significantly alter the calculated results. These trends established that the strength modeling in NONSAP was adequate.

Based on the experience gained from the preceding effort, when the third case was examined (a 14.3 mm diameter sphere impacting at 1.5 km/s) two considerations led to a first attempt of running a FE calculation (Case C-1) using the AFTON loading obtained from Case A, scaled by the ratio of the sphere diameters. First, this approach would be very attractive for future design studies of impacts onto fuel tank walls (with or without foam backing), since a single AFTON FD analysis could be used as input to several plate response, FE calculations, thereby significantly reducing costs. Second, since the entrance panel thickness doesn't scale when the sphere diameter is changed, this procedure slightly overestimates the impulse delivered to the front panel. Thus, if no difference between Case C-1 and Case A was observed, the ability of the numerical technique to predict front panel failure would be suspect. As it turned out, the resulting stresses and strains in Case C-1, as stated in the appendix, were sufficiently different from Case A to provide convincing evidence that the code solution could differentiate between plate response to various loadings.

The scaled impulses used in the foregoing step were expected to be overestimates of the test, since the actual panel thicknesses did not scale. Therefore, a FD calculation, Case C-2, with the 14.3 mm diameter sphere was run with the correct panel thickness. Peak pressure and impulses along the panel in Case C-2 were found to be only slightly smaller than the scaled values from Case A which were used in Case C-1 (see Figure A-18 in appendix). This confirmed the general validity of the scaled-loading approach. Comparisons of other measured data (sphere displacement, shock velocity, water pressures) were excellent.

Original plans for a second foam-backed panel calculation were abandoned because the Case B results and the experimental data showed that the 38 mm thick foam was considerably thicker than needed to prevent fractures. Thus, another calculation with such a thick foam layer would not be expected to produce any additional information. The remaining effort was, therefore, expended on examining refinements of the numerical techniques which could substantially reduce the cost per case and improve accuracy of these solutions.

5.4.2.2 Conclusions

The principal conclusions from the AFTON-NONSAP calculations are as follows:

1. The AFTON code is capable of accurately generating the pressure field within the fluid for the length of time that loading of the entrance panel is significant.

2. AFTON-driven NONSAP calculations can predict displacement profiles which are qualitatively correct. It appears that it will not be difficult to predict failure by these means. The AFTON-NONSAP features responsible for inaccuracies in displacement predictions are simplified boundary conditions, axial symmetry assumption, and premature termination of the driving pressure.

3. AFTON results can be simply scaled to account for variation in projectile diameter.

SECTION VI
SUMMARY AND CONCLUSIONS

Hydrodynamic ram effects induced by high-velocity fragments have been studied with experimental and analytical and numerical techniques. The projectiles were 11.1 and 14.3 mm diameter steel spheres traveling in excess of 1.5 km/s.

It was found that:

1. High velocity projectiles constitute a severe threat to entrance panels.

2. 2024-T3 aluminum alloy is far more resistant to ram damage than 7075-T6 aluminum alloy.

3. Both ballistic foam and styrofoam are extremely effective in defeating entrance panel hydrodynamic ram.

4. The dynamics of entrance panel motion and failure are as follows: The impact induced shock wave produces extremely high pressures over the area immediately adjacent to the impact site; however, the duration of the shock pressure is only tens of microseconds. During the time that significant loads are applied, the response of the panels is largely inertial. Most of the impulse is transferred to the panel before it has strained appreciably. The outward motion of the panel then proceeds at a relatively slow rate; the major displacement step propagates at only ∿300 m/s. The hoop stresses due to the deformation induced by the shock may cause very early tensile failure at the entrance site. If this occurs, cracks propagate out as the panel displaces. Thus, the critical physical processes in an entrance panel event take place within a few tens of millimeters of the entrance site during the first hundred microseconds after impact.

5. The local nature of entrance panel phenomena permits meaningful experiments to be carried out in small scale tanks.

6. The moiré fringe device developed for this program can be used to measure hydrodynamic ram-induced panel motions with sufficient accuracy and resolution to check numerical predictions.

7. The fluid drag code developed at NWC provides an adequate description of fluid pressure in the tank interior.

8. The fluid shock code embodies assumptions about wavefront shape and velocity decay which are clearly violated in hydrodynamic ram events.

9. The BR-1A (HR) code is not able to adequately predict hydrodynamic ram-driven panel motions. The principal reasons apparently involve the basic nature of the piston theory embodied in the code.

10. When driven by AFTON-generated pressures, the BR-1A can probably provide a sufficient description of panel motions.

11. The AFTON-NONSAP calculations of panel displacement are qualitatively correct. Small refinements of the technique will probably yield excellent quantitative predictions of panel shape as well as a failure criterion.

12. 2024-T3 aluminum alloy panels 1.5 mm thick fail catastrophically when struck by a 11.1 mm diameter sphere above ∿1.5 km/s.

13. A layer of ballistic foam equal to the projectile diameter defeated a 2.38 km/s impact.

14. In the configuration used here, no side panel or exit panel failures occurred.

15. Partial results indicate foam is of marginal utility in defeating ram effects at exit panels.

APPENDIX A

This Appendix was prepared by California Research and Technology under subcontracts RI-76884 and 77713 for the University of Dayton Research Institute, Dayton, Ohio.

APPENDIX A

FINITE DIFFERENCE/FINITE ELEMENT ANALYSIS OF FUEL TANK PENETRATION BY STEEL FRAGMENTS

Sheldon Schuster
Y. Marvin Ito

California Research & Technology, Inc.*
Woodland Hills, CA 91367

A.1 INTRODUCTION AND APPROACH

A.1.1 Prior Study

In a previous study by CRT[1], the WAVE-L two-dimensional (2-D) Lagrangian finite difference code was used to investigate the dynamics of .50 caliber bullets penetrating fuel tanks, with particular attention being given to damage to the *exit* panel, i.e. the rear surface of the tank which is penetrated after the projectile passes through the fuel. The impacts were at normal incidence with no yaw, but tumbling was simulated by continuously changing the shape and frontal area of the bullet to match an assumed time-dependent drag force.

A.1.2 Objectives of Present Study

In the current computational program, a study has been performed of the effects of steel spheres (representing chunky fragments) impacting the *entrance* panel of aluminum tanks (filled with water simulating fuel), with and without foam backing. The problems which were numerically analyzed during this study are shown in Table A-1.

---

* This work was performed by CRT under Subcontract RI-76884 and RI-77713 with University of Dayton Research Institute.

[1] M. Rosenblatt, G. E. Eggum, and L. A. DeAngelo, "Numerical Analyses of Fuel Tank Penetration Dynamics, AFFDL-TR-76-31, California Research & Technology, Air Force Flight Dynamics Lab., April 1976.

TABLE A-1. CONDITIONS FOR CRT CALCULATIONS AND EXPERIMENTAL COMPARISONS

CRT Case	Impacting Sphere			Entrance Panel		UDRI Test	Actual Test Velocity (m/sec)	Observations Available for Comparison
	Dia (cm)	Mass (gm)	Velocity (m/sec)	2024-T3 Al Thickness (cm)	AVCO Ballistic Foam Thickness (cm)			
A	1.11	5.5	1550	0.16	0	FT5B	1550	o Time-resolved entry panel profiles o Damage severity
B	1.11	5.5	1550	0.16	3.8	FT26A	1520	o Final profile of entry panel o Damage severity
C-1*	1.43	11.0	1550	0.16	0	FT6	1520	o Damage severity
C-2	1.43	11.0	1500	0.16	0	FTA9	1460	o Projectile displacement history o Shock arrival times

* using Phase I output of Case A scaled by 1.43/1.11 = 1.29

The objectives of these calculations were (1) to implement new and more efficient numerical methods for analyzing fragment and projectile impacts into fuel tanks, and (2) to validate these methods, insofar as possible, by comparing numerical results with dynamic observations of the penetration and response processes occurring in tanks impacted by steel spheres. These observations were obtained by UDRI in connection with the experimental program described in the main body of this report.

A.1.3 Numerical Techniques

A two-phase analysis method was employed: In Phase I, an adaptation of the AFTON 2-D finite difference code[2] was used to calculate the *penetration dynamics* and to determine the time-resolved force loading between the water and the tank wall. In Phase II, the *tank wall response* was calculated by applying this force loading as a boundary condition in a NONSAP 2-D finite-element code[3] solution. This approach of partially decoupling the penetra on and response assumes that the penetration dynamics are largely unaffected by the rigidity of the front plate (although the plate mass and inertia are correctly taken into consideration). This is a reasonable assumption during the early stages treated by the Phase I analysis.

a. AFTON Finite Difference Code

The AFTON code was selected for this study because of its ability to continuously redefine the Lagrangian mesh spacing. This capability reduces the large distortions which occur in these problems when the mesh moves in the normal Lagrangian manner with the material. In the Phase I calculations,

---

[2] W. J. Niles, J. F. Germroth, and S. H. Schuster, "Numerical Studies of AFTON 2A Code Development and Applications, Vol. II," AFWL-TR-70-22 Vol. II, February 1971.

[3] K-J Bathe, E. L. Wilson, and R. H. Iding, "NONSAP - A Structural Analysis Program for Static and Dynamic Response of Nonlinear Systems", Structural Engineering Laboratory, University of California, Berkeley, California, UC SESM 74-3, February 1974.

the mesh points defining both the front surface of the water and the cavity behind the penetrator moved with the particle velocity associated with the material (i.e. Lagrangian). However, interior mesh points (within the fluid) were continuously rezoned toward positions nominally equidistant from their neighbors. As illustrated by the plot of the mesh in Figure A-1, after the sphere has penetrated about one diameter, the severe distortions of the mesh usually associated with pure Lagrangian calculations are minimized by the AFTON technique. At the same time, the motion of the boundaries, which would be lost if the mesh were fixed in space and time as in pure Eulerian formulations, has been preserved.

In the Phase I calculations, the 0.16-cm (1/16-in.) aluminum entrance panel was modeled by attaching the inertial mass of the aluminum to the mass of the mesh points along the front surface of the fluid. Material models for the water and foam were the same as used in the previous study.[1] The steel sphere was treated as a rigid body.

The Phase I calculations were stopped before the first signal reached the nearest side wall of the tank (at r ~ 37.5-cm), and when pressures everywhere along the entrance panel were less than 10 bars (~ 150 psi). The pressure vs time data along the front panel were then used to derive the force loading for the subsequent Phase II NONSAP structural response calculation.

b. NONSAP Finite Element Code

NONSAP is an implicit, 3-D, non-linear finite element code which was selected for the second phase of this study in order to adequately and efficiently model the large deflections of the thin entrance panel. (A finite difference code analysis of this thin plate response would be difficult, due to the very small time step imposed by the explicit stability criterion.) The finite element calculations assumed the front panel was a 37.5-cm radius disc of 2024-T3 aluminum, rigidly supported around its edge, and with a circular hole in the center the size of the impacting sphere. The zoning and material model

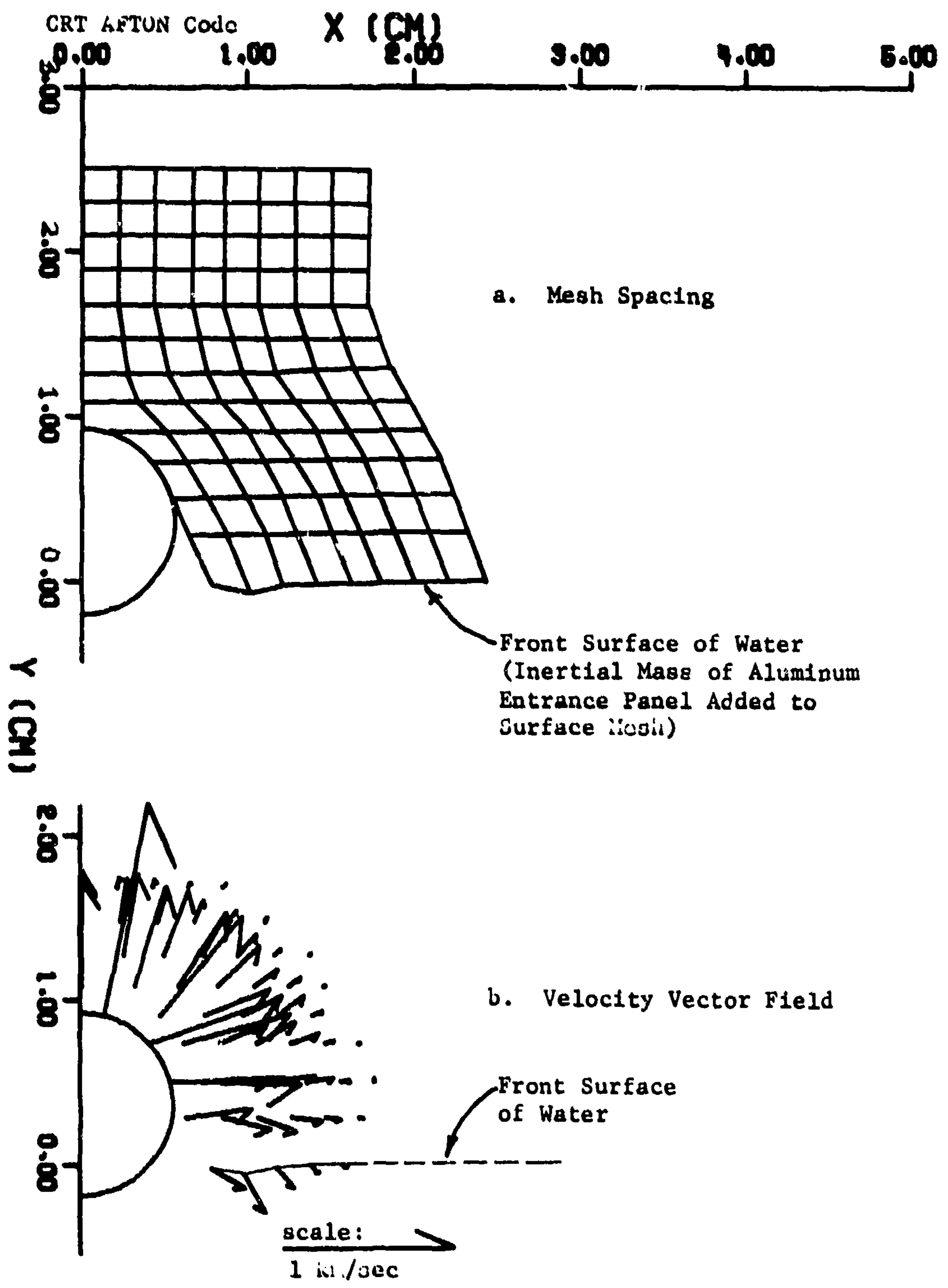

Figure A-1. Mesh Spacing and Velocity Vector Field in Water at 6.2 μsec After Impact. CRT Case A: 1.11-cm Steel Sphere Impact at 1550 m/sec

used are illustrated in Figure A-2. No failure criterion was specified for the aluminum, so only elastic and continuous plastic deformation are allowed. An axisymmetric model of the entrance panel was assumed (instead of the trapezoidal-shaped panel used in the UDRI experiments) so that a 2-D version of NONSAP could be employed. This allowed better representation of the impulsive force input and of the highly nonlinear response of the plate.

ENTRANCE PANEL GEOMETRY:

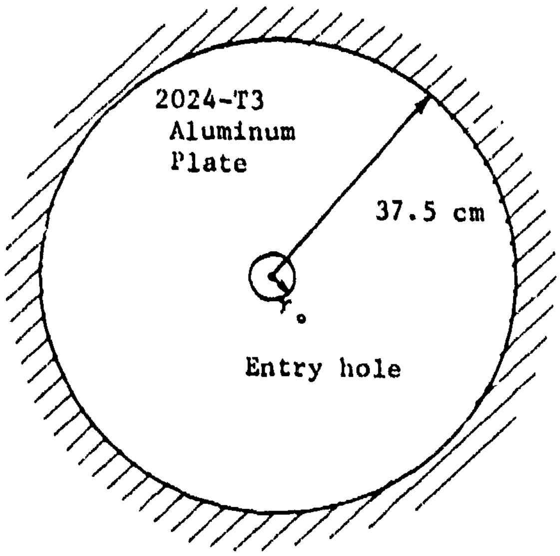

END VIEW

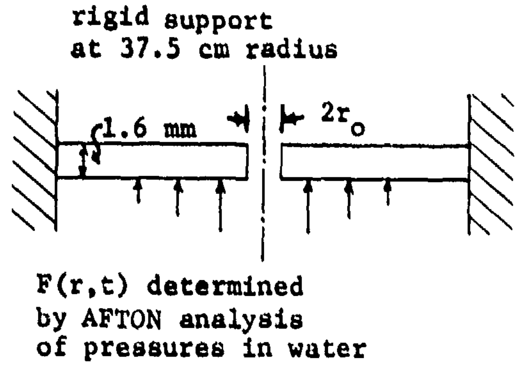

CROSS-SECTIONAL VIEW

2024-T3 ALUMINUM
MATERIAL MODEL:

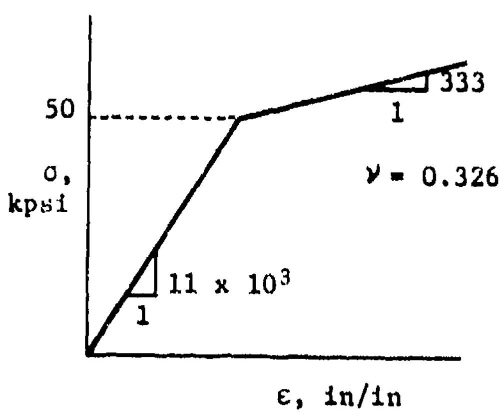

GRID SIZE:

$2r_o$	No. Elements	No. Nodes
11.1 mm	56	283
14.3 mm	55	278

TIME STEP:

$\Delta t = 2\ \mu sec$

Figure A-2. NONSAP Finite Element Axisymmetric Model of the Entrance Panel of the Fuel Tank

A.2 RESULTS OF THE CALCULATIONS AND EXPERIMENTAL COMPARISONS

A.2.1 CRT Case A: Impact of 1.11-cm dia Steel Sphere at 1550 m/sec into Water Tank with 0.16-cm (1/16-in.) Aluminum Wall

A.2.1.1 Calculations

The progress of the 1.11-cm dia steel sphere (5.5 gm) through the water in the fuel tank at 6.2, 36.1, and 78.2 μsec is illustrated in the series of velocity vector fields in Figures A-1, A-3, and A-4, respectively. At 6.2 μsec (Figure A-1), the sphere has penetrated almost a full diameter and cavitation has begun. As the sphere continues to penetrate, more and more mesh points are automatically activated so that by 136 μsec, 3500 points were included in the problem. Since the motions of the front panel were of primary interest, all zones at depths greater than 10 cm were replaced in the calculation after 136 μsec by a reflecting boundary condition. (Reflection from this boundary would not be felt at the front panel during the time of interest.) The Phase I calculation was continued to 178 μsec. By this time, the pressures along the front panel had decayed to less than a bar (~ 15 psi) everywhere except within 5 cm of the axis, where several zones were still at about 10 bars.

Time histories of the instantaneous peak pressure in the water, and of the velocity and displacement of the sphere, are shown in Figure A-5. After impact, the calculated peak pressure in the water (which always occurs just ahead of the penetrating sphere) decays rapidly as the initial shock wave expands. At times greater than 25 μsec the peak is essentially the dynamic pressure ($1/2\ \rho U^2$), where U is the instantaneous velocity of the sphere and ρ is the fluid (water) density. The expected dynamic pressure (determined from the calculated instantaneous velocity of the sphere) is shown by the smooth curve in Figure A-5a. As is seen, the peak pressure directly calculated by the code closely follows the $1/2\ \rho U^2$ curve after 25 μsec.

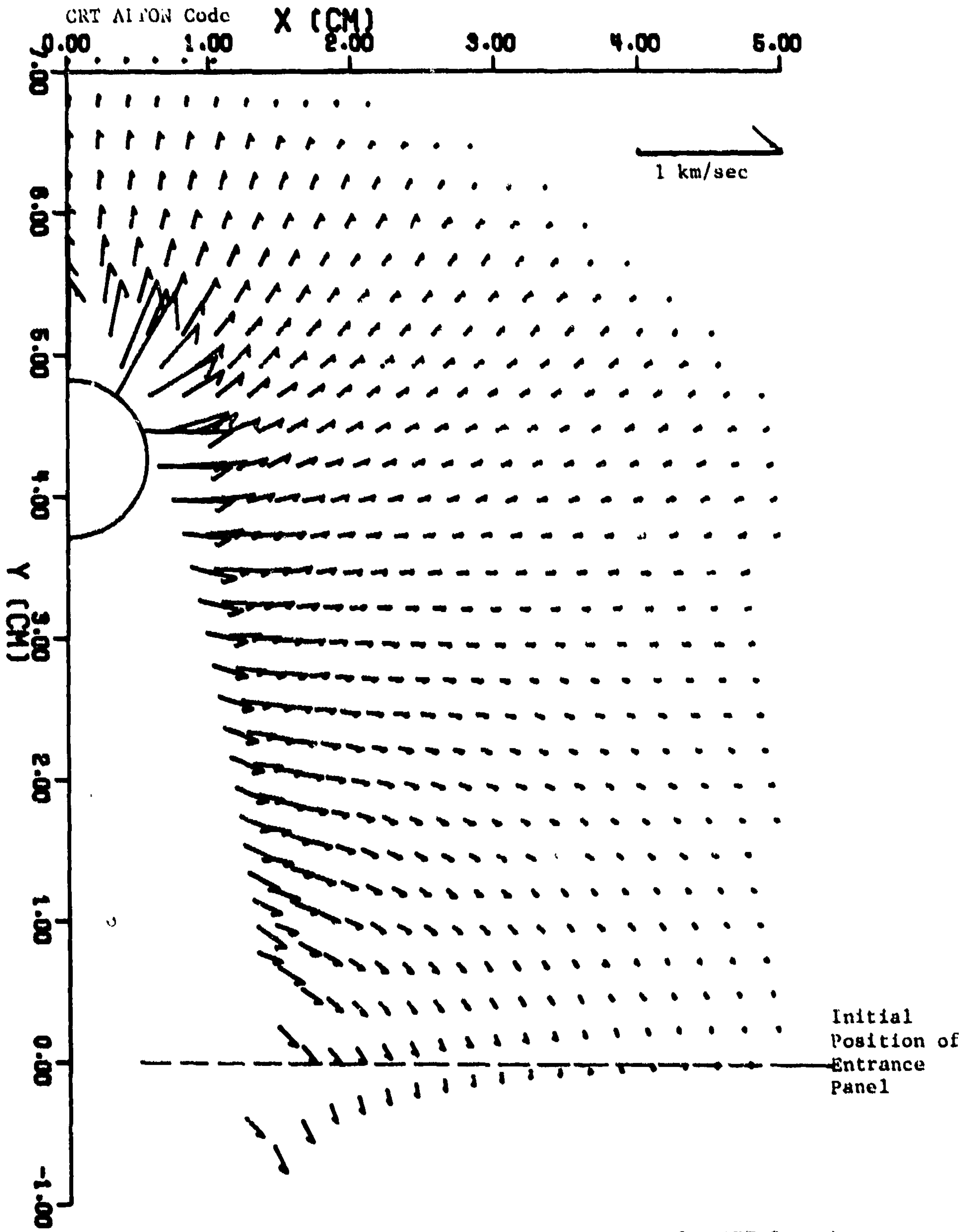

Figure A-3. Velocity Field in Water at 36 μsec for CRT Case A: 1.11-cm dia Steel Sphere Impacting at 1550 m/sec

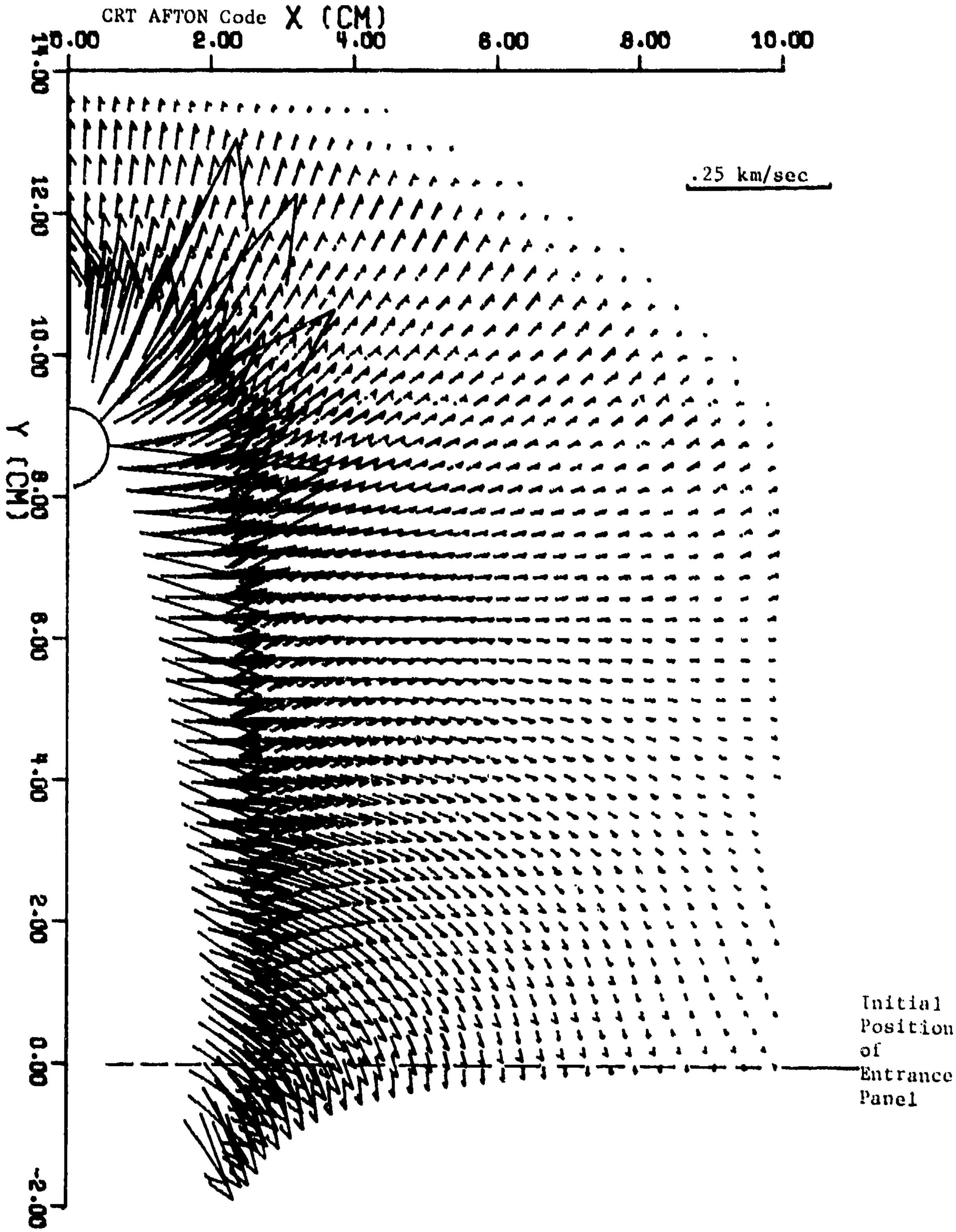

Figure A-4. Velocity Field in Water at 78.2 μsec for CRT Case A: 1.11-cm dia Steel Sphere Impacting at 1550 m/sec

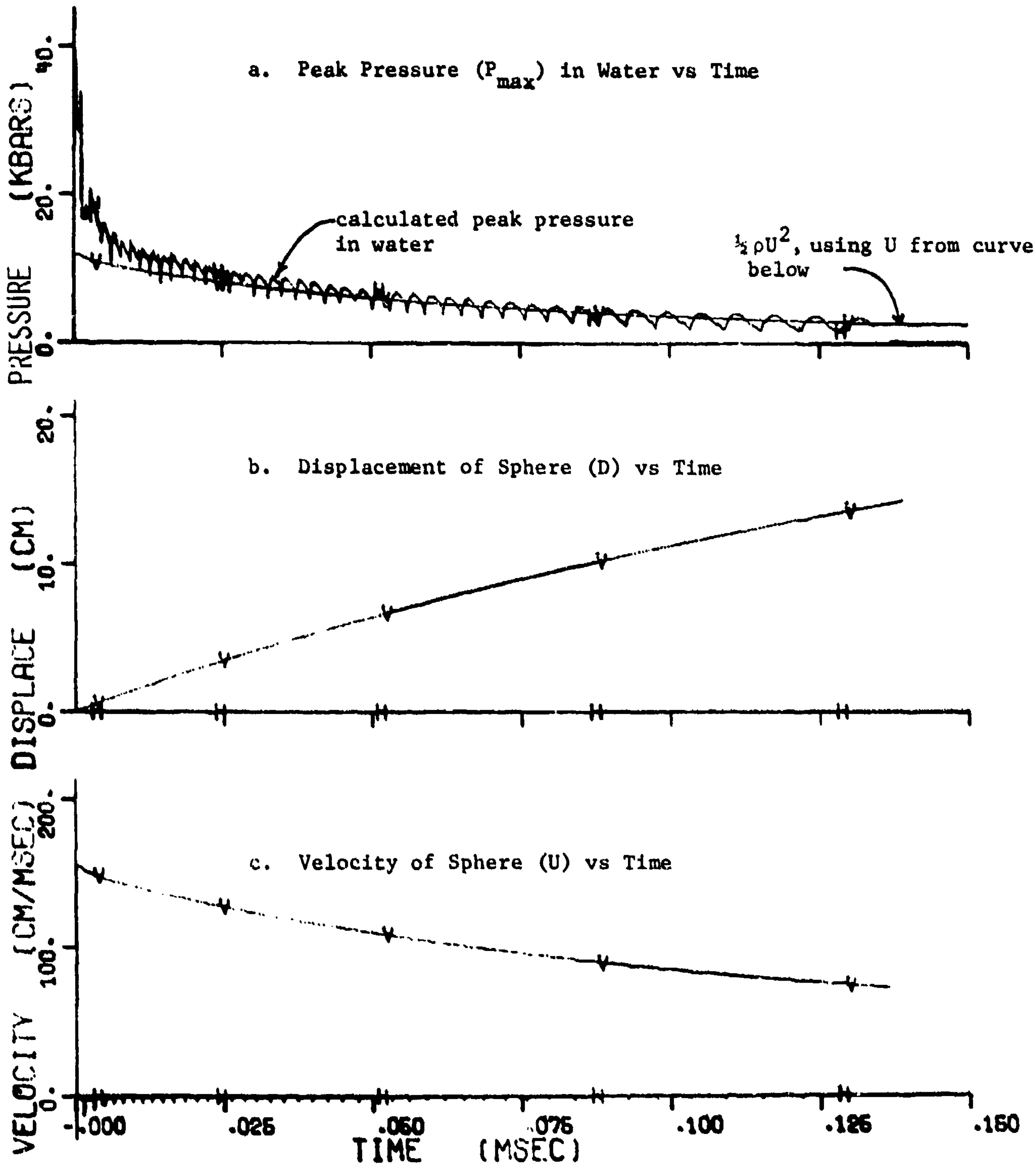

Figure A-5. Time Histories of the Peak Pressures in the Water, and of the Displacement and Velocity of the Sphere. CRT Case A: AFTON Code Solution of 1.11-cm dia Steel Sphere Impact at 1550 m/sec

The oscillations in the calculated peak pressure come about because the pressure periodically decays in one zone and increases in the next, consistent with the zone engulfment time of the pressure wave through the mesh.

The effective drag coefficient, C_D, of the penetrating sphere can be estimated by fitting the calculated velocity, U, and displacement, D, histories in Figure A-5 with the equation

$$U = U_o e^{-\beta D} \tag{A-1}$$

where U_o = 1550 m/sec (the impact velocity) and with β = .055. C_D and β are related by

$$C_D = \frac{8}{3} \frac{\rho_s r_o}{\rho_w} \beta \tag{A-2}$$

where ρ_s and ρ_w are the respective densities of the sphere and fluid (steel and water), and r_o is the sphere radius.

During the first 130 μsec after impact, the above fit leads to a value of C_D = 0.62. Initially, the drag coefficient is much higher (C_{Do} ~ 1.2), but it decreases to the effective value (C_D ~ 0.6) within about 1 dia of penetration.

Time histories of the pressure 5 cm from the axis of symmetry and at 2,5 and 10 cm depth are plotted in Figure A-6. The duration of the first pulse broadens with depth as the time difference between the arrival of the initial wave and the relief waves originating from the front surface increases. Figure A-7 shows peak pressure vs radius points within the tank and along the front surface; these decrease with distance from the axis for each depth.

Pressure-time histories along the entrance panel out to 178 μsec from the Phase I AFTON finite difference calculation were used in Phase II as the forcing functions in the NONSAP finite element code. These forces were applied to the inside surface of a 37.5-cm dia disc of 0.16-cm (1/16-in.) thick aluminum, as indicated in Figure A-2. The calculated displacement profiles of the aluminum plate at 200 μsec intervals are plotted in Figures A-8 and A-9. The peak displacements ranged

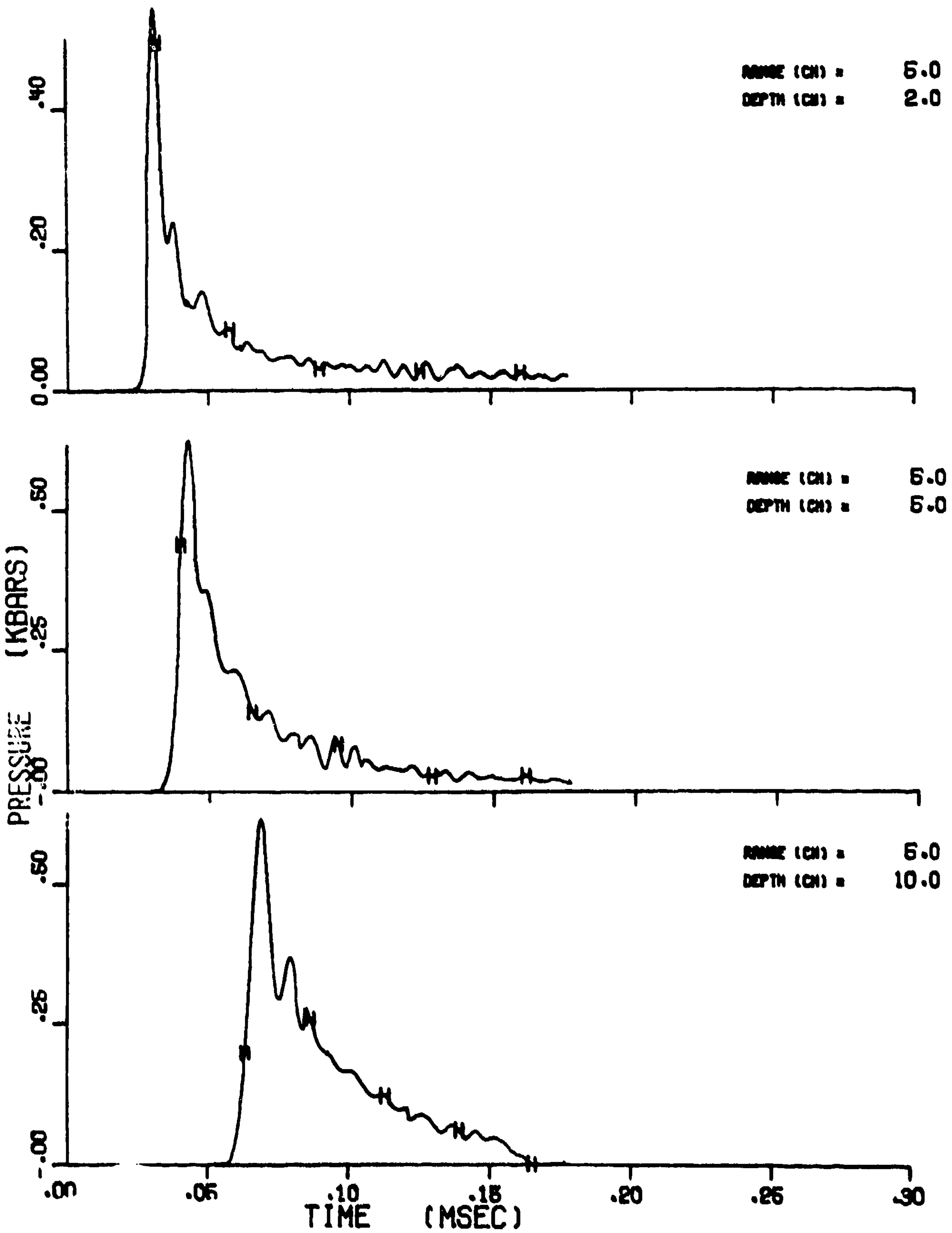

Figure A-6. Time Histories of the Pressure in the Tank. CRT Case A: 1.11-cm Dia Steel Sphere Impacting at V_0 = 1550 m/sec at Points 5 cm off the Axis of Symmetry and at 2,5 and 10 cm Depth from the Entrance Panel

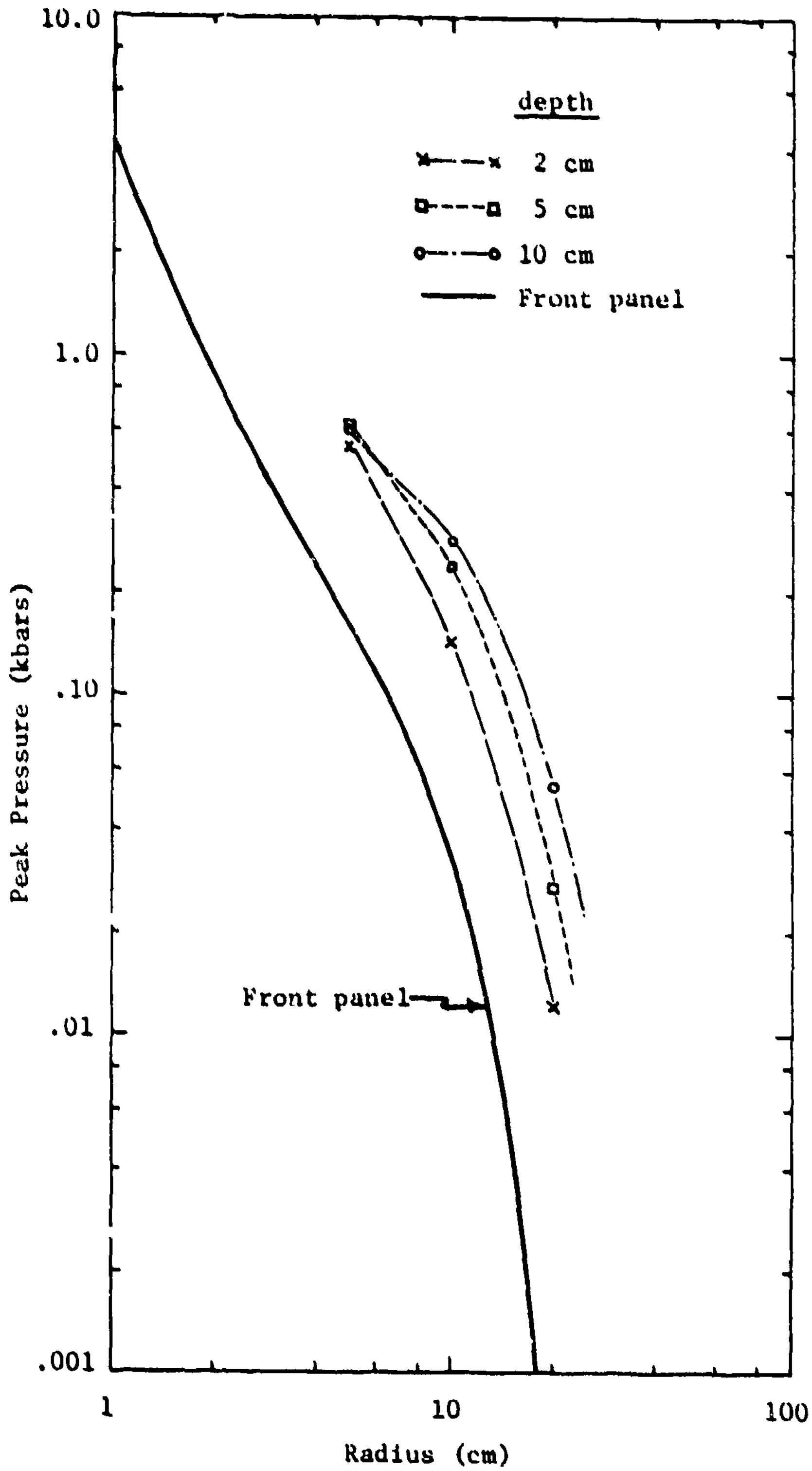

Figure A-7. Peak Pressure Experienced along the Front Panel and at Selected Points in the Tank as a Function of Distance from the Axis of the Spherical Fragment. CRT Case A: 1.11-cm dia Steel Sphere Impacting at 1550 m/sec

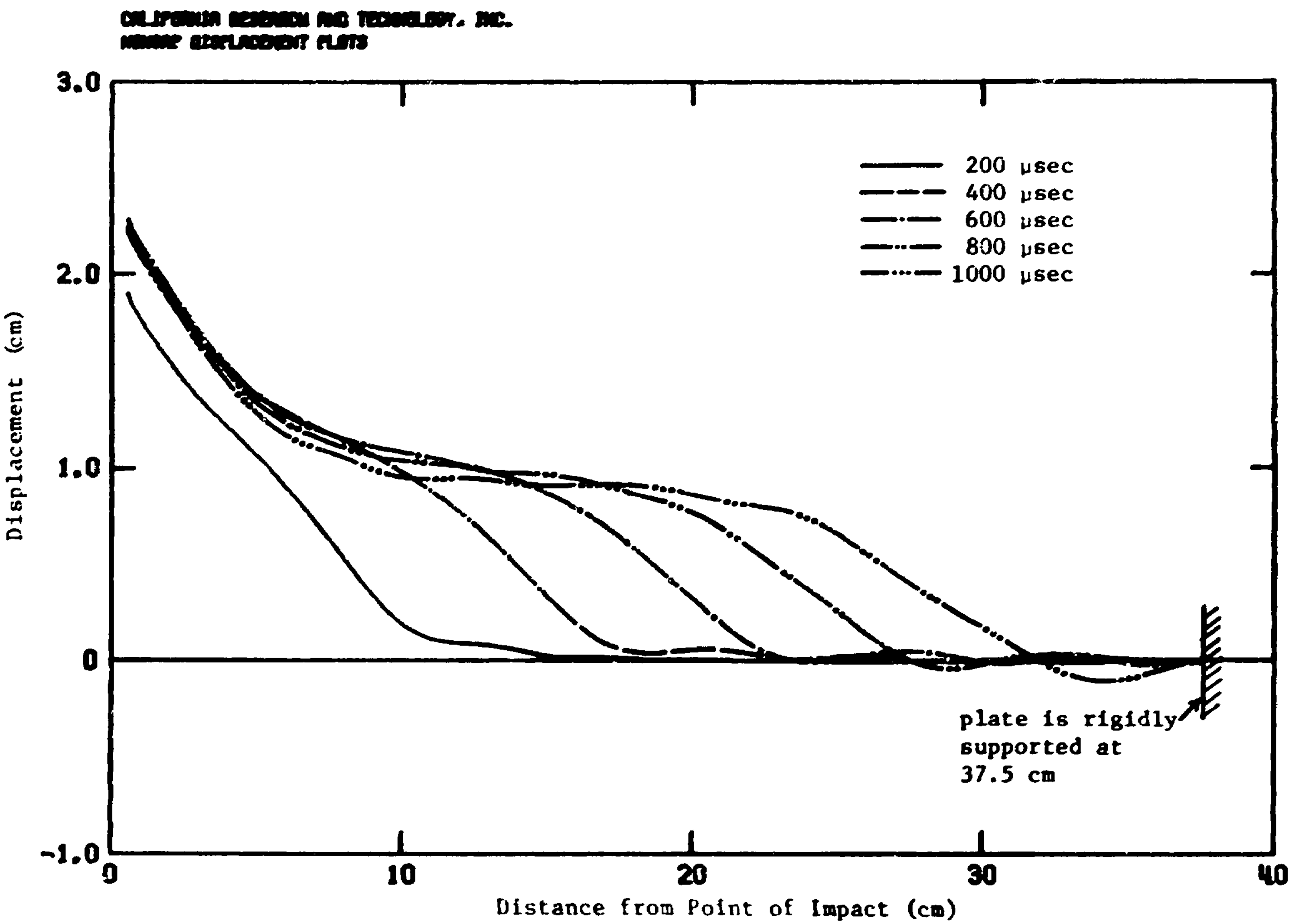

Figure A-8. Calculated Displacement Profiles along the 0.16 cm Aluminum Entrance Panel at Sequence of Times Between 200 and 1000 μsec After Impact. CRT Case A: 1.11-cm Dia Steel Sphere Impacting at V_o = 1550 m/sec

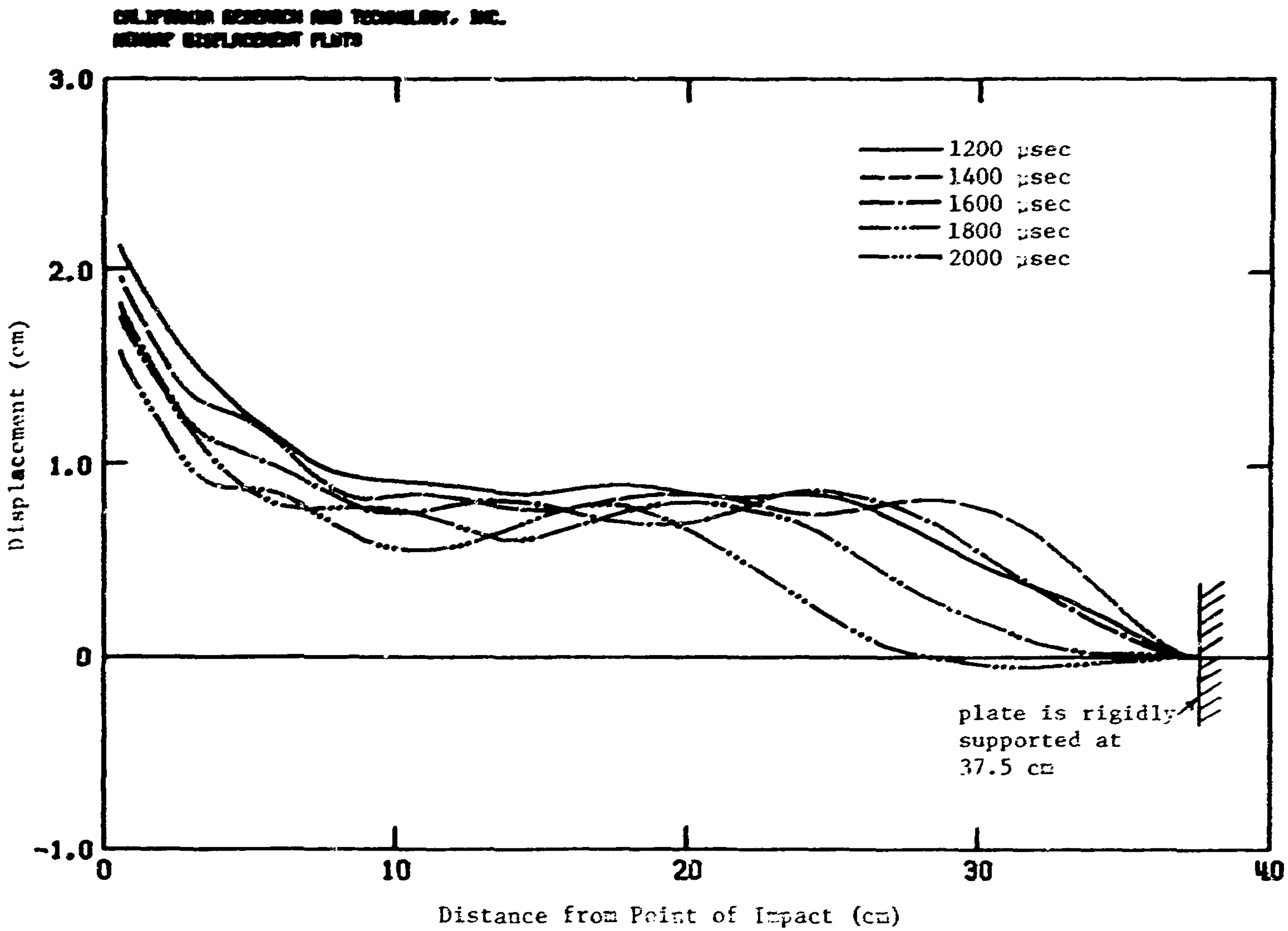

Figure A-9. Calculated Displacement Profiles along the 0.16-cm Aluminum Entrance Panel at Sequence of Times Between 1200 and 2000 μsec After Impact. CRT Case A: 1.11 cm Dia Steel Sphere Impacting at V_o = 1550 m/sec

from about 2.2-cm near the entry hole to about 1-cm at radii between 10 and 30 cm.

The calculated tensile hoop stresses which developed in the impacted aluminum plate as it deforms are shown in Figure A-10. Close to the axis, these stresses reach a maximum quite early ($t < 200$ μsec) and then decay as more of the disc is engulfed by the shock wave. Only a small region (out to about 4-cm in radius) of the disc attains stresses above the nominal 70 kpsi tensile limit of 2024-T3 aluminum. It is therefore, reasonable to expect that any radial cracks which might form around the hole will not propagate. It is pointed out that the peak stresses and strains which would lead to possible failure develop early in the analysis, prior to the end of the Phase I calculation.

A.2.1.2 Experimental Comparisons

The conditions for UDRI Test FT5B correspond approximately with CRT Case A. Experimental observations of the dynamic distortion of the entrance panel were made in this test, using the experimental arrangement in the sketch:

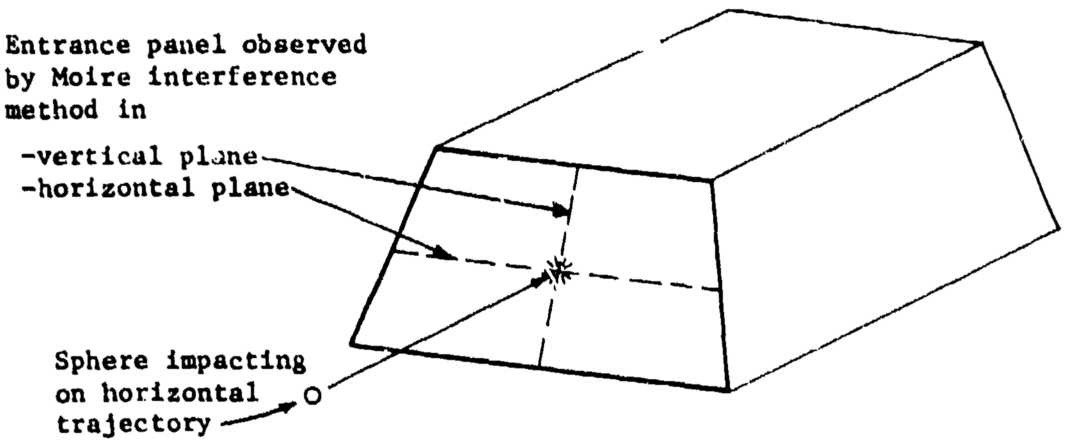

Figures A-11 and A-12 show sequences of entrance panel profiles in horizontal and vertical planes, as observed by the Moire interference technique. The nominal inter-frame time in these observations was 160 μsec. The impact time is thus known

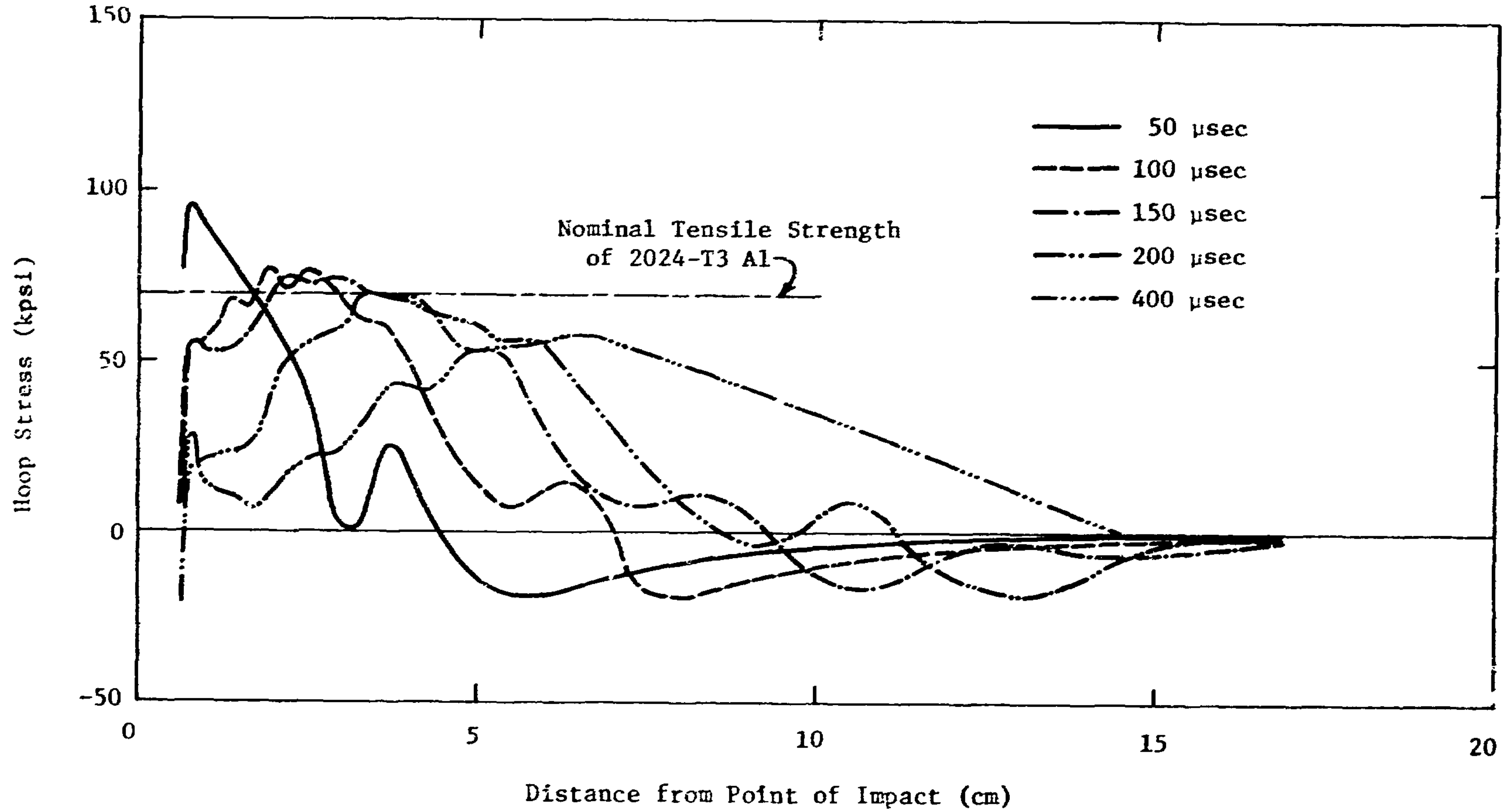

Figure A-10. Calculated Hoop Stress in 0.16-cm (1/16-in.) Aluminum Entrance Panel vs Distance from Point of Impact. CRT Case A: 1.11-cm Dia Steel Sphere Impacting at 1550 m/sec

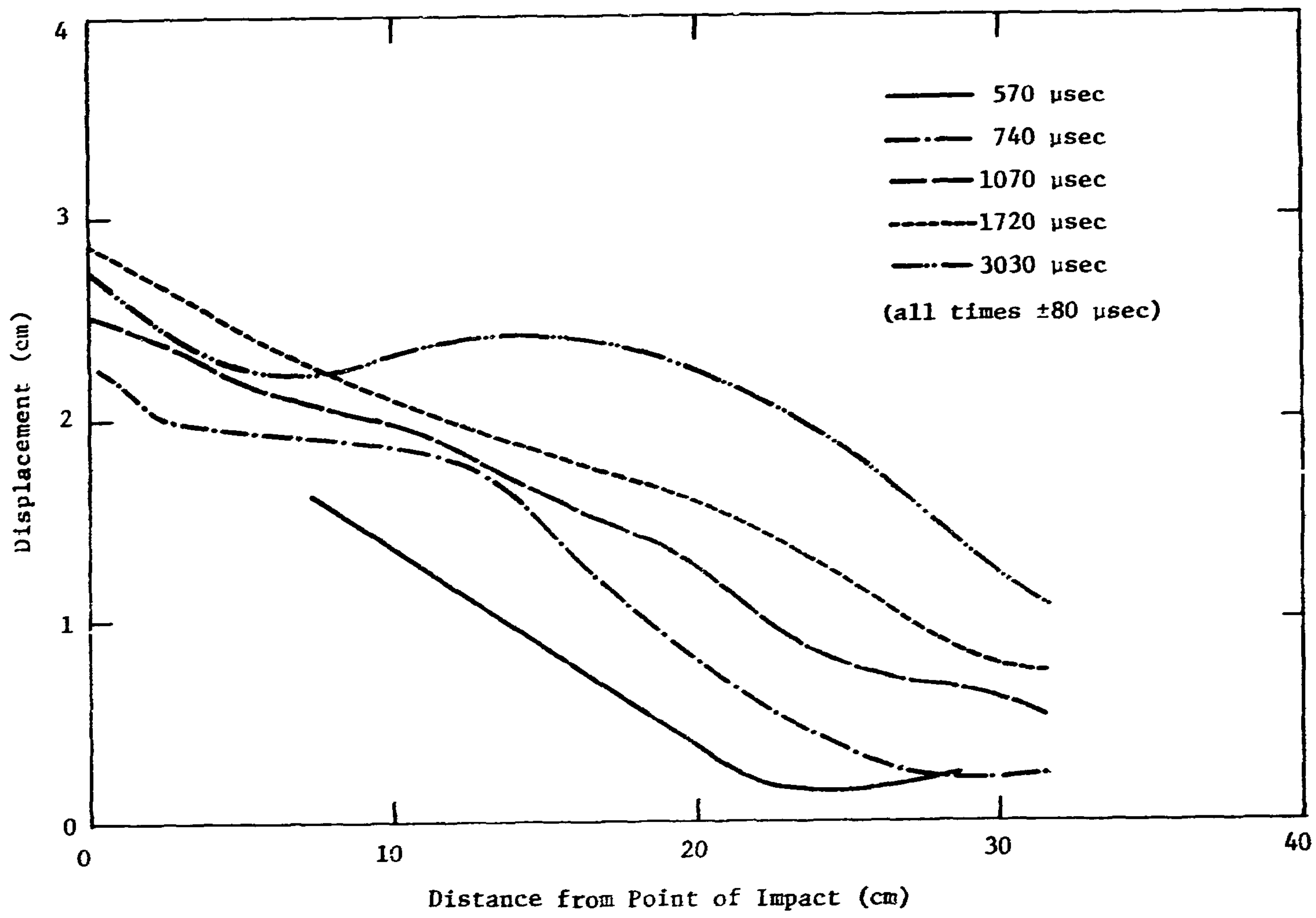

Figure A-11. Experimental Displacement Profiles Measured Along a Horizontal Line through the Impact Point. UDRI Test FT5B: 1.11-cm Dia Steel Sphere Impacting at 1550 m/sec

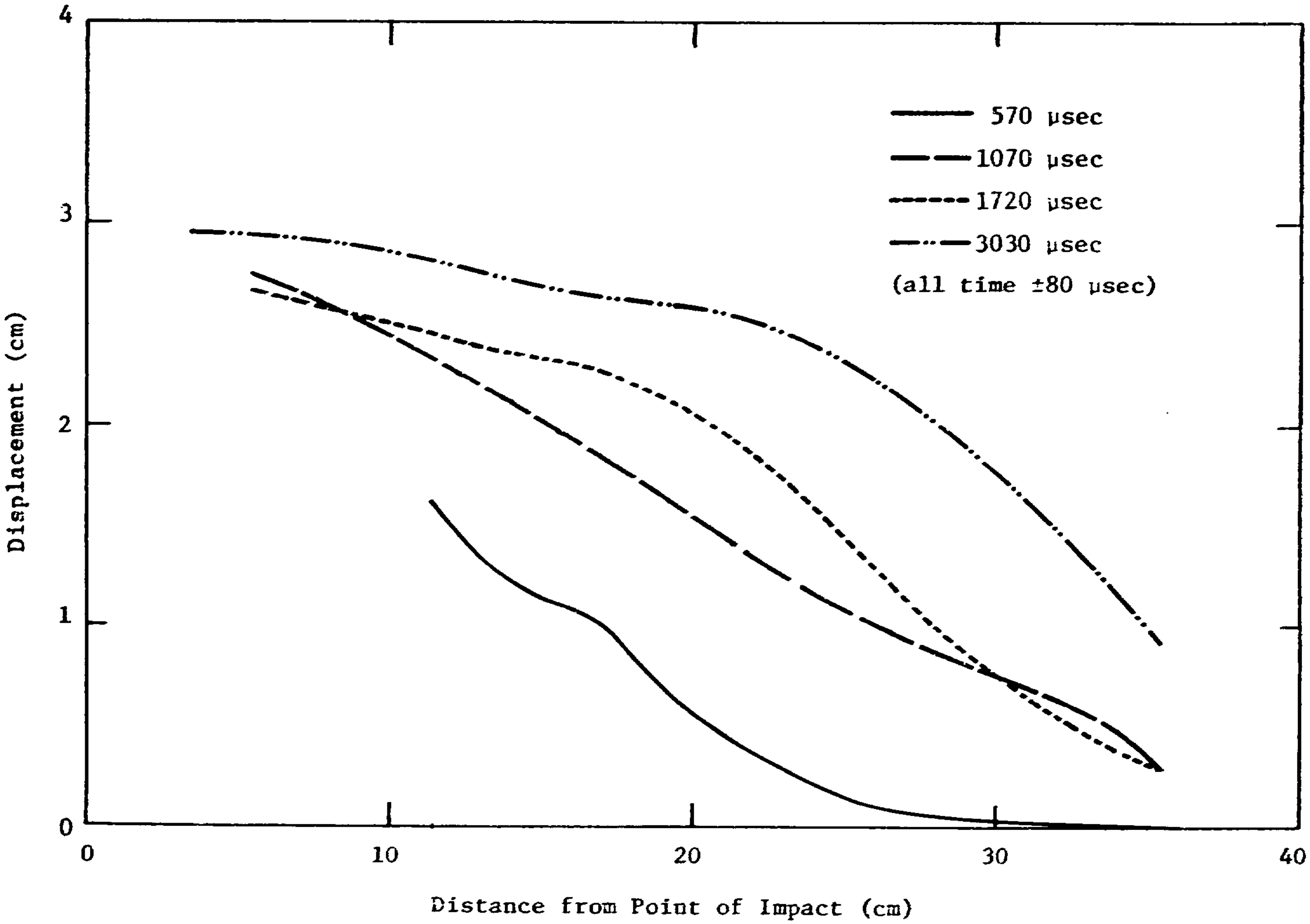

Figure A-12. Experimental Displacement Profiles Measured Along a Vertical Line through the Impact Point. UDRI Test FT5B: 1.11-cm Dia Steel Sphere Impacting at 1550 m/sec

to within ±80 μsec, so there is also a ±80 μsec time uncertainty associated with each profile. The displacements in the vertical plane are consistently larger than those in the horizontal plane, a result of the plate geometry and/or some uncertainty in the displacement observations.

Taking these uncertainties into account, Figure A-13 shows that the calculated profile at 600 μsec is quite similar to the observed profiles at 570 ±80 μsec. However, as seen in Figures A-11 and A-12, the observed profile continues to move out after 600 μsec, while the calculated motion (Figures A-8 and A-9) begins to slowly rebound. Assumptions in the calculation, and differences between the experimental and calculated conditions, are responsible for the divergence after 600 μsec:

- The forcing function used in the Phase II response calculation was set to zero after 178 μsec, the end of the Phase I analysis. At later times, therefore, the calculated tensile stresses in the aluminum entrance panel were able to arrest the outward motion of the panel and turn it around more quickly than in the experimental case. While the calculated pressures at the surface of the water had dropped to the 1 bar (~ 15 psi) level or less by 178 μsec, the water was still moving outward. The entrance panel in the tests absorbed this momentum, thereby reaching larger displacements before rebounding.

- The calculations treated the panel as a flat circular disc, rigidly clamped at the outer edge. The experiment used a trapezoidal entrance panel with edges attached by bolts to the side walls of the tank. This attachment presumably strongly restrains edge motion *mormal* to the front pancl surface, but may only weakly restrain rotations of the the edge or motions in the plane of the entrance panel (i.e., "radial" motions). This relatively weak boundary constraint would allow larger displacements in the

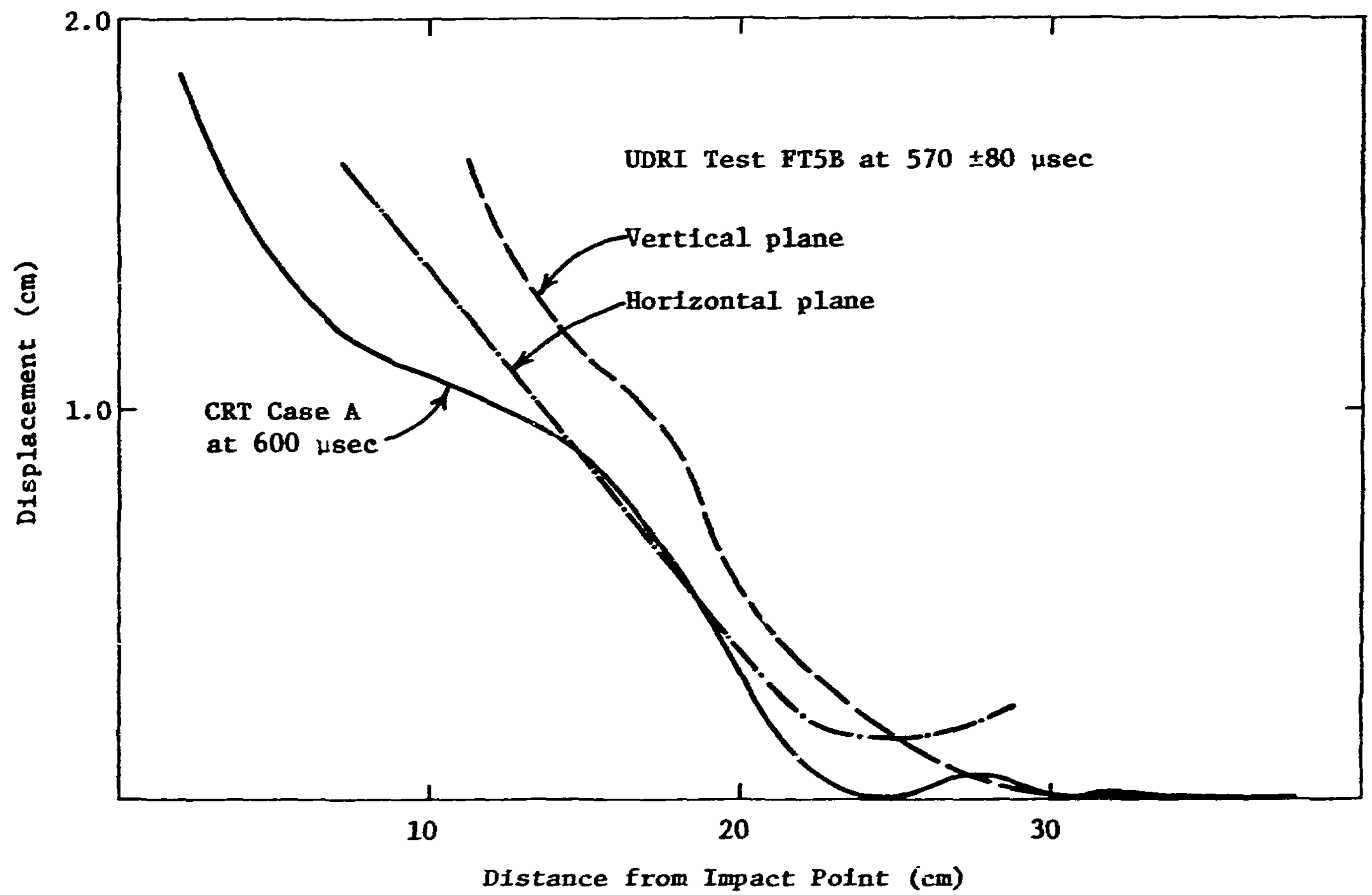

Figure A-13. Comparison of Calculated and Measured Displacement Profiles of Entrance Panel Approximately 600 µsec After Impact at 1550 m/sec by a 1.11-cm Dia Steel Sphere

test case. For example, based on large deflection plate theory[4], the maximum displacement would be expected to increase by at least a factor of two if the boundary is allowed to move freely in the radial direction. The actual boundary conditions on the test panel were somewhere between the extreme of the immovable boundary assumed in the calculation and a boundary allowing free rotation and radial motion. The effect of the geometry and boundary restraint is further seen in a static solution of the plate deflection in which the 0.5 psi hydrostatic load produced by the water head at the level of the impact point was uniformly applied to the radially-restrained disc. This solution produced a 0.5-cm maximum deflection in the plate. By contrast, the maximum static deflection of the test plate, as measured by UDRI with Moire finge shifts, was about 1 cm, indicating that the trapezoidal shape and the relatively weaker radial restraint in the test allows significantly larger deflections.

The entrance panel in UDRI Test FT5B showed permanent distortion, but radial cracks did not propagate outward from the entrance hole. This appears consistent with the hoop stresses calculated in CRT Case A. The plots in Figure A-10 show that calculated tensile hoop stresses exceeded the nominal ultimate strength of 2024-T3 only near the entrance hole.

---

[4] S. Timoshenko and S. Woinowsky-Krieger, "Theory of Plates and Shells," 2nd Edition, p. 404-415, McGraw-Hill, New York, N. Y., 1959.

A.2.2 CRT Case B: Impact of 1.11-cm dia Steel Sphere at 1550 m/sec into Tank with 0.16-cm Aluminum Wall Backed by 3.8-cm of Foam

This case was identical to CRT Case A except for the inclusion of a 3.8-cm layer of AVCO ballistic foam placed directly behind the entrance panel. This foam has a crushing strength of about 25 psi.

The AFTON finite difference calculation was begun with the steel sphere at the foam-water interface (i.e., it was assumed that no energy or momentum was lost in passing through the foam). The inertial mass of the aluminum entrance panel was added to the outermost foam zone. At a time of 77 μsec, Figure A-14, the flow field in the water is quite similar to that in Case A (Figure A-4). The entrance panel, being separated from the water by the foam, has not yet felt any significant pressure and has not moved.

By 174 μsec, the maximum pressure on the aluminum is 30 psi and only the foam out to 8-cm radius has experienced pressures sufficient to cause any crushing (i.e. $P > 25$ psi). In Figure A-14, the velocities of the water near the entrance are such that the water appears to be cutting through the first few centimeters of foam. This is consistent with the observation in UDRI Test FT26B that about 1-cm of foam has been chipped away from around the impact hole.

The much lower pressures generated along the foam-backed plate surface in CRT Case B, as compared with the pressure on the bare plate in CRT Case A, will clearly produce lower displacements and stresses in the aluminum. Since the calculation of the no-foam case (Case A) showed only a minimal chance of crack formation around the entry hole, and since examination of the post-test entrance panel from the corresponding UDRI Tests (FT26 and FT26A) showed no measurable permanent distortion (other than the entry hole), it was decided that a Phase II NONSAP calculation of Case B would not be useful.

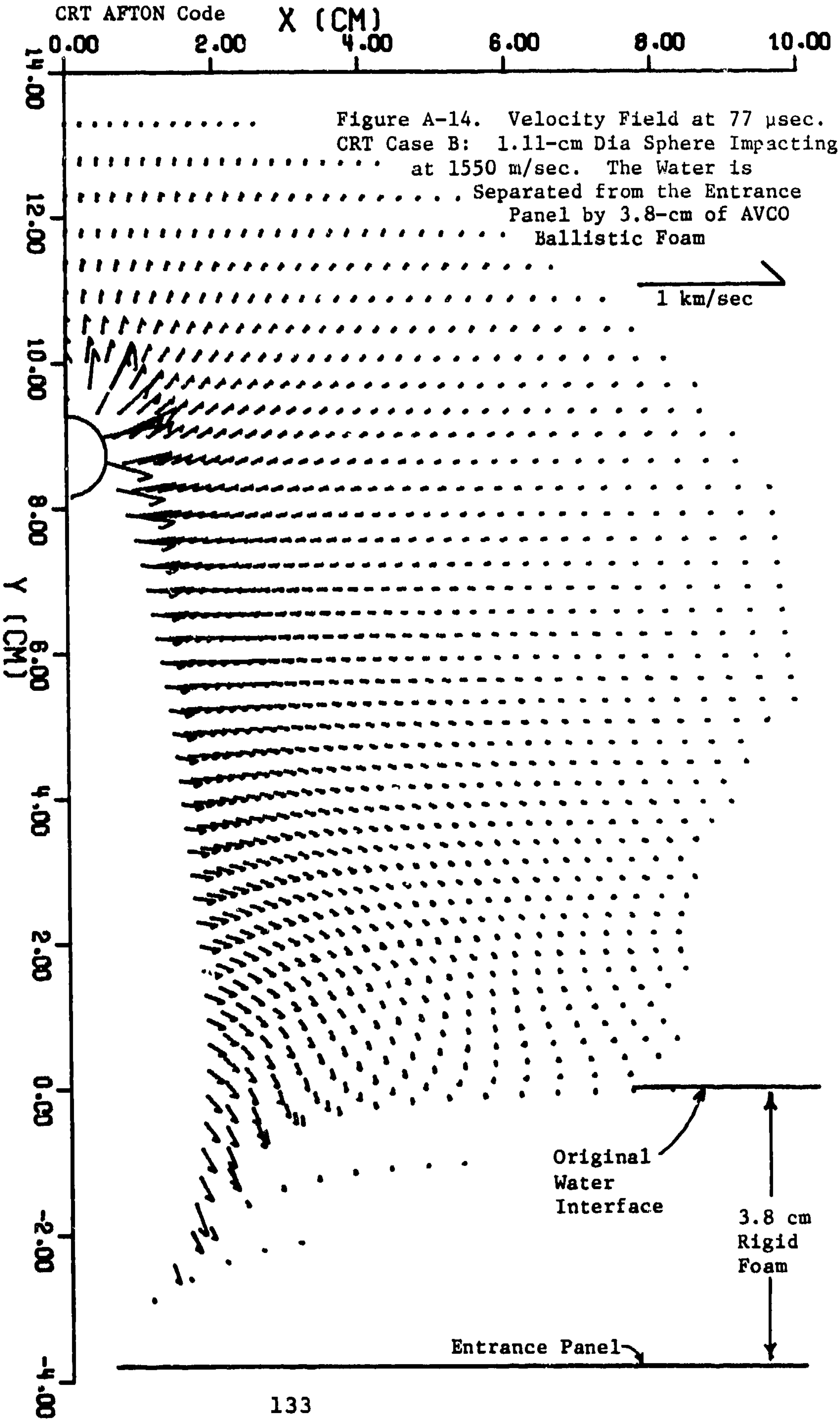

Figure A-14. Velocity Field at 77 μsec. CRT Case B: 1.11-cm Dia Sphere Impacting at 1550 m/sec. The Water is Separated from the Entrance Panel by 3.8-cm of AVCO Ballistic Foam

A.2.3 CRT Case C: Impact of 1.43-cm dia Steel Sphere at 1550 m/sec into Tank with 0.16-cm Aluminum Wall

A.2.3.1 Calculations

The conditions for this case are identical to CRT Case A except that the impacting sphere diameter is 1.43-cm instead of 1.11-cm. *If the thickness of the entrance panel is disregarded,* the penetration dynamics in Case C are seen to be identical to those in Case A at linearly scaled times and dimensions. The scale factor is the ratio of the diameter of the spheres, i.e., 1.43/1.11 = 1.29. Thus, for example, the pressure and particle velocity at 2-cm depth at 10 μsec, as calculated for the CRT Case A conditions, would be the same as those found in the Case C impact at 2.6-cm depth at 12.9 μsec.

These considerations suggest that it may be possible to use scaled results of Phase I penetration analyses obtained for one size fragment or sphere to drive Phase II tank wall response analyses for other size fragments or spheres. This approach could be attractive for future design studies, so it was evaluated here by making two analyses of Case C. In the first, which will be referred to as CRT Case C-1, appropriately scaled Phase I penetration and entrance panel loading results from the CRT Case A calculation were used to drive the Phase II NONSAP analysis of the entrance panel response to the larger sphere impact. In the second analysis, referred to as CRT Case C-2, an AFTON Phase I analysis of the penetration of the 1.43-cm dia sphere was obtained (using the correct inertial mass for the 0.16-cm thick aluminum entrance panel). The validity of the scaled-loading approach used in Case C-1 can be evaluated by comparing the results of C-1 and C-2.

a. Case C-1: Analysis Using Scaled Loading

The entrance panel thickness is the same in CRT Cases A and C, while the sphere diameter increases from 1.11 to 1.43-cm. The relatively thinner plate (with respect to the sphere diameter) in Case C thus provides less inertial confinement to the water during the penetration. As a

consequence, the scaled-loading approach results in some over-loading of the plate in Case C-1.

Displacement profiles obtained at 200 μsec intervals from the NONSAP analysis of the entrance plate response are shown in Figure A-15. These have the same general shape as those for the smaller sphere in Case A, (Figure A-8) but displacements are consistently 50% greater in magnitude; 3.5 vs 2.25-cm on axis, 1.5 vs 1.0-cm at 15-cm off axis, etc. Similarly stress profiles (Figure A-16) shows consistently higher stresses relative to those at 200 μsec, for example, about 2.5 times as much area of the front panel (5.75 vs 3.75-cm in radius) was stressed by hoop tension greater than the nominal 70 kpsi tensile limit of the 2024-T3 aluminum than in the previous case (Figure A-12). Also, at 400 μsec the hoop stress level i. still just below the tensile strength as far out as 10-cm radius, which shows a greater tendency for crack propagation than the previous case. Perhaps the most definitive change occurs in the hoop strain. As shown in Figure A-17, the strains produced at 200 μsec by the scaled forces in Case C-1 are considerably larger than those in Case A. In the first calculation the strain drops rapidly from a peak of 9% to under 2% at 1.2-cm and is less than 0.5% by 3.5-cm while the larger sphere produced a peak strain over 13% and the 2% and 0.5% levels occur at almost 3 and 7-cm respectively. Thus at least six times as much material underwent hoop strains of 2% or more in the scaled calculation, a difference great enough to provide a potential failure criterion.

b. Case C-2: Analysis Using Loading Calculated for 1.43-cm dia Steel Sphere Impact

A Phase I AFTON code analysis was made of a 1.43-cm dia steel sphere impact at 1500 m/sec. (This slightly lower impact velocity corresponds more closely with conditions of UDRI Test FTA9, which will be used for comparison later.) Comparisons of peak pressure, Figure A-18a, and the specific impulse up to 130 μsec, Figure A-18b, for Cases A, C-1, and C-2 indicate

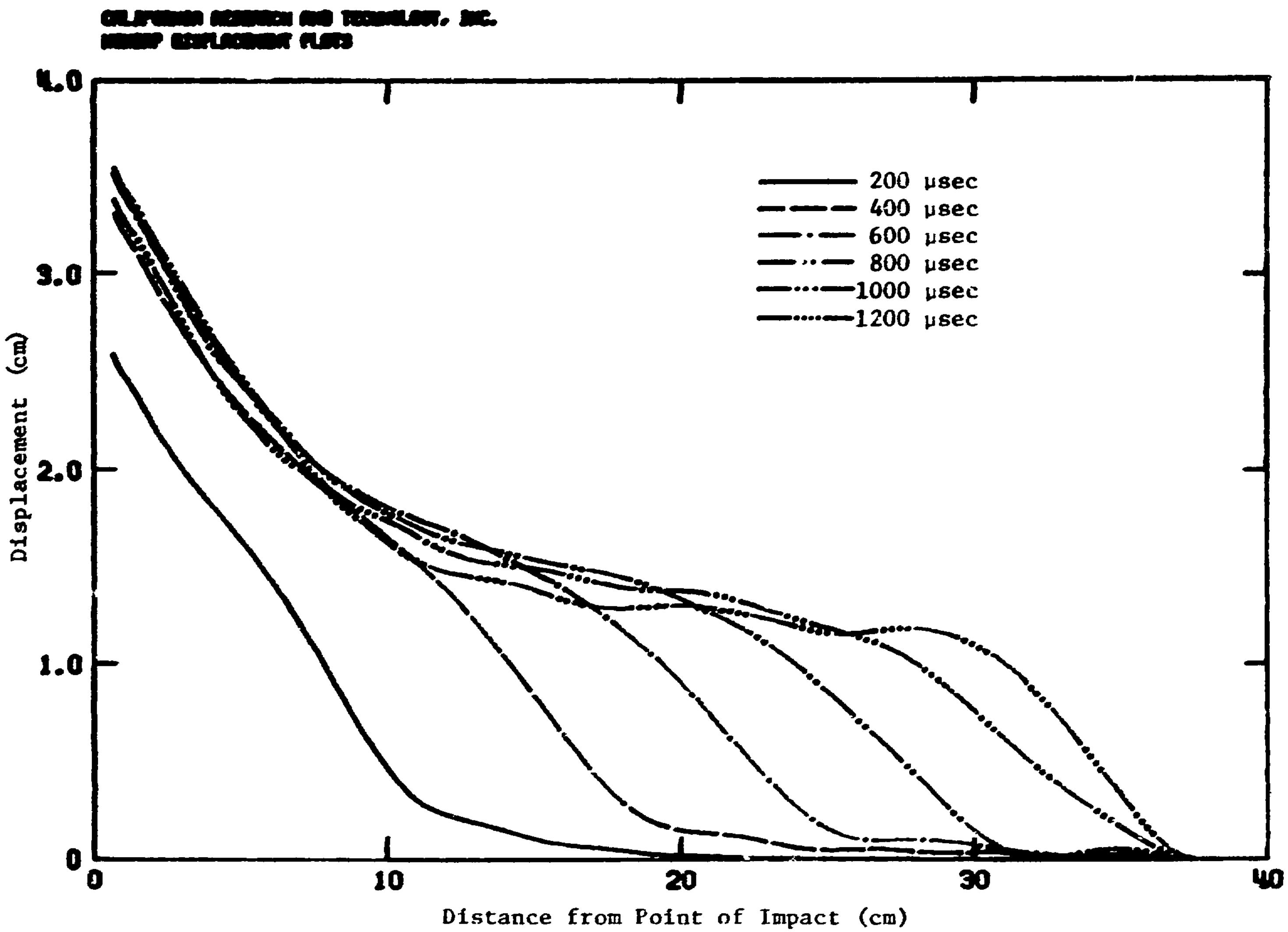

Figure A-15. Calculated Displacement Profiles along the 0.16-cm Aluminum Entrance Panel at Sequence of Times Between 200 and 1200 μsec After Impact. CRT Case C-1: 1.43-cm Dia Steel Sphere Impacting at 1550 m/sec (Loading of Panel Obtained by Scaling Results of Penetration Analysis of 1.11-cm Dia Sphere Impact from CRT Case A)

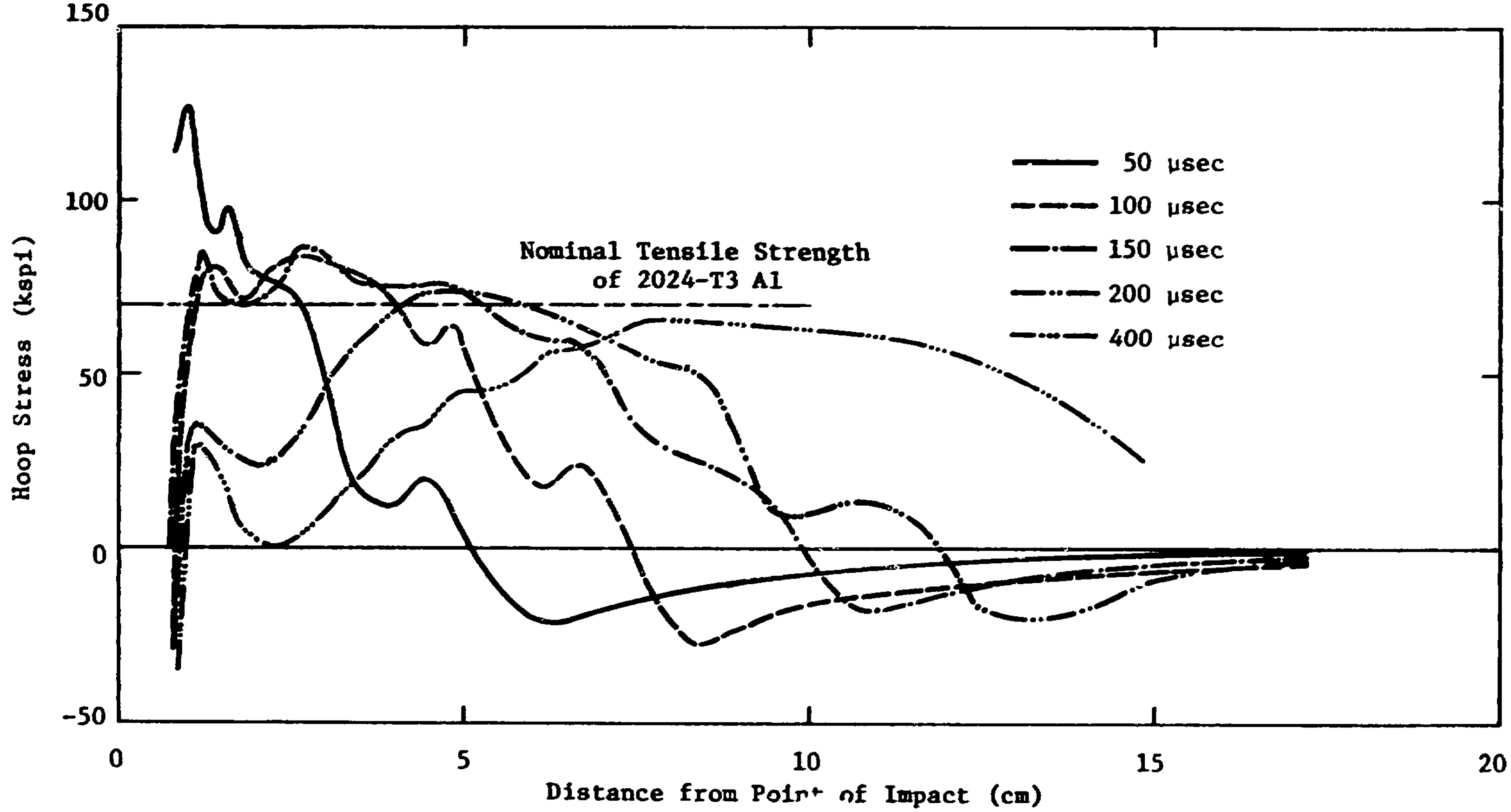

Figure A-16. Hoop Stress (Tension Positive) vs Distance along the Entrance Panel from Impact Point. CRT Case C-1: 1.43-cm Dia Steel Sphere Impacting at 1550 m/sec

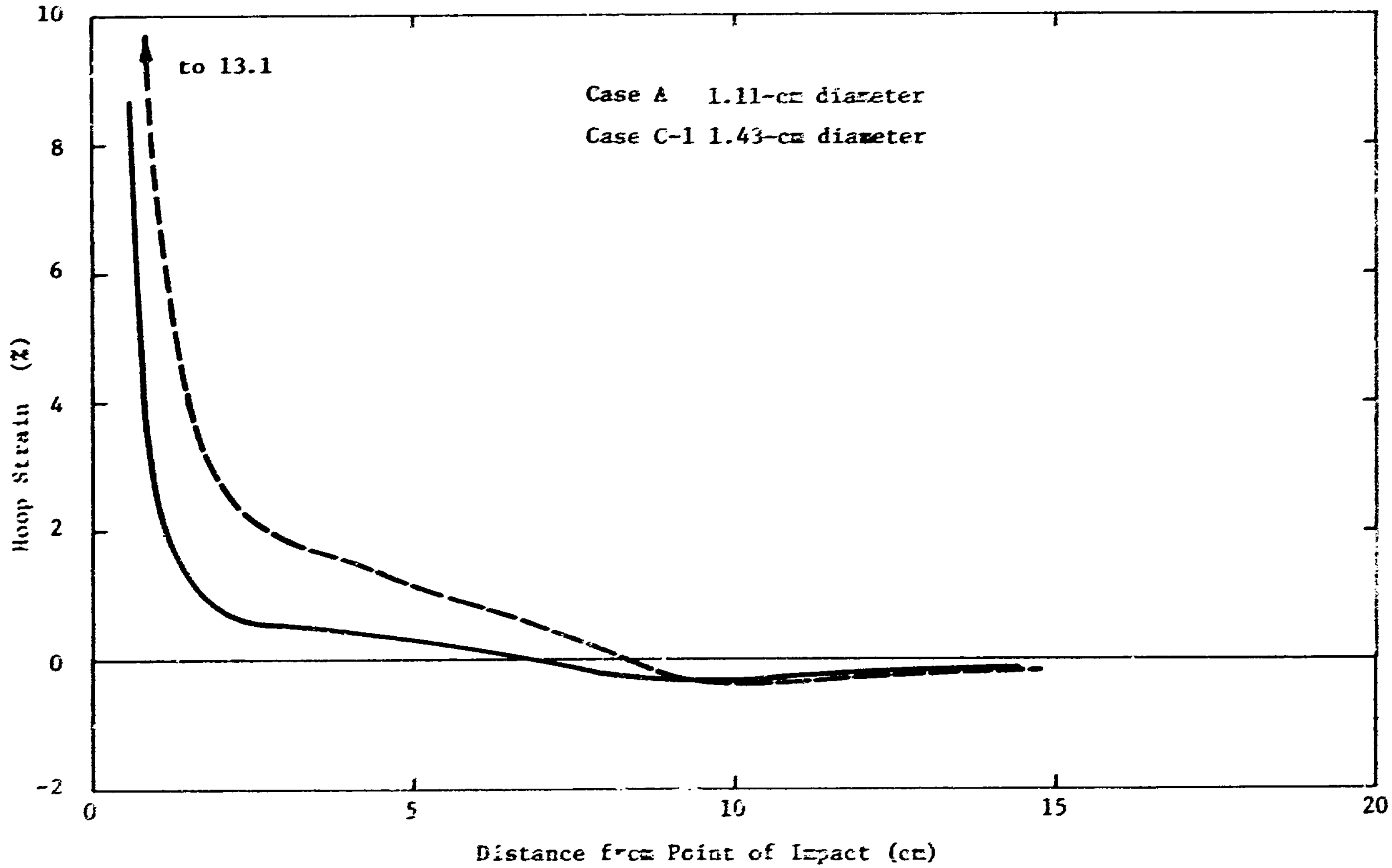

Figure A-17. Hoop Strain at 200 μsec vs Distance along Front Panel for 1.11-cm (Case A) and 1.43-cm (Case C-1) Dia Steel Spheres Impacting at 1550 m/sec

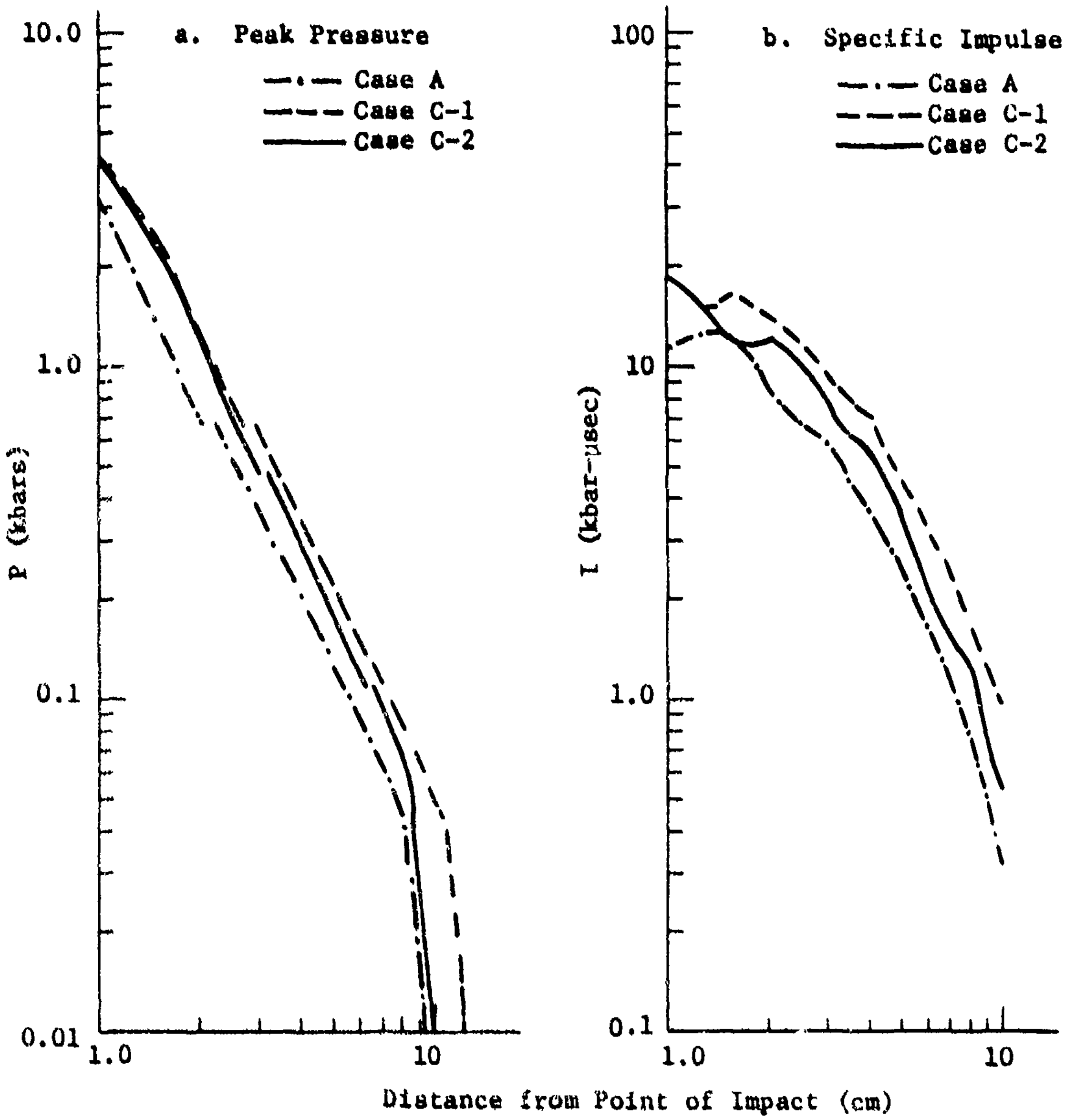

Figure A-18. Peak Pressure and Specific Impulse to 130 μsec along the Entrance Panel Calculated by the AFTON Code for CRT Cases: A (1.11-cm Dia Sphere), C-1 (Time and Distance in Case A Scaled by 1.43/1.11), and C-2 (1.43-cm Dia Sphere)

that simple scaling of the forces from the AFTON calculation in Case A provided a reasonable approximation to the actual forces calculated in Case C-2. Initially, the cavity behind the penetrator appears to be the primary source of relief waves. The scaled peak pressure lies along that calculated for the 1.43-cm diameter sphere, while the scaled integrated specific impulse is about 20% higher. At distances large relative to the size of the penetrator (about 8-cm) the relief from the entrance wall dominates the attenuation and the peak pressure is almost the same for both spheres. Similarly the difference between the scaled and actual impulses grows with range so that at 10-cm the scaled value is almost a factor of two too high. Since the stresses and strains leading to fracture occur early in time and close to the entrance hole, results of Case C-1 are probably adequate to describe the response to the 1.43-cm sphere. The calculated displacements, however, are a result of long time and large range pressures, and are probably higher than would be expected from the C-2 forces.

A.2.3.2 Experimental Comparison

Observations of entrance panel dynamic deformation for conditions corresponding to CRT Case C were not obtained in the UDRI test series. However, measurements were made in UDRI Test FTA9 of the displacement of the sphere vs time. Figure A-19 compares the measured displacements (which were obtained to about 55 μsec), with the displacements calculated in CRT Case C-2. Excellent agreement is seen; the slight offset in time is probably due to the difficulty in establishing the exact zero time by forward extrapolation of the experimental data.

Shock front arrival times at increasing radii along the entrance panel were also measured in UDRI Test FTA9. These are compared in Figure A-20 with the times at which peak pressures occured, as calculated in CRT Case C-2. The length of the vertical bar associated with each calculated peak corresponds to the width of the corresponding zone and is a measure of the

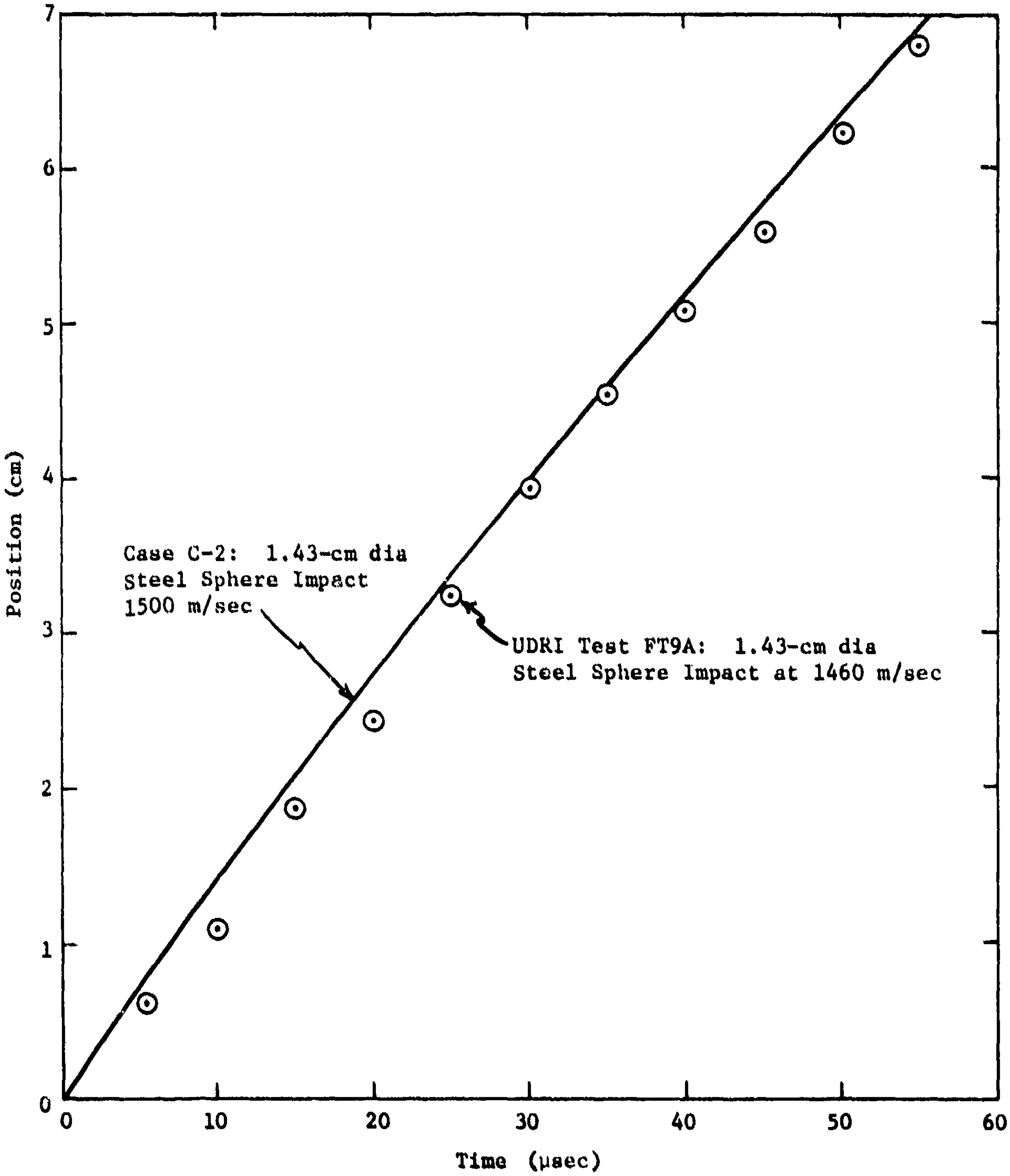

Figure A-19. Experimental and Calculated Position of Projectile vs Time

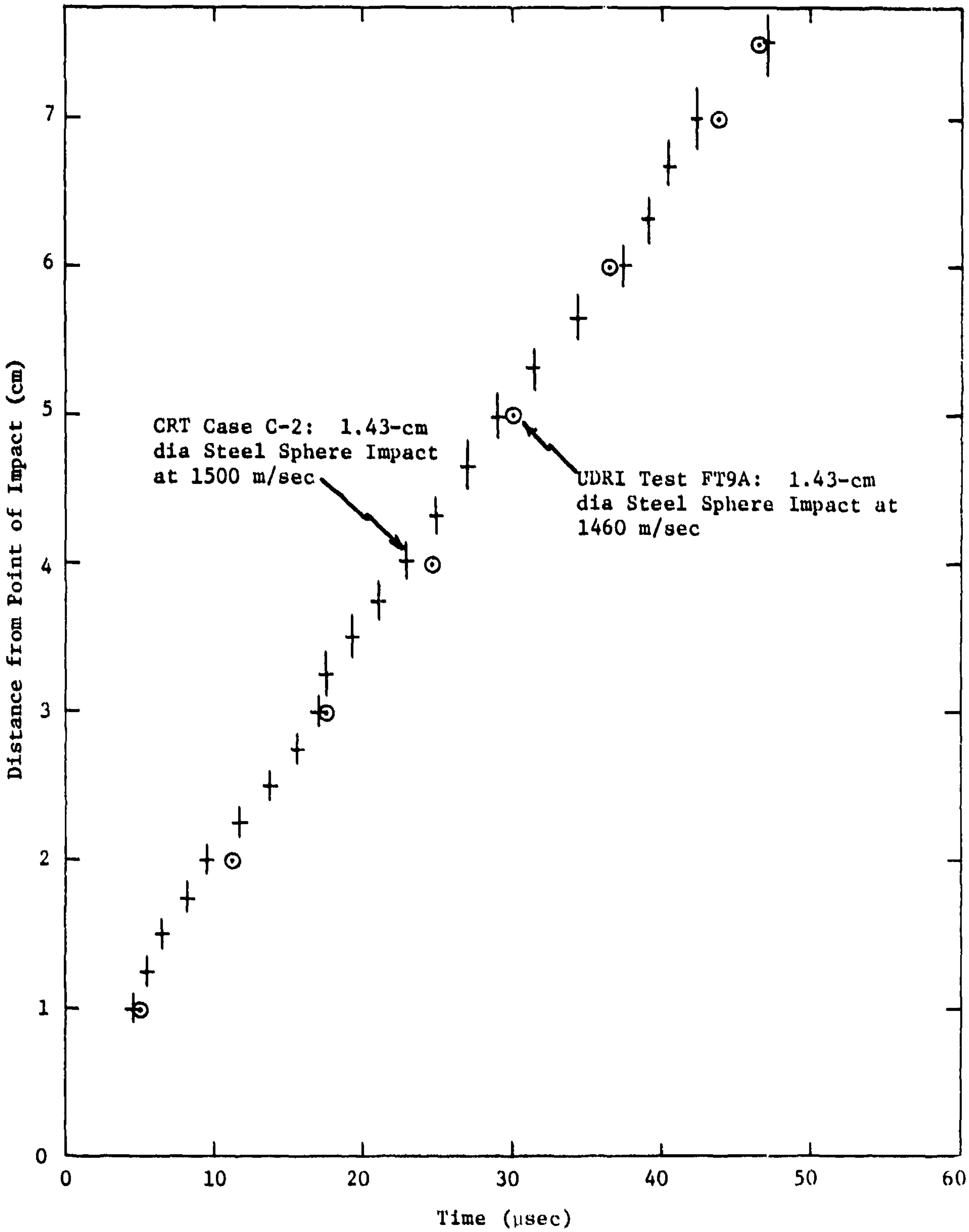

Figure A-20. Arrival Time of Experimental Shock Front and Calculated Peak Pressure along Entrance Panel

uncertainty in position. Again the agreement is seen to be excellent. Since shock velocity and hence displacement of the shock front along the front panel is a function of pressure, this agreement indicates that the calculated peak pressures are correct.

A.3 SUMMARY AND CONCLUSIONS

1. A two-pha e numerical technique for predicting penetration and response of fuel tanks impacted by high velocity fragments has been demonstrated and correlated with available experimental observations. Phase I of the method uses an adaptation of the AFTON 2-D finite differenc code to analyze penetration dynamics and to determine the time-resolved pressure applied by the fuel along the entrance panel. Phase II uses this information to drive a NONSAP 2-D finite element code analysis of the entrance panel dynamic response (deformation).

2. Using this method, calculations have been made of steel sphere impacts at ∿1500 m/sec into tanks containing water. Results of the calculations were compared with UDRI experimental observations of projectile displacement history within the water, shock arrival time in the water along the water-entrance panel interface, and entrance panel displacement profiles. Excellent agreement was obtained between the calculated and experimental projectile motions, as well as the shock arrival times. Comparisons of entrance panel deflection profiles are generally good at early times, but the measured profiles eventually show larger displacements than the calculated profiles. This reflects differences in boundary conditions between the tests and calculations, as well as the fact that the penetration analysis (Phase I) was not continued far enough. (This is not a limitation of the technique; AFTON solutions of penetration could be extended in future analyses if desired.)

3. Catastrophic failure of entrance panels occurs by propagation of radial cracks emanating from the impact hole. The calculations show that peak tensile hoop stresses and strains, which would lead to such rupture, develop in the region around the impact hole well *after* the impact, but well *before* most of the panel responds to the impact. In the problems considered in the current program (1.11-cm and 1.43-cm

dia sphere impacts at ~1500 m/sec), these peak stresses developed within 200 μsec of the impact.

4. Use of foam backing on the entrance panel greatly reduces the transient pressures applied by the water to the entrance panel.

A.4 RECOMMENDATIONS

This numerical approach should be used to analyze interactions and mechanisms which are difficult to identify or observe experimentally, and which may be important in developing tank designs which are more resistant to impact damage.

An important example would be to use numerical solutions to systematically examine the effects of foam-backing parameters on entrance panel response. Foam backing is clearly very effective in reducing damage, but its use reduces the available tank volume. For this reason, it is highly desirable to optimize the foam system by choosing the best combination of foam thickness, foam crushing strength and foam density. Systems in which foam or honeycomb are sandwiched between layers of aluminum (or other materials) also can be evaluated and optimized in this manner.

APPENDIX B

This Appendix provides a listing of the changes made to the FDC and the listing for the shock propagation code. None of the changes in the FDC affected the way the code calculates pressure. They were made to adapt the code to the UDRI tank boundary conditions, and to provide output in the format required for the BR-1A(HR) code.

```
            X1(JJ)=XP(JJ,1)
            Y1(JJ)=XP(JJ,2)
            Z1(JJ)=XP(JJ,3)
   84       CONTINUE
            PRINT*, "ASIGN VALUES MODIFIED FOR UDRI TANK"
            PRINT*, "I, X0,Y0,Z0   X1,Y1,Z1,  ASIGN "
            ASIGN(1)=0.
            ASIGN(2)=1.
            ASIGN(3)=-1.
            ASIGN(4)=0.
            ASIGN(5)=1.
            ASIGN(6)=-1.
            ASIGN(7)=0.
            ASIGN(8)=-1.
            ASIGN(9)=1.
            ASIGN(10)=0.
            ASIGN(11)=1.
            ASIGN(12)=-1.
            ASIGN(13)=0.
            ASIGN(14)=1.
            ASIGN(15)=-1.
            ASIGN(16)=0.
            ASIGN(17)=-1.
            ASIGN(18)=1.
            ASIGN(19)=0.
            ASIGN(20)=-1.
            ASIGN(21)=1.
            ASIGN(22)=0.
            ASIGN(23)=-1.
            ASIGN(24)=1.
            ASIGN(25)=0.
            ASIGN(26)=1.
            ASIGN(27)=-1.
            DO 85 ISD=1,I
            WRITE (6,86) ISD,X0(ISD),Y0(ISD),Z0(ISD),X1(ISD),Y1(ISD),Z
           1ASIGN(ISD)
   85       CONTINUE
   86       FORMAT (I5,3X,3F10.5,3X,3F10.5,3X,F10.5)
            RETURN
            END
```

Figure B-1. Listing of modified portions of subroutine IMAGES.

```
      PROGRAM HRAM (INPUT,OUTPUT,TAPE5=INPUT,TAPE6=OUTPUT,TAPE7)
      DIMENSION A(3,300)
      DIMENSION KPT(6),KT(6)
      COMMON/PLOT/ASIGN(300),X0(300),Y0(300),Z0(300),X1(300),Y1(300),Z1(
     1300),NS,DT,TMAX,NP,XW(300,3),PRF1(50,100),IFIRST(50)
      COMMON /LABEL/ KJOB,NJOB
      COMMON/IDINFO/ID(6)
      READ(5,1000) NJOB
      DO 1 KK=1,NJOB
      KJOB = KK
      READ(5,2001)NP
      READ(5,3001)TMAX,DT,IPLOT
 3001 FORMAT(2F10.5,I1)
      DO2I=1,NP
      READ(5,1001)(XW(I,J),J=1,3)
    2 CONTINUE
 1001 FORMAT(3F10.5)
 2001 FORMAT(I3)
 1000 FORMAT(I1)
      CALL IMAGE(NS)
      CALL TRAJ(A,B,DX,XE,NE,C,DENS,JXE,JMAX)
      CALL MIRROR(A,B,DX,XE,NE,C,DENS,JXE,JMAX)
    1 CONTINUE
      PRINT*, "DATA TO PUNCH"
      ITMAX= TMAX*10. + .00001
      DO 11 ITIME = 1,ITMAX
       ICOUNT = 0
      DO 15 IPOINT=1,NP
      IF ( IFIRST(IPOINT) .LT. ITIME )  ICOUNT = ICOUNT + 1
   15 CONTINUE
      TIME = ITIME*10
      WRITE(7,10) TIME,ICOUNT
      WRITE(6,14) TIME,ICOUNT,ITIME
   10 FORMAT(F10.4,I5)
   14 FORMAT(1X,F10.4,I5,30X,I5)
      K = 0
      L=0
      IF (ICOUNT.EQ.0) GOTO 32
      IFLAG=0
      DO 36 INDEX=1,6
      KPT(INDEX) = 0
      KT(INDEX) = 0
   36 CONTINUE
      DO 20 IPOINT = 1,NP
      IF (IFLAG.EQ.1 .AND. IPOINT.EQ.NP .AND. IFIRST(IPOINT).GE.ITIME)
     1    GOTO 21
      IF (IFIRST(IPOINT) .GE. ITIME) GO TO 19
      IF (L.EQ.0 .OR. L.EQ.6 .OR. L.EQ.12 .OR. L.EQ.18 .OR. L.EQ.24
     1     .OR. L.EQ.30 .OR. L.EQ.36 .OR. L.EQ.42 .OR. L.EQ.48
     2     ) K = 0
      IFLAG = 1
      L = L + 1
      K = K + 1
      KPT(K) = IPOINT
      KT(K) = ITIME
      IF ( K .EQ. 6 ) GO TO 21
      IF (IPOINT.EQ.NP) GOTO 21
```

Figure B-2. Listing of modified portions of program HRAM and MIRROR.

```
            GO TO 19
   21       CONTINUE
            KPT1 = KPT(1)
            KPT2 = KPT(2)
            KPT3 = KPT(3)
            KPT4 = KPT(4)
            KPT5 = KPT(5)
            KPT6 = KPT(6)
            KT1  = KT(1)
            KT2  = KT(2)
            KT3  = KT(3)
            KT4  = KT(4)
            KT5  = KT(5)
            KT6  = KT(6)
            WRITE (7,13) KPT1,PRR1(KPT1,KT1), KPT2,PRR1(KPT2,KT2),
           1     KPT3,PRR1(KPT3,KT3), KPT4,PRR1(KPT4,KT4),
           2     KPT5,PRR1(KPT5,KT5), KPT6,PRR1(KPT6,KT6)
            WRITE(6,13) KPT1,PRR1(KPT1,KT1), KPT2,PRR1(KPT2,KT2),
           1    KPT3,PRR1(KPT3,KT3), KPT4,PRR1(KPT4,KT4),
           2     KPT5,PRR1(KPT5,KT5), KPT6,PRR1(KPT6,KT6)
            K = 0
   13       FORMAT(6(I4,F9.0))
            IFLAG = 0
            DO 34 INDEX=1,6
            KPT(INDEX) = 0
            KT(INDEX) = 0
   34       CONTINUE
   19       CONTINUE
  C         WRITE (6,30) IFIRST(IPOINT), ITIME, K, L
  30        FORMAT (50X,4I5)
   29       CONTINUE
  32        CONTINUE
  11        CONTINUE
   5        CONTINUE
   6        FORMAT(I4,7F10.4)
            WRITE(6,7) NS
   7        FORMAT(//,"NS IS",I4)
  8         FORMAT (1H1)
            CALL EXIT
            END
```

Figure B-2 (Cont'd). Listing of modified portions of program HRAM and MIRROR.

```
      IF(L(K).EQ.0) GO TO 5
      IF(L(K).GT.JMAX) GO TO 6
      IF(NI.EQ.0) GO TO 4
      IF(L(K).LE.JX1) GO TO 4
      V=0.
      XX=X1
      AM=0.
    4 CONTINUE
      R=(X(K)-XX)**2+W(K)**2
      R=SQRT(R)
      DTDX=1./(1.-V/C*(X(K)-XX)/R)
      DLX1=(AM-3.*B/C)*V*DTDX/R**3
      DLW1=DLX1
      DLX1=DLX1*(X(K)-XX)-B*(1./R-1./RL(K))
      DLW1=DLW1*W(K)+B/W(K)*((X(K)-XX)/R-X(K)/RL(K))
      X(K)=X(K)+.5*(DLX1+DLX2(K))*DT
      W(K)=W(K)+.5*(DLW1+DLW2(K))*DT
      DLX2(K)=DLX1
      DLW2(K)=DLW1
      UU=B*AM*V/C*DTDX/R**2
      UXX=UU*(X(K)-XX)+B*DX(K)
      UW=UU*W(K)+B*DW(K)
      UX=UW/W(K)*(XP    -XI(K))+UXX/R1(K)*(X1(K)-X0(K)) * .5
      UY=UW/W(K)*(YP    -YI(K))+UXX/R1(K)*(Y1(K)-Y0(K)) * .5
      UZ=UW/W(K)*(ZP    -ZI(K))+UXX/R1(K)*(Z1(K)-Z0(K)) * .5
      PPHI=B*AM/C*V*DTDX-B*B*ALOG((X(K)+RL(K))/(X(K)-XX+R))
      PPHI = PPHI * .5
      SUMUX=SUMUX+UX*ASIGN(K)
      SUMUY=SUMUY+UY*ASIGN(K)
      SUMUZ=SUMUZ+UZ*ASIGN(K)
      SPPHI=SPPHI+PPHI*ASIGN(K)
    5 CONTINUE
      UX=SUMUX/.012
      UY=SUMUY/.012
      UZ=SUMUZ/.012
      PPHI=SPPHI*DENS
      U2=UX*UX+UY*UY+UZ*UZ
      P=PPHI-.5*DENS*U2*.00144
      INN=INN+1
      TTS(INN)=T
      PTS(INN)=P
      U=SQRT(U2)
      WRITE (6,100A)  T,P,PPHI,U,UX,UY,UZ
 100A FORMAT(6X,9F11.3)
C
      ITIM  = T*100. + 0.0001
      IF ( ABS(P) .LT. 0.01) IFIRST(JK)=ITIME
      IF (ITIM .GT.100) PRINT*, "ITIME ERROR"
      IF (ITIM .GT.100) GOTO 71
      PRS1(JK,ITIM) = 2.0*P
      IF ( PRS1(JK,ITIME) .LT. 0. )   PRS1(JK,ITIME) = 0.0
   71 CONTINUE
C
      NPAGE=NPAGE+1
      IF(NPAGE.LT.40) GO TO 7
      WRITE(6,2007)
      NPAGE=0
```

Figure B-2 (Cont'd). Listing of modified portions of program HRAM and MIRROR.

```
001
032
0.75       4.01
31.90      1.73       0.02
30.65      3.48       0.02
31.33      6.67       0.02
30.40      9.23       0.02
30.90      11.20      0.02
30.23      12.20      0.02
30.56      14.20      0.02
29.43      15.73      0.02
27.93      24.57      0.02
27.30      23.40      0.02
27.23      2.6        0.02
27.23      7.7        0.02
27.23      11.7       0.02
26.40      14.20      0.02
23.40      15.20      0.02
25.73      17.97      0.02
26.43      22.87      0.02
26.16      24.30      0.02
22.23      2.6        0.02
22.23      7.7        0.02
22.23      11.7       0.02
22.23      14.7       0.02
22.23      19.7       0.02
22.23      23.7       0.02
22.23      28.7       0.02
18.23      2.6        0.02
18.23      7.7        0.02
18.23      11.7       0.02
18.23      14.7       0.02
18.23      19.7       0.02
19.23      24.7       0.02
19.23      28.7       0.02
 1 1 1 1 1 133.46       31.42      38.59
16.73      13.19      0.0
16.73      13.19      [illegible]
.0123.0123.0010.15  0.15  0.15  0.15  0.15  0.15
0.356 0.356 0.356 0.356 0.0011.356
0.036      14.7       0.0        5010.0     0.436
4068.0     0.5
0          0.0        30.        30.        30.
0          0.0
           30.
   3.0     1.0     3.0      0       0
```

Figure B-3. Input data for simulation of shot FT5 (or FT5B) by FTC.

```
 10   CONTINUE
*     CALL OUTPUT
*     PRINT 100,U,TH,P2,P21,P22,P3,P4,QP2,RH,DRH
100   FORMAT(1H1,T15"U"T35"TH"T55"P2"T75"P21"T95"P22"/
     *     T10,E14.8,T30,E14.6,T50,E14.8,T70,E14.8,T90,E14.8/1H0
     *     T15"P3"T35"P4"T55"QP2"T75"RH"T95"DRH"/
     *     T10,E14.8,T30,E14.8,T50,E14.8,T70,E14.8,T90,E14.8)
*     PRINT 101,DUT,DDRH
101   FORMAT (1H0,T15"DUT"T35"DDRH"/
     *   T10,E14.8,T30,E14.8)
      KNT = 0
      IF ( KOUNT .EQ. 1 )    KNT = 1
      IF ( KOUNT .EQ. 5 )    KNT = 2
      IF ( KOUNT .EQ.  8 )   KNT = 3
*     IF ( KNT .GT. 0 )      CALL PICTURE
      CALL PICTURE
      IF ( MS .LT. 1.4 )      GO TO 5
      STOP
      END

      FUNCTION RHO1(A,N)
      COMMON /3/ AINC,BINC
      EXTERNAL MSF
      REAL MSF,N
      A1 = AINC
      B1 = BINC
      B = 1. + 1E-3
 10   C = MSF(B,N)
      D = A - C
      IF ( D .LT. 1E-12  .A. D .GT.  -1E-12 )        GO TO 60
*     PRINT 500, A, B, C, D
500   FORMAT(" A="E12.5"    B="E12.5"    C="E12.5"    D="E12.5)
      IF ( D .LT. 0. )                               GO TO 20
      IF ( D .GE. A1 )                             GO TO 50
      IF ( A1 .GE. 1E-13 )                           GO TO 40
      PRINT 1000, D, A1
      GO TO 60
 20   IF ( B1 .GE. 1E-12 ) GO TO 30
      PRINT 1001, D, B1
      GO TO 60
 30   B = B - B1
      B1 = B1 / 2.
      GO TO 50
 40   A1 = A1 / 2.
 50   B = B + B1
      GO TO 10
 60   CONTINUE
      RHO1 = B
      RETURN
1000  FORMAT (" ERROR RETURN MESSAGE; D = "E12.5" , A1 ="E12.5" RETURNED
     * FROM POINT 1." )
1001  FORMAT (" ERROR RETURN MESSAGE; D = "E12.5" , B1 ="E12.5" RETURNED
     * FROM POINT 2." )
      END
```

Figure B-4. Listing of Shock Propagation Code.

```
      SUBROUTINE SETUP
      COMMON /1/ BETAMS,DRH,TH,BTH,N,MS,P1,BETA,L1,L1P1,R(300),DUT,DDRH
     *    ,KNT
      COMMON /3/  AINC,BINC
      REAL MS,N
*   DATA STARTS IN COLUMNS 15, 25, 35, AND 45.
      DATA     BETA      ,AINC      ,BINC      ,L1        /
     *         -.10988   ,.1        ,.1        ,100       /
      DATA     N         ,MS        /
     *         7.        ,1.        /
*   R(I) HAS L1 VALUES IN THE INTERVAL ( 1, 0 )
*   WANT R(1) TO BE 1.
      L1P1 = L1 + 1
      R(1) = 1.
      DO 10 I = 2, L1
      R(I) = FLOAT(L1P1 - I) / FLOAT(L1)
   10 CONTINUE
      RETURN
      END

  1                FUNCTION U1(X)
                   U1 = 1. - 1./X
                   RETURN
                   END

              REAL FUNCTION MSF ( B, X )
              MSF = ( B**(X+1.) - B ) / ( X*(B-1.) )
              MSF = SQRT(MSF)
              RETURN
              END

              FUNCTION DRHO1(RH)
              COMMON /1/ BETAMS,DRH,TH,BTH,N,MS,P1,BETA,L1,L1P1,R(300),DUT,DDRH
             *    ,KNT
              REAL MS,N
              RHN = RH ** N
              TOP = 2. * N * MS * (RH-1.)**2
              BTM = N * RHN * RH - (N+1.) * RHN + 1.
              DRHO1 = TOP / BTM
              RETURN
              END

              FUNCTION DUTH(RH)
              COMMON /1/ BETAMS,DRH,TH,BTH,N,MS,P1,BETA,L1,L1P1,R(300),DUT,DDRH
             *    ,KNT
              REAL MS,N
              DDRH = DDRHO1(RH)
              DUTH = MS * (DDRH - (DRH*DRH)/RH ) + DRH
              DUTH = DUTH * (BETA/RH)
              RETURN
              END
```

Figure B-4 (Cont'd). Listing of Shock Propagation Code.

```
      PROGRAM YKPRESS (INPUT,OUTPUT,PLOT)
      EXTERNAL MSF
      DIMENSION REQ(300),T2B(300),T3B(300),T4B(300)
      COMMON /1/ BETAMS,DRH,TH,BTM,N,MS,P1,BETA,L1,L1P1,R(300),DUT,DDRH
     *   ,KNT
      COMMON /2/ PP(300),PP1(300),PP2(300),T2(300),T21(300),T22(300)
     *     ,T3(300),T4(300)
      DIMENSION XMS(20)
      REAL N,MS,MSF
      DATA XMS/1.053,1.05,1.039,1.029,1.021,1.014,1.013,1.005/
      CALL SETUP
      KOUNT = 0
5     KOUNT = KOUNT + 1
      MS = XMS(KOUNT)
      IF ( MS .EQ. 0. )   STOP"MS = 0."
C     DEFINE THE EXPRESSION FOR T1 ( T1 = P1.
      RH = RHO1(MS,N)
      P1 = U = U1(RH)
      DRH = DRHO1(RH,MS,N)
      TH = BETA * MS * DRH
      TH = TH / (U*RH)
      QP2 = 3.*RH - 1.
C     SOLVE FOR THE TERMS: P2, P3, AND P4 OF EQ. 70
      US = U * U
      UTH = U * TH
      USTH = US * TH
      UBETA = U * BETA
      USTHS = UTH * UTH
      UTHBETA = UTH * BETA
      CONNIE = ( BETA * MS * DRH ) / ( RH * RH )
      P21 = US - U + UBETA
      P22 = P21 + CONNIE
      P2 = P22 + UTH - USTH
      BETAMS = BETA * MS
      DUT = DUTH(RH)
      P3 = UTH + USTHS - 2*USTH - UTHBETA - BETAMS * DUT
      P4 = USTHS
C     FIND THE TERMS T2(I), T3(I), AND T4(I)
      T2A = RH / QP2
      T3A = T2A / QP2
      T4A = T3A / QP2
      DO 10 I = 1, L1
      REQ(I) = R(I) ** QP2
      T2B(I) = 1. - REQ(I)
      X = R(I)
      CHRIS = QP2 * ALOG(X)
      CHRIS = QP2 * ALOG(X) - 1.
      T3B(I) = 1. + REQ(I) * CHRIS
      T4B(I) = 2. - REQ(I) * ( CHRIS * CHRIS + 1. )
      T2(I) = T2A * P2 * T2B(I)
      T21(I) = T2A * P21 * T2B(I)
      T22(I) = T2A * P22 * T2B(I)
      T3(I) = T3A * P3 * T3B(I)
      T4(I) = T4A * P4 * T4B(I)
      PP(I) = P1 + T2(I) - T3(I) + T4(I)
      PP1(I) = P1 + T21(I)
      PP2(I) = P1 + T22(I)
```

Figure B-4 (Cont'd). Listing of Shock Propagation Code.

```
      FUNCTION DDRHO1(RH)
      COMMON /1/ BETAMS,DRH,TH,BTM,N,MS,P1,BETA,L1,L1P1,R(300),DUT,DDRH
     *    ,KNT
      REAL N,MS
      RHM1 = RH - 1.
      RHENM1 = RH ** (N-1.)
      F = N * (RHM1) / BTM
      T1 = 2. * RHM1
      T2 = 4. * MS * DRH
      T3 = (N+1.) * RHENM1 * DRH * DRH
      DDRHO1 = F * ( T1 + T2 - T3 )
      RETURN
      END
      SUBROUTINE OUTPUT
      COMMON /1/ BETAMS,DRH,TH,BTM,N,MS,P1,BETA,L1,L1P1,R(300),DUT,DDRH
     *    ,KNT
      COMMON /2/ PP(300),PP1(300),PP2(300),T2(300),T21(300),T22(300)
     *      ,T3(300),T4(300)
      REAL MS,N
      PRINT 1000
      PRINT 1001, MS, P1
      PRINT 1002
      DO 10 I = 1,L1
      PRINT 1003, PP(I),PP1(I),PP2(I),T2(I),T21(I),T22(I),T3(I),T4(I)
   10 CONTINUE
      RETURN
 1000 FORMAT(1H1," THIS PROGRAM COMPUTES THE SOLUTIONS TO THE EQUATION
     *S: 73, 74, AND 75."/" THESE ARE THE BACH AND LEE COMPLETE SOLUTION
     *, THE STRONG SHOCK SOLUTION OF B&L, AND YURKOVICH'S SOLUTION.")
 1001 FORMAT(1H0," THIS DATA IS COMPUTED FOR SHOCK MACH NUMBER:"F7.3/
     *   1H0,T10"P1 ="E12.5)
 1002 FORMAT(1H0,T7"PP(I)"T24"PP1(I)"T41"PP2(I)"T58"T2(I)"
     *   T75"T21(I)"T92"T22(I)"T109"T3(I)"T126"T4(I)"/1H0)
 1003 FORMAT(T3,E12.5,T20,E12.5,T37,F12.5,T54,E12.5,T71,E12.5
     *   T88,E12.5,T105,E12.5 ,T122,E12.5)
      END
      SUBROUTINE PICTURE
      COMMON /1/ BETAMS,DRH,TH,BTM,N,MS,P1,BETA,L1,L1P1,R(300),DUT,DDRH
     *    ,KNT
      COMMON /2/ PP(300),PP1(300),PP2(300),T2(300),T21(300),T22(300)
     *      ,T3(300),T4(300)
      COMMON / XYZCOM / CMINX,STEPX,CMINZ,STEPZ,FCTR,MODLIN(  1),IFLIP,
     A   IORDER,IPLOT,IPRINT,ISTRIP,MISC(10),LAST,LBLC(5),LBLC1(5),
     B   LBLX(5),LBLY(  1,  3,3),LBLZ(5),MODSYM(  1),MULPLT,
     C   XIN(  1,  3, 100),ZIN(  1,  3, 100),XLGTH,ZLGTH
      MODSYM(1) = -1
      IPRINT = 1
      LBLC(1) = 10H    BETA =
      LBLC(2) = IMAGE(BETA,5)
      LBLC(3) = 10H      MS =
      LBLC(4) = IMAGE(MS,5)
      LBLX(5) = 10H    RADIUS
      LBLZ(1) = 10HPRESSURE
      LBLY(1,1,1) = 10HBACH AND L
      LBLY(1,1,2) = 10HEE
```

Figure B-4 (Cont'd). Listing of Shock Propagation Code.

```
      LBLY(1,2,1) = 10HB AND L
      LBLY(1,2,2) = 10HSTRONG SHO
      LBLY(1,2,3) = 10HCK
      LBLY(1,3,1) = 10HYURKOVICH
      LBLY(1,3,2) = 10HSTRONG SHO
      LBLY(1,3,3) = 10HCK
      MSG = 0
      CALL START
      DO 10 I = 1,L1
      XIN(1,1,I) = XIN(1,2,I) = XIN(1,3,I) = R(I)
      ZIN(1,1,I) = PP(I)
      ZIN(1,2,I) = PP1(I)
      ZIN(1,3,I) = PP2(I)
   10 CONTINUE
      LAST = 0
      IF ( KNT .EQ. 3 )   LAST = 1
      CALL XYZPLT
      RETURN
      END
```

Figure B-4 (Cont'd). Listing of Shock Propagation Code.

REFERENCES

1. Fry, P. F., A Review of the Analyses of Hydrodynamic Ram, AFFDL-TR-75-102, Wright-Patterson Air Force Base, Ohio, Air Force Flight Dynamics Labs., In Print.

2. Stepka, F. S., C. R. Morse, and R. P. Dengler, Investigations of Characteristics of Pressure Waves Generated in Water-Filled Tanks Impacted by High-Velocity Projectiles, NASA TN D3143, NASA, Wash. D.C., Dec. 1965.

3. Fuhs, A. E., R. E. Ball, and H. L. Power, FY73 Hydraulic Ram Studies, Naval P.S., Monterey, California, Feb. 1974.

4. Lundstrom, E. A. and E. W. Stule, Fluid Dynamic Analysis of Hydraulic Ram II (Results of Experiments), Naval Weapons Center, Chine Lake, California, 1973.

5. Rosenblatt, M., G. E., Eggum, and L. A. DeAngelo, Numerical Analyses of Fuel Tank Penetration Dynamics, AFFDL-TR-76-31 (CRT-300-1, review draft), California Research and Technology, Woodland Hills, California, Nov. 1975.

6. Williams, R. F., Shock Effects in Fuel Cells, SR 1 Report Accession No. L-23995, Stan. Res. Inst., Menlo Park, California, Oct. 1969.

7. Yurkovitch, R., Hydraulic Ram: A Fuel Tank Vulnerability Study, MDC G 964, McDonnell Aircraft Corp., St. Louis, MO, Sept. 1969.

8. Zabel, P. Tests of Hydraulic Ram Buffering Materials, D.S. Rept. 1560-74-43, Ultrasystems Inc., Dynamic Science Div., Phoenix, Arizona, May 1974.

9. Ball, R. E., Structural Response of Fluid Containing Tanks to Penetrating Projectiles (Hydraulic Ram) - A Comparison of Experimental and Analytical Results. NPA-75B p76051, Naval Post Graduate School, Monterrey, California, May 1976.

10. McQueen, R. G., S. P. Marsh, J. W. Taylor, J. N. Fritz, and W. J. Carter, "The Equation of State of Solids from Shock Wave Studies" in High-Velocity Impact Phenomena, R. Kinslow, Academic Press, New York, 1970.

11. Barker, L. M., R. E. Hollenback, "Shock-Wave Study of the $\alpha \rightarrow \epsilon$ Phase Transition in Iron," Appl. Phys. 45, 4872-4887, 1974.

12. Thiel, M. (ed.), Compendium of Shock Wave Data, UCRL-50108 (Vol.1) Lawrence Rad. Lab., Livermore, California, June 1966.

13. Power, H. L., FY74 Experimental Hydraulic Ram Studies, NPS-57Ph 74081, Naval P. G. S., Monterey, California, August 1974.

14. Lundstrom, E.A., and W.K. Fung, Fluid Dynamic Analysis of Hydraulic Ram IV (User's Manual for Pressure Wave Generation Mode), JTCG/AS-74-T-018.

15. M.J. Jacobson and J.R. Yamane, Effects of Internal Blast on Combat Aircraft Structures (Vol. 1), The BR-1A Computer Code for Transcent Structure Response to Blast Loading of Aircraft Compartments, AFFDL-TR-75-73, (Vol. 1), Northrop Corp., Hawthorne, California, July 1975.

16. Bach, G.C. and J.H. Lee, "Shock Propogation in Solid Media," Presented at the 5th Aerospace Sciences Meeting of the AIAA, Paper No. 67-141, January 2326 1967, New York, N.Y.: AIAA, January 1967, A6718290.

17. Stepka, F.S. and C.R. Morse, Methods for Reduction of Fracture Damage of Projectile-Impacted Liquid-Filled Tanks, NASA TM-X-1224, Washington: National Aeronautics and Space Administration, March 1966.

18. Dewitt, Richard J. and Patrick H. Zabel, Tests of Hydraulic Ram Buffering Materials I, Dynamic Science Report 1560-74-43- , Phoenix, Arizona: Dynamic Science Division, Ultrasystems, Incorporated, 30 May 1974.

19. Bristow, R.J. "Design of Hydraulic Ram Resistant Structure," in Proceedings of the Army Symposium on Solid Mechanics, 1972, Watertown, Mass.: AMMRC, September 1973, AMMRC MS 73-2, AD 423063.

20. Lundstrom, E.A., Private Communication, 1976.

21. Brass, J. J.R. Yamane, and M.J. Jacobson, Effects of Internal Blast on Combat Aircraft Structures, (Vol. II), User's and Programmer's Manual, AFFDL-TR-73-136, (Vol. II, Northrop Corp, Hawthorne, January 1974.

22. Lundstrom, E.A., "Fluid/Structure Interaction in Hydraulic Ram" (draft), paper presented to Hydrodynamic Ram Seminar, Sponsored by JTCG/AS-AFFDL, Dayton, Ohio Oct. 20-22, 1976.

23. Prandtl, L., "Essentials of Fluid Dynamics," Hofner, New York, 1952.

24. Shapiro, A.H., "The Dynamics and Thermodynamics of Compressible Fluid Flow," Volume 1, Ronald Press Co., New York, 1953.

25. Ankeney, P., private communication, 1976.

*U.S.Government Printing Office: 1978 — 757-080/495